INFORMATION TO USERS

This manuscript has been reproduced from the microfilm master. UMI films the text directly from the original or copy submitted. Thus, some thesis and dissertation copies are in typewriter face, while others may be from any type of computer printer.

The quality of this reproduction is dependent upon the quality of the copy submitted. Broken or indistinct print, colored or poor quality illustrations and photographs, print bleedthrough, substandard margins, and improper alignment can adversely affect reproduction.

In the unlikely event that the author did not send UMI a complete manuscript and there are missing pages, these will be noted. Also, if unauthorized copyright material had to be removed, a note will indicate the deletion.

Oversize materials (e.g., maps, drawings, charts) are reproduced by sectioning the original, beginning at the upper left-hand corner and continuing from left to right in equal sections with small overlaps.

ProQuest Information and Learning
300 North Zeeb Road, Ann Arbor, MI 48106-1346 USA
800-521-0600

A Realistic Simulation System for Quantitative Functional Imaging with Positron Emission Tomography

Yilong MA

Department of Biomedical Engineering
McGill University, Montreal, Quebec, CANADA

September 1999

A thesis submitted to the Faculty of Graduate Studies and Research in partial fulfillment of the requirements of the degree of Doctor of Philosophy

Abstract

We have developed and implemented an analytic simulation system to evaluate and correct quantitative imaging distortions in positron emission tomography (PET) scans. It is based on measured tomograph characteristics and realistic 3-D brain models generated from regionally segmented brain image data. Each structure is assigned with a regional radiotracer concentration and attenuation coefficient to create 3-D dynamic brain models and tissue attenuation maps. Projection data are then generated by incorporating key physical factors of detector geometry and resolution, attenuation, scatter, randoms, efficiency, deadtime and counting statistics. This has been done for a multi-slice PET scanner and includes temporal sampling and radiotracer decay. Simulated emission and transmission data are reconstructed by a filtered-backprojection algorithm.

The simulation methods are validated by scan data from both geometrical and anatomically realistic brain phantoms. Simulated projection components of a uniform phantom and a 3-D Hoffman brain phantom agree accurately with the measured data from our PET scanner. We then summarize current applications of this simulation tool to improve regional radioactivity quantification and optimize imaging protocols. In particular we have implemented a novel methodology to estimate and correct 3-D partial volume effects in dynamic PET studies using correlated magnetic resonance images. Simulations and phantom data in both single and double isotope experiments reveal substantial errors in striatal and cortical structures. Both show spatially variant and nonlinear distortions in time-activity curves which become more significant with degrading image resolution. These errors are removed completely by the partial volume correction algorithm with a reasonable increase in variance.

This software package is flexible and extensible. We have added many automatic steps to increase computational efficiency and simplify its usage in a clinical environment. This simulation tool offers a unified framework to evaluate and optimize PET imaging methodology from data acquisition, processing, and reconstruction to image analysis and physiological parameter estimation.

Résumé

Nous avons développé et implémenté un simulateur analytique destiné à évaluer et à corriger les distorsions quantitatives présentes dans les images obtenues en tomographie d'émission de positons (TEP). Cette méthode est basée sur les caractéristiques physiques mesurées du tomographe et sur des modèles cérébraux réalistes générés à partir d'images cérébrales segmentées. Chaque structure cérébrale identifiée se voit assignée une concentration en traceur radioactif et un coefficient d'atténuation afin de créer des modèles cérébraux 3-D dynamiques ainsi que des cartes d'atténuation. Des projections sont ensuite générées après incorporation des facteurs physiques fondamentaux relatifs à la géométrie de détection et à la résolution, à l'atténuation, aux rayonnements diffusés et fortuits, à l'efficacité de détection, et à la statistique de comptage. Cela a été implémenté pour un tomographe multi-coupes et incorpore l'échantillonnage temporel et la décroissance radioactive du traceur. Les projections simulées des données d'émission et de transmission sont ensuite reconstruites à l'aide d'un algorithme de rétroprojection filtrée. Les méthodes de simulation sont validées par des données tomographiques provenant de fantômes géométriques ainsi que de fantômes anatomiques réalistes. Les composantes des projections simulées d'un fantôme uniforme ainsi que d'un fantôme de cerveau 3-D (Hoffman) sont en accord avec les données mesurées à l'aide de notre tomographe TEP. Nous résumons ensuite les applications actuelles de cet outil de simulation dans le cadre de l'amélioration de la quantification des mesures régionales de radioactivité et l'optimisation des protocoles d'imagerie. Nous avons implémenté en particulier une nouvelle méthodologie pour estimer et corriger les données TEP dynamiques des effets de volume partiel en 3-D basée sur l'emploi d'images par résonnance magnétiques corrélées. Les données obtenues par simulation et à l'aide d'un fantôme anatomique pour des expérimentations utilisant soit un seul, soit 2 isotopes, révellent des erreurs substantielles au niveau des noyaux striés et du cortex cérébral. Ces deux études mettent en évidence des distorsions variant spatialement et non linéaires au niveau des courbes d'activité temporelles qui deviennent d'autant plus significatives avec la dégradation de la résolution image. Ces erreurs sont totalement éliminées par l'algorithme de correction des effets de volume partiel au prix d'une augmentation modérée de la variance. Cet ensemble algorithmique est flexible et extensible. Nous avons implémenté de nombreuses fonctions automatiques afin d'optimiser l'efficacité de calcul et de simplifier son utilisation en environement clinique. Cet outil de simulation offre un cadre de travail unifié pour évaluer et optimiser la méthodologie TEP depuis l'acquisition, le traitement, et la reconstruction des images, jusqu'à leur analyse et à l'estimation des paramètres physiologiques.

Dedication

To my parents who devoted everything to their children and taught them diligence and persistence from the beginning...

Acknowledgment

This project has been completed at the McConnell Brain Imaging Centre of the Montreal Neurological Institute. First of all I wish to thank my advisor Dr. Alan Evans for his confidence and support over the course of this study. I am also indebted to Dr. Chris Thompson for many insightful discussions on PET instrumentation and Dr. Terry Peters for teaching fundamental principles of medical imaging. Their emphasis on the value of basic science in clinical practice makes this work all worthwhile.

It is a great privilege to work and learn in this cooperative environment. Many technical staff and fellow students offered their expertise on multimodal imaging methodology and biomedical computing. I am especially thankful to the programming assistance from Peter Neelin, Micheline Kamber, Louis Collins and Greg Ward on several occasions. I also appreciate our cyclotron unit for preparing radioactive solution in PET studies and Atsushi Takahashi for performing MR scans of the brain phantom. Special thanks go to Vasco Kollokian for providing emergency disk space, and Kate Hanratty and Kerry Jones for administrative assistance.

I want to express my gratitude to a number of colleagues for a fruitful collaboration. Particularly Olivier Rousset for creativity and inspiration; Youpu Zhang for sharing some programs; Kenya Murase, Wei Gu, David Reutens and Alain Dagher for stimulation. Their effort and insight have expanded new horizons of this project. I would also like to mention the helpful input from Dr. David Hawkes at the Guy's Hospital London and Dr. Dean Wong at the Johns Hopkins Hospital.

This thesis would not have been completed without invaluable help from Dr. Alan Evans and Peter Neelin. I am extremely thankful to their efforts in improving and proofreading the manuscript. I will remember all my coworkers at 527 Pine Ave West

for their kindness, assistance and cheerful encouragement during the last leg of this journey.

My scientific pursuit would not be possible without the unfailing support and encouragement from my family and relatives over many years. I take this occasion to forward my hearty appreciation to each and everyone of them on the other side of the globe. I also acknowledge the friendship and generosity from Wenxin Ruan, Ariel Edery and Michaela Gutmann. I have enjoyed many memorable times with their family in Montreal. Finally I am grateful to the financial assistance from the Medical Research Council of Canada and the McConnell-Pew Program in Cognitive Neuroscience.

Original Scholarship

The bulk of this work has originated from independent investigations of the author. Its completion depends partially on the rich programming and computational resources at the Montreal Neurological Institute. The principal contributions of this thesis are summarized below.

1. Design and implementation of a fast simulation tool (*PETSIM*) to model data acquisition and image reconstruction of a PET system. It can perform dynamic emission/transmission simulation and analysis automatically on a single platform. It has been implemented for general application in both brain and body imaging studies.

2. Systematic validation of simulation methodology with many different phantom scans. Simulated data and images are in good agreement with the experimental measurement. In effect this establishes a realistic physical model of data collection for statistical image reconstruction algorithms. Numerical analyses reveal some errors in the scatter and attenuation correction methods of the scanner.

3. Applications in the development and validation of a number of other projects to assist in the design of optimal data analysis strategy in clinical PET study protocols.

This work reveals nonlinear distortions in regional activity values under static and dynamic imaging conditions. It offers an objective basis to compare MR-PET image registration methods using both emission and transmission scans. Besides its instrumental use in one MSc and one PhD theses at McGill, *PETSIM* has also played a key role in another doctoral dissertation in France. We have implemented an elegant algorithm to remove 3-D partial volume distortions using correlated structural images. It works by imaging each structure separately in order to estimate structure-specific recovery coefficients and activity spillover contributions. This method has

been validated by simulated dynamic scans and real phantom studies. *PETSIM* and the partial volume correction method have also been installed at the Johns Hopkins University for clinical neuroreceptor imaging.

With 22 abstract presentations this work has led to the following publications:

1. Y. Ma, M. Kamber, and A.C. Evans. 3-D simulation of PET brain images using segmented MRI data and positron tomograph characteristics. *Comput Med Imag Graph* 17: 365-371, 1993.

2. O. Rousset, Y. Ma, M. Kamber, and A.C. Evans. 3-D simulations of radiotracer uptake in deep gray matter structures of human brain. *Comput Med Imag Graph* 17: 373-379, 1993.

3. P. Neelin, J. Crossman, D.J. Hawkes, Y. Ma, and A.C. Evans. Validation of an MRI/PET landmark registration method using 3-D simulated PET images and point simulations. *Comput Med Imag Graph* 17: 351-356, 1993.

4. O. Rousset, Y. Ma, G. Leger, A.H. Gjedde, and A.C. Evans. Correction for partial volume effects in PET using MRI-based 3-D simulations of human brain metabolism. In: *Quantification of brain function using PET*. K. Uemura, N.A. Lassen, T. Jones and I. Kanno, editors. Amsterdam: Elsevier; 1993: 113-123.

5. O. Rousset, Y. Ma, S. Marenco, D.F. Wong, and A.C. Evans. In vivo correction for partial volume effects in PET: accuracy and precision. In: *Quantification of brain function using PET*. R. Myers, V. Cunningham, D. Bailey and T. Jones, editors. San Diego: Academic Press; 1996: 158-165.

6. Y. Ma, and A.C. Evans. Analytical modeling of PET imaging with correlated functional and structural images. *IEEE Trans Nucl Sci* 44: 2439-2444, 1997.

7. O. Rousset, Y. Ma, and A.C. Evans. Correction for partial volume effects in PET: principle and validation. *J Nucl Med* 39: 904-911, 1998.

8. O. Rousset, Y. Ma, D.F. Wong, and A.C. Evans. Pixel verses ROI based partial volume correction in PET. In: *Quantification of brain function using PET*. R.E. Carson, M.E. Daube-Witherspoon and P. Herscovitch, editors. San Diego: Academic Press; 1998: 67-75.

Contents

List of Tables

List of Figures

Chapter 1

Introduction

Positron Emission Tomography (PET) is a powerful imaging system to measure the spatial distribution of a large number of radiopharmaceuticals in the living human body. Biologically active compounds are labeled with several short-lived radionuclides and administered into the bloodstream to probe a series of rapid biochemical processes in the organ of interest. By estimating their concentrations in tissue and blood at different times PET allows the formulation of compartmental models to generate many important physiological parameters. The most common variables include blood flow, blood volume, oxygen consumption, glucose metabolism and neuroreceptor distribution.

Because of the sensitivity of PET it is possible to detect very small amounts of radioactive molecules in the body without disturbing their normal activity. This offers a unique opportunity to perform quantitative investigation of many biological functions *in vivo*. Biochemical change can be localized and measured in any part of the brain. This allows us to ask very specific questions about the behavior of both normal and abnormal brains. While the majority of clinical studies are in humans PET has also been increasingly used in experimental animals.

PET has been widely used to provide three-dimensional (3-D) analysis of cerebral physiology and biochemistry. However it is an expensive device and there are still some technical problems which limit its quantitative imaging capability. In practice a general computational tool is needed to model these problems and predict the behavior. This thesis describes the design and implementation of a 3-D computer simulation system to incorporate realistic organ and tomograph properties. It has a number of useful features to evaluate and optimize many aspects of PET imaging protocols in clinical applications.

1.1 History Overview

The discovery of X-ray and radioactivity about 100 years ago has opened a tremendous window to explore the interior of the human body [Webb, 1995]. Most early work used radiographic means to record x-rays passing through the organ or gamma-rays emitted by radioactive substances injected into the organ. These types of examinations were called transmission and emission imaging respectively. However both provided only two-dimensional (2-D) projection images of the internal structures without giving much depth information. Tomographic systems were then made to visualize specific areas by using ingenious mechanical motions between the radiation sources and radiographic films. This innovation formed the basis of body section imaging to view not only tissue composition and blood vessels but also the distribution of certain radioactive compounds.

With the onset of the computer age in the 1950s, electronic detectors were used to record high energy radiation. They gave the ability to process data digitally rather than analogically. This moved body section imaging from qualitative inspection to quantitative evaluation. Great progress was made in the emission imaging modality

with the invention of scintillator cameras in the 1960s. This scanning device employed Anger logic to determine position by use of a network of resistors and permitted dynamic processes to be monitored rapidly. Thereafter mathematical algorithms based on algebra solutions and filtered backprojection (FBP) were successfully implemented to reconstruct images from projection data collected at a large number of linear and angular positions. These advances led to the design of X-ray computerized tomography (CT) in 1973 and single photon emission computed tomography (SPECT) in 1976.

The potential of positron emitters for biological imaging was recognized in the early 1950s from advances in radiochemistry. However the development of modern PET scanners began only after many years of work in single photon imaging. The circumstances that fostered its rapid growth have been reviewed by one of the early pioneers [Ter-Pogossian, 1985]. Fundamental to the success of PET are the use of biochemical compounds which produce paired gamma-rays 180° apart and the use of coincidence detection to reconstruct 3-D radioactivity distributions. Counts are collected by recording the response of scintillators along many thousands of projection lines around the body. PET design has evolved from single-slice to multi-ring systems that measure tissue activity concentration simultaneously in a larger image volume. The continued improvements over the last two decades have increased the resolution and sensitivity by an order of magnitude [Cherry and Phelps, 1996]. This allows both 2-D and 3-D imaging of increasingly smaller structures in most major organs of the body.

Parallel to innovations in instrumentation, many computational solutions have also been developed to improve the quantitative accuracy and precision of activity estimates. This is necessary to remove physical distortions inherent in tomographic

data acquisition and image reconstruction. Iterative image reconstruction algorithms based on maximum likelihood and Bayesian modeling are implemented in a number of medical imaging laboratories. They generally provide more accurate images than the FBP methods. However their success depends very much upon *a priori* knowledge about PET data collection.

Magnetic resonance imaging (MRI) came into existence in the early 1980s. It yields excellent images of body structures by detecting signals emitted after the body is illuminated by electromagnetic radiation. CT gives much the same information with the highest contrast between soft tissue and bone whereas MRI provides larger soft tissue contrast and reveals high resolution details of brain structures. Both are standard imaging equipment in diagnostic radiology. While CT and MRI are best in visualization of body anatomy they can also see vascular structures with or without injecting contrast agents. PET and SPECT are most suitable to quantify dynamic radiotracer uptake and are used mainly in nuclear medicine. SPECT gives relatively poor images mainly because it detects only single gamma-rays. PET provides much better images by detecting coincident gamma-rays from a large number of biochemicals directly involved in organ function.

PET and MRI represent the most advanced imaging tools for measuring functional and structural changes in the human brain. Although functional changes often precede detectable anatomical abnormalities both are currently being used to study epilepsy. stroke. brain tumors. Alzheimer's disease. movement disorders and neuropsychiatric illness. PET and functional MRI have also been used to map neuronal activation in the human brain under a wide variety of physiological stimuli. Despite their differences both provide complementary information. It is a common practice to employ MRI data to improve PET image analysis. Great advances have been made

by combining multimodal image data for functional and anatomical correlation.

1.2 Rationale and Objectives

PET images are typically collected in a dynamic mode to determine regional tissue time-activity curves (TAC). These data are then analyzed to estimate kinetic model parameters. Accurate measurement of the local concentration with PET depends on both the uptake properties of radiotracers in each structure and the technical characteristics of tomography design. In most imaging studies the tracers of physiological significance are distributed in 3-D anatomical structures of irregular shapes and finite sizes, which are often small and differ little in their uptake values. The primary limitations of PET include poor spatial resolution (e.g. 1 mm for MRI; 5-6 mm for PET; 10-15 mm for SPECT) and low counting statistics. Poor resolution leads to gross errors in apparent tracer distribution called partial volume effects (PVE). Consequently the accuracy and precision of the measured activity concentration depend on imaging conditions.

Regional distortions from the PVE are spatially and temporally variant due to the dynamic nature of radiotracer uptake. This is a big problem in itself producing non-stationary bias and variance on each TAC. The errors in the observed data propagate directly into estimated functional parameters. It also poses problems due to inadequate temporal sampling and unknown noise characteristics. Low signal/noise ratios are reduced further by noise amplification in data processing and reconstruction algorithms. Both degrade a scanner's contrast sensitivity to detect small specific biochemical change in the brain. This may introduce some morphometric distortions in physiological activation studies.

The effects of tomograph design on quantitative image quality are usually eval-

uated by scanning physical phantoms on each tomograph. Most phantoms rely on regular-shaped objects to represent tracer distributions in the human brain. Although providing valuable information these methods are often insufficient owing to the interaction between individual physical factors and the complex tracer uptake in brain structures. It is important to note that PET measurement is specific to the organ characteristics under investigation.

The problems have also been addressed using computer simulations. Conventionally this is done by Monte Carlo simulations which trace photon interaction in the object and the detection system. Because of the extremely heavy computational load this method is generally limited to the use of regular geometrical shapes to model radiotracer distribution and tissue attenuation. This tool is not suitable for revealing distortions in image reconstruction because of the limited number of counted events and hence excessive noise in simulated data. Despite the great improvement in computing power the limitation in speed is still one primary drawback for clinical use.

In recent years, analytical simulations based on simple mathematical modeling have become increasingly valuable because they can provide much faster and flexible solutions to evaluate a number of problems in PET imaging. Modeling tools with different degrees of sophistication have been used by researchers with diverse objectives. The most common methods perform simplistic simulations on TACs directly in image space [Blomqvist et al., 1995]. It ignores any errors coming from object and camera dependent factors. This type of work does not recognize image bias and variance introduced by the projection-backprojection process. More elaborate methods simulate physical components at the projection level followed by image reconstruction [Mahoney et al., 1987]. By modeling image acquisition from raw data this approach

allows correct simulation of the magnitude and distribution of noise. However they all have some limitations because of inadequate or incomplete object creation and data generation models. Such restrictions make these tools less useful for general dynamic studies. It should be noted that none of the previous methods have been experimentally validated despite their widespread usage.

In this dissertation we present a general analytical simulation approach to study quantification problems in PET imaging methodology. There are two motivations underlying this approach: 1) the evaluation and restoration of imaging distortions in emission and transmission scans, and 2) the improvement and optimization of PET imaging protocols. The method reported here differs from others in two ways. First, it is based on the use of realistic 3-D objects created jointly from the segmented MRI/PET images and radiopharmaceutical biodistribution data. Second, it models the data acquisition of a PET system in the projection space according to its physical characteristics.

The primary goal of this project is to develop and implement an automated software system so that one can simulate both static and dynamic PET imaging studies very rapidly. The work centers on the quantification issues in PET brain imaging and the methodology consists of four parts:

a) A computerized 3-D brain phantom is constructed by segmenting a set of MR images of the human brain into distinct tissue and anatomical maps. Fine anatomical structures are incorporated according to a standardized neuroanatomical atlas.

b) 3-D activity distribution and tissue attenuation coefficients are assigned to the segmented brain image data. This allows the creation of functionally and anatomically realistic brain models.

c) Projection data of the brain model are generated at many angles using the

sampling geometry and axial/transverse detector response functions of a specific tomographic scanner configuration. Both emission and transmission scans are simulated with major physical and statistical effects in PET data acquisition.

d) The set of projection data are then reconstructed with different reconstruction algorithms and parameters. Images are obtained and analyzed in the same way as in clinical PET scans.

The simulation algorithms developed here have been validated with the experimental data acquired from simple phantoms and 3-D brain phantoms. This has been done on a brain tomograph at the Montreal Neurological Institute and a body scanner at the Johns Hopkins University Hospital.

The PET simulator provides a useful tool to predict image bias and variance in typical clinical studies. It allows for the correction of the PVE based on anatomical information from co-registered MRI data. In this work we demonstrate a novel PVE correction method and evaluate its accuracy with a 3-D brain phantom in both static and dynamic imaging conditions. We also show its application for evaluating image registration errors between MRI and PET images. In addition we describe briefly its usefulness in estimating the signal/noise ratios in brain activation scans and investigating iterative image reconstruction algorithms with anatomical constraints.

This thesis is organized as follows. Chapter 2 reviews the physical principles of PET imaging and its major application areas. In Chapter 3 we discuss current problems related to image quantification and examine the signal/noise characteristics associated with the entire data correction and image reconstruction process. Chapter 4 surveys common experimental methods for characterizing the system performance of a PET scanner and compares simulation approaches used by others in the field. In Chapter 5 we describe the simulation algorithms and their implementation in

our environment. This is followed by model validation in Chapter 6 using both simulated and measured data from phantom studies. We then summarize several clinical applications of this simulation tool in Chapter 7. Finally Chapter 8 presents a general conclusion along with a brief discussion on the future direction of this research program.

Chapter 2

Operating Principles of PET Imaging

Positron emission tomograph (PET) is a noninvasive imaging tool to quantify 3-D distribution of many biological compounds in the body. Being radioactively labeled with positron-emitting isotopes these compounds are actively involved in the functional processes of a large number of organs. A positron and an electron undergo an annihilation reaction in tissue with the production of two 511 keV photons travelling in opposite directions as seen in Fig. 2.1. Both photons can be recorded simultaneously by external radiation detectors to determine the area of space within which the annihilation has taken place. A PET scanner contains thousands of highly sensitive detectors mounted on multiple rings. It measures the total number of annihilation events between each pair of detectors. By combining data from many different angles tomographic images can be reconstructed to represent the density of positron-labeled molecules in the tissue.

PET images are acquired at one or more times to provide a series of static or dynamic frames. It is a common procedure to convert dynamic data into regional biochemical variables by the use of appropriate mathematical models of tracer kinetics.

With proper tracers PET offers great opportunities to study local hemodynamics, metabolism and pharmacokinetics *in vivo* [Diksic and Reba, 1991]. A typical PET study protocol consists of the following steps: a) Intravenous injection of radiotracers and blood sampling from an artery: b) Acquisition of PET projection data at different time intervals: c) Data processing and image reconstruction from measured projection data: d) Generation of time-activity curves (TACs) in different organ structures with a set of regions of interest. e) Estimation of physiological parameters from tissue and blood TACs using tracer kinetic models.

The construction and operation of a PET imaging system result from a collaborative effort between several scientific and medical disciplines. These range from radiochemistry, engineering, physics, computer science to physiology and medicine. In this chapter we describe the basic principles of PET technology and summarize its major applications in quantitative functional imaging.

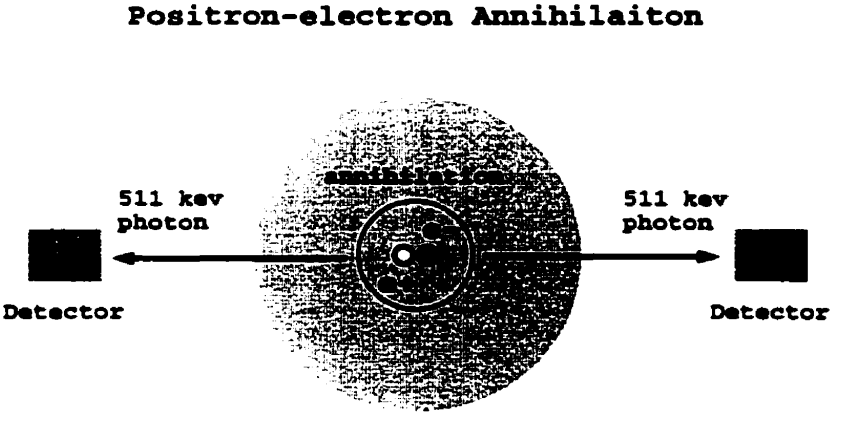

Figure 2.1: Back-to-back emission of 511 keV γ-rays by positron and electron annihilation. Both photons help locate the positron source along a line between the two detectors.

2.1 Positron Emission and Detection

2.1.1 Synthesis of positron emitters

One of the key features of PET imaging is the use of biologically relevant compounds such as sugar and water. These can be combined with radioisotopes such as carbon (C-11), oxygen (O-15), nitrogen (N-13) and fluorine (F-18) which reach stability by the ejection of a positron. Importantly most compounds employed are native substances or their analogs produced and consumed by body cells. The fundamental principle of radiotracer design is labeling molecules with the smallest modification (e.g. C-11/F-18) so that they will be chemically indistinguishable from their natural counterparts. This is important so that the tracer will have a known and predictable pharmacological behavior along the chosen biochemical pathway.

Positron-emitting radioisotopes for PET studies have short half-lives ranging from 2 minutes to 2 hours (Table 2.1). Thus they are usually produced on site in a medical cyclotron by bombardment of stable elements with protons. Both positive and negative ion systems are in use where protons are accelerated to sufficient energy prior to striking a target. Target materials are then extracted and incorporated into compounds using special radiochemical reactions. The radiochemical yield is usually the combination of two competing processes, namely increasing chemical yield and radioactive decay. It reaches a peak between 10 and 60 minutes depending on the half-life of radioisotope and the method of tracer production.

There are several challenges and requirements associated with radiotracer development (a) rapid synthesis of compounds in its purest chemical form; (b) high specific activity (i.e. radioactivity to mass ratio) of the labeled products with minimal dilution from unlabeled compounds; (c) accurate dose calculation to give reliable specific

activity estimates and (d) rigorous quality control methods to ensure safety to the subjects and timely delivery of the tracer in clinical use. Currently most cyclotrons provide automated radiopharmaceutical synthesis modules to achieve these goals and simplify the process.

In a PET imaging study, a very small amount of radioactive material is introduced into the body to probe organ physiology and biochemistry. It can be injected into the veins or inhaled in a gas form prior to a PET scan. This tracer will participate in many biochemical reactions in both tissue and vascular space. It is known that quantitative studies of tracer kinetics in the tissue require the knowledge of the tracer concentration in the circulation system as a function of time. In most cases this information is extracted by taking blood samples from radial artery following tracer administration. Automatic tracer injectors and blood samplers are installed in some PET establishments [Graham and Lewellen, 1993] to increase the scan throughput and decrease radiation exposure to technicians.

2.1.2 Positron and electron annihilation

Radionuclides used in PET imaging decay by positron emission: $p => n + e^{+} + \nu$, where p refers to the proton, n the neutron, ν the neutrino and e^{+} the positron with additional kinetic energy. After losing most of its energy in tissue one positron will annihilate with a nearby electron (Fig. 2.1), emitting a pair of 511 keV gamma rays towards opposite directions according to the law of energy and momentum conservation. These gamma-rays have sufficient energy to escape the body and can be detected using coincidence detection techniques described in the next section.

The spatial accuracy for localizing positron sources is limited by two physical phenomena (Fig. 2.2). Firstly, before annihilation positrons travel a short distance

from the emitting tracer molecule. This process is shown to follow a bi-exponential distribution with a maximum displacement of $\leq$10 mm for typical positron-emitting radioisotopes [Palmer and Brownell, 1992]. Consequently the site of annihilation is not exactly the location of the radiotracer. This corresponds to a finite range depending on the maximum positron energy of a given isotope decay. Table 2.1 shows that the mean range in water is smaller than 2-3 mm for most common radionuclides used in clinical PET imaging.

Secondly, the positron and electron are not stationary before collision because of thermal agitation. As a result the two γ-rays are not strictly in the opposite directions and may deviate from the ideal line of emission. This is equivalent to an angular distribution with a finite width of roughly 0.3°, about a mean angle 180° between the two annihilation photons. Its contribution to the spatial uncertainty is proportional to the detector separation. Both effects put a 3-4 mm lower limit on the resolution of the human PET scanners. In other words there is a residual uncertainty in locating the site of positron emission even with perfect 'point' detectors.

Table 2.1: Physical characteristics of positron-emitting radionuclides

Radionuclides	Half life	Maximum energy	Maximum range	Mean range
	(min)	(MeV)	(mm)	(mm)
Oxygen-15	2.07	1.72	8.0	2.5
Nitrogen-13	9.96	1.20	5.1	1.5
Carbon-11	20.3	0.96	3.9	1.1
Fluorine-18	109.8	0.64	2.4	0.6
Gallium-68	68.3	1.90	8.9	2.9

The positron range values are quoted for water from the literature [Phelps et al., 1975].

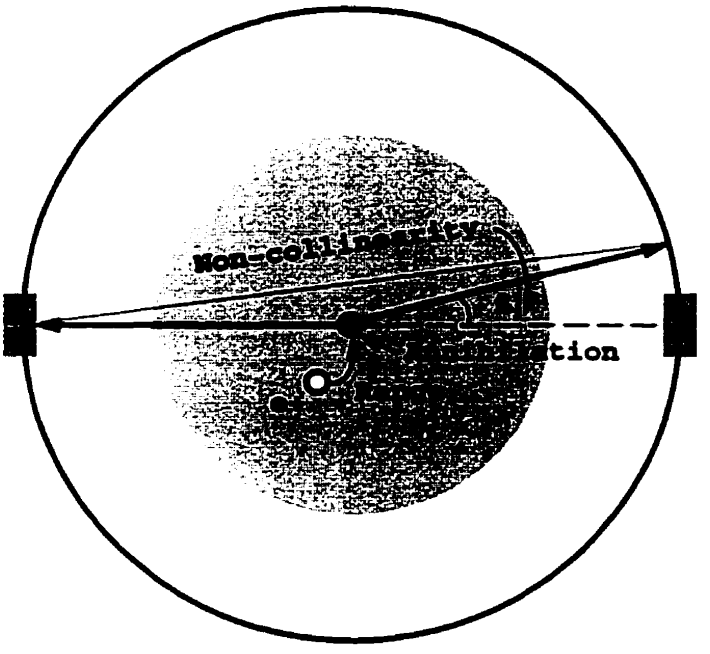

Figure 2.2: Illustration of positron range and photon non-collinearity effects. Both cause a spatial uncertainty in source localization and hence worsen image resolution.

2.1.3 Photon interaction with matter

γ-rays with moderately high energy interact with matter mainly by two mechanisms. The first one is Compton scatter where a photon loses part of its energy and changes direction after colliding with a free or loosely bound electron. The scattered photon has a reduced energy

$$E_s = \frac{E}{1 + \alpha(1 - cos\theta)} \tag{2.1}$$

where $\alpha = E/E_o$ is the incident photon energy E normalized to the static electron energy $E_o = 511$ keV, and θ is the scatter angle. $E_s \approx E$ when θ is small. At $E = E_o$, E_s ranges from $\frac{1}{2}E$ to $\frac{1}{3}E$ for scatter angles between 90° and 180°. The majority of photons undergo multiple interactions and subsequently lose all of their energy.

This is the phenomenon primarily responsible for photon attenuation (at 511 keV) in body tissue. The second one is the photoelectric effect in which a photon ejects one electron from the outer orbit of an atom. A very small portion of the photon energy is used to overcome the binding energy of the electron with the reminder imparted as kinetic energy to the ejected photoelectron. As a result the incident photon loses its energy at once and becomes totally absorbed. This is the chief mechanism of radiation detection using scintillators.

In general both interactions occur with certain probability and there are always some photons that escape from the object without undertaking any interaction. Let I_i and I_o denote the number of photons before and after passage of a uniform medium. we then have

$$I_o = I_i e^{-\mu L} \tag{2.2}$$

where L is the thickness of the medium and μ its linear attenuation coefficient in cm^{-1}. This defines the attenuation factor $e^{-\mu L}$ and the absorption probability 1-$e^{-\mu L}$. The total attenuation value at a given photon energy is calculated by (c.f. [Johns and Cunningham. 1969]).

$$\mu = \mu_{cs} + \mu_{pe} \tag{2.3}$$

with the Compton part given by

$$\mu_{cs} = \rho_e 2\pi r_\circ^2 \{\frac{1+\alpha}{\alpha^2}(\frac{2(1+\alpha)}{(1+2\alpha)} - \frac{ln(1+2\alpha)}{\alpha}) + \frac{ln(1+2\alpha)}{2\alpha} - \frac{1+3\alpha}{(1+2\alpha)^2}\} \tag{2.4}$$

where ρ_e is the electron density of the material (cm^{-3}) and $r_\circ$ is the effective electron radius (2.817938 x 10^{-13} cm). and the photoelectric part described by

$$\mu_{pe} = A\rho_m Z^4 E^{-B} \tag{2.5}$$

in material of mass density ρ_m and effective atomic number Z. A and B are fitting parameters with different values below and above the highest K-shell absorption energy. B has a nominal value of 3 in most materials.

Table 2.2: Theoretical linear attenuation coefficients at 511 keV

Tissue	Density	μ (cm^{-1})	Material	Density	μ (cm^{-1})
Blood	3.51	0.1007	Aluminum	7.84	0.2250
Bone	5.27	0.1509	BaF_2	12.4	0.4366
Brain	3.44	0.0985	BGO	18.1	0.8983
Brain Stem	3.50	0.1003	CsF	10.4	0.3712
CSF	3.42	0.0980	Germanium	14.2	0.4236
Fat	3.06	0.0877	GSO	17.4	0.6650
Hair	4.20	0.1204	Lead	27.0	1.6282
Heart	3.42	0.0979	Lucite	3.83	0.1098
Lung	0.86	0.0247	Polystyrene	3.38	0.0969
Muscle	3.45	0.0987	Sodium Iodide	9.43	0.3254
Skin	3.64	0.1043	Tin	18.5	0.6359
Water	3.34	0.0958	Tungsten	46.9	2.3901

This table gives the electron density ($10^{23}/cm^3$) and the total attenuation coefficient (μ) of each material.

Both terms decrease as a function of photon energy with μ_{pe} dropping much more rapidly. In order to provide a theoretical reference we have calculated the total attenuation coefficients to 511 keV radiation using recently published parameters [Picard et al., 1992]. Table 2.2 lists the values for typical biological tissues and solid materials. We need these data to estimate photon attenuation in the body and also to compare the stopping power of different detectors. A large attenuation value would increase the absorption probability and hence the stopping power.

2.2 Data Collection and Processing

The most important mechanism in a PET imaging system is the coincidence instrumentation used to detect annihilation radiation emitting from the activity distribution. This requires dense and fast scintillation crystals optically coupled to photomultiplier tubes (PMT). Atoms in the crystal are excited to a higher energy state by impinging photons and then emit visible light as they decays back to the ground state. The light intensity is proportional to the amount of energy deposited in the crystal by the photon. Thus each incoming γ-ray (511 keV) produces many low energy photons which are collected in the PMT and converted into electrical signals. The output signal of each detector contains information on the energy received by the crystal and the time of interaction. Some discriminatory processing is needed in order to register the total number of annihilation photons. In the following sections we describe the process of coincidence detection with one pair of detectors and discuss some system design features.

2.2.1 Basic detection components

Coincident radiation exiting from the object is measured by analyzing the output electrical pulses from each detector. Because of scatter the signals resulting from the detection of multiple photons show a continuous energy spectrum as illustrated in Fig. 2.3. The rate and energy distribution of the detected photons are called singles rate and singles spectrum respectively. A finite energy window is necessary to count the photon peak at 511 keV. The electronic circuit mounted near each PMT has a pre-amplifier and two leading edge discriminators. The lower discriminator (E_T = 50 keV) establishes an accurate timing pulse while the higher discriminator (E_L = 300 keV) rejects the low-energy noise and the annihilation photons undergoing large

angle ($> 73°$) scattering. Because of the finite energy resolution of the detector there is also a upper level discriminator $E_H = 650$ keV to increase the detection efficiency.

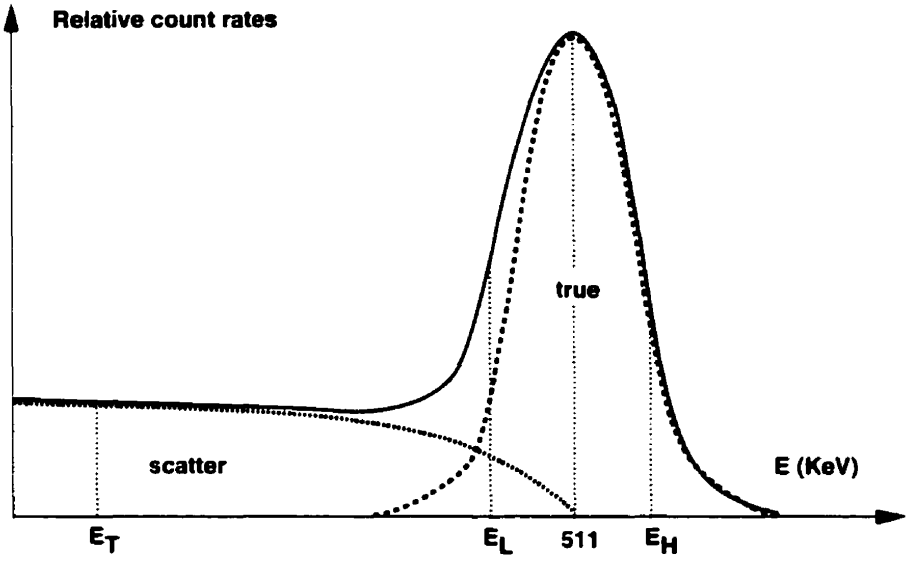

Figure 2.3: Illustration of energy spectrum showing components of scatter (dotted line) and true radiation (dashed line). The true peak at 511 keV is broadened because of the poor energy resolution of the detector. A finite energy window is defined between the low (E_L) and high (E_H) energy thresholds. The signal below E_T is used for accurate timing measurement.

Ideally paired γ-rays from a single annihilation would be detected simultaneously on opposite sides of the object (Fig. 2.4). In practice the time of the PMT signal has a finite uncertainty due to the stochastic nature of the scintillation process. Hence a time window on the order of tens of nanoseconds must be allowed between two pulses deemed to be a true coincidence. Consequently two different types of spurious coincidences are also detected: (a) Two photons from different sites may arrive at a pair of detectors. This leads to accidental coincidences known as randoms. (b) One or both annihilation photons may be scattered before hitting the detector pair and contribute scatter coincidences. In addition the limited response time of the detection

system to process each pulse makes each detector inactive for a short period after each event. There will be data loss in both singles and coincidence rates which is referred to as deadtime. These effects will be discussed further in Chapter 3.

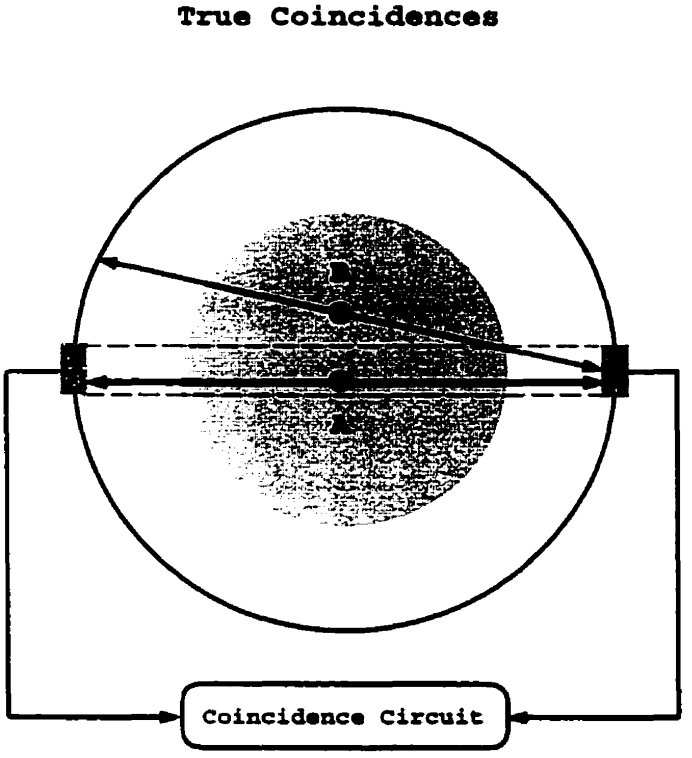

Figure 2.4: Coincidence detection of annihilation photons by two detectors across from each other on the ring. While photons within the volume (between dash lines) register a true event (A) those from outside the volume (B) are rejected by this pair of detectors without satisfying the collinearity condition.

Both the energy window and the coincidence time window must be as large as possible to maximize the true count rates but small enough to keep scatter and randoms to a minimum. As a general rule, desirable scintillators must have short photofluorescent decay times to achieve good timing resolution and high count rates. In addition they should have high stopping power to detect 511 keV radiation efficiently. Equation 2.5 shows that this quantity depends on the 4th-power of atomic number and on

the material mass density.

Table 2.3: Physical properties of scintillators suitable for PET

Scintillating crystals	Decay time (nsec)	Relative light yield	Mass density (g/cc)	Atomic number
Sodium iodide [NaI(Tl)]	230	100	3.67	50
Bismuth germanate (BGO)	300	15	7.13	74
Lutetium oxyorthosilicate (LSO)	42	75	7.40	66
Gadolinium orthosilicate (GSO)	60	16	6.71	59
Barium Fluoride (BaF_2)	0.8	5	4.89	54
Cesium Fluoride (CsF)	3	8	4.64	53

Table 2.3 compares several scintillators for PET imaging. Both sodium iodide (NaI) and bismuth germanate (BGO) have long decay times and inferior timing resolution. This causes larger randoms rates and greater deadtime. BGO crystals have higher stopping power but a much lower light output than NaI crystals. Lutetium oxyorthosilicate (LSO) is a promising new detector with similar stopping power to BGO but yields 5 times as much scintillation light over a much shorter period of time. Cesium fluoride (CsF) and barium fluoride (BaF_2) crystals have very short decay times but much lower stopping power and less light output than BGO crystals. LSO has become available only recently as an optimal choice among these scintillators.

2.2.2 Tomograph design characteristics

One pair of detectors determine the total amount of radioactivity in one dimension only and defines a line of response (LOR) between the two detectors. In order to reconstruct activity density in a cross-section it is necessary to acquire projection data through a large number of LORs. In modern scanners this is achieved with thousands

of radiation detectors surrounding the body in a series of rings. Each ring contains hundreds of scintillators connected by coincidence circuits for electronic collimation. Coincidence electronics are synchronized so as to apply timing discrimination to the measured pulses between each pair of detectors.

PET design aims to detect true coincident count-rates with high resolution and high sensitivity. Derenzo and coworkers have discussed critical issues affecting the design of a perfect PET instrument [Derenzo et al., 1993]. Most commercial scanners are made with BGO crystals on circular rings. These crystals are linked to PMTs in blocks with some form of position encoding. The position of each coincidence event within the block is determined by the relative amount of light collected by each PMT photocathode. This mode allows a large number of small crystals (i.e. 4×4 or 8×8 matrix) to be read by a small number of PMTs (four) to achieve better resolution. High resolution systems have been built using smaller but deep crystals with individual coupling to the PMT. The coincidence time window is normally set from 10 to 20 ns because of relatively poor timing resolution.

In the gantry design there are basically two data acquisition methods: planar and volumetric. Fig. 2.5 and Fig. 2.6 show the sagittal and transverse views of the scanner geometry respectively. In the planar (2-D) mode the thin lead septa are installed between detector rings to define each image plane and shield radiation from adjacent planes [Thompson et al., 1986, Kops et al., 1990, Evans et al., 1991b]. Septa geometry determines the thickness of each slice and limits scatter and randoms from other slices. Thick lead plates outside the axial field of view (FOV) block any external radiation. The entire detector array may also undergo some form of mechanic 'wobble' motion (rotation plus translation) in order to increase data sampling. Compared to the septaless design described below, multi-slice systems have inherently low count

efficiency by detecting only a small fraction of the available photons. However they provide valuable images very economically by minimizing the computational cost.

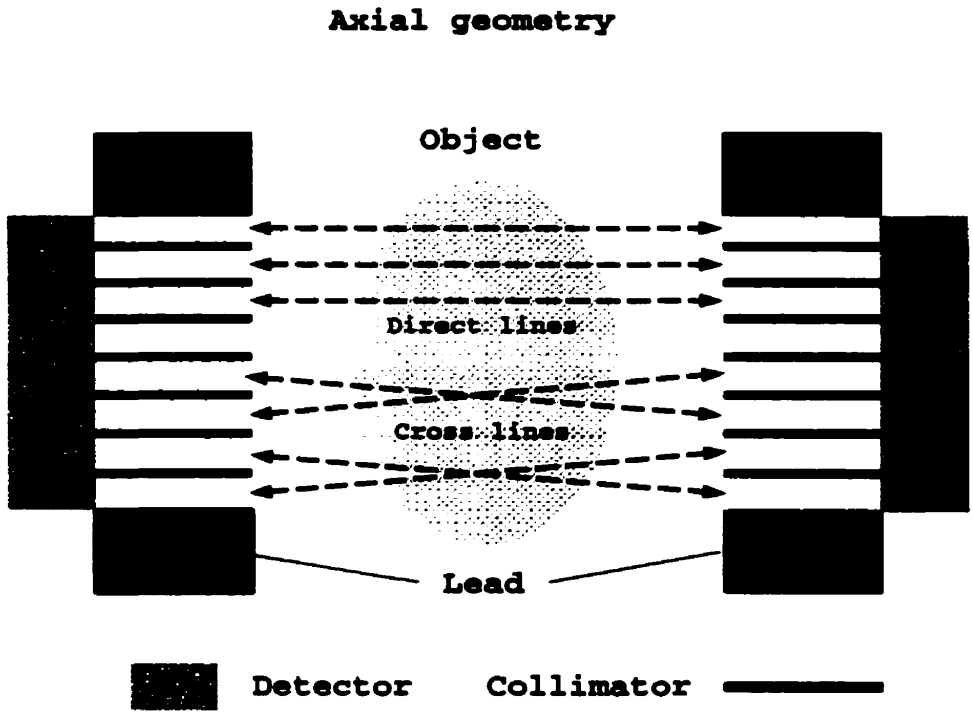

Figure 2.5: Axial configuration of a PET scanner showing coincidence lines of response within and between detector rings. These are used to form direct and cross image planes respectively.

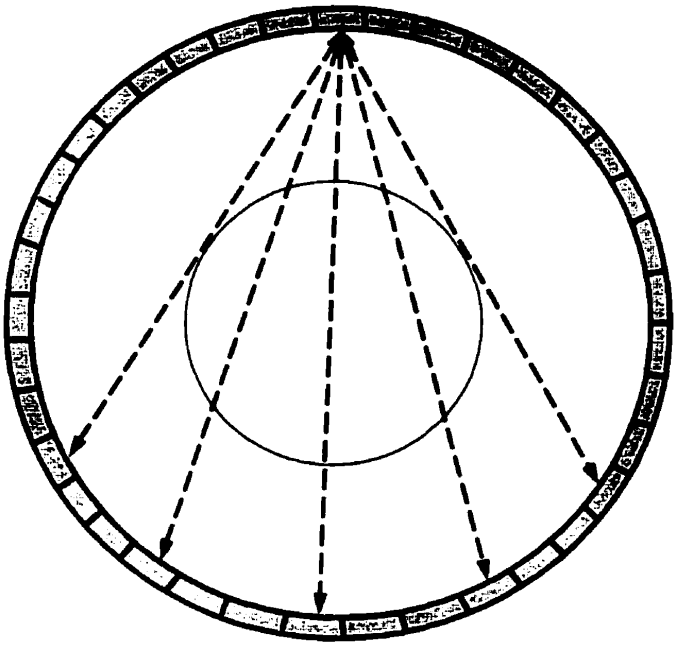

Figure 2.6: Transverse configuration of a PET scanner showing coincidence lines of response that define the imaging field of view.

In volumetric (3-D) mode the lead septa are removed completely to accept counts in a larger axial FOV. This increases the scanner's sensitivity by 5 to 10 times but at the expense of increasing scatter and random rates by a factor of 3. Most current systems have retractable inter-ring septa to allow switching between 2-D and 3-D imaging acquisition options [Spinks et al., 1992, Wienhard et al., 1994, DeGrado et al., 1994, Adam et al., 1997]. Sensitivity can be improved even further in the 3-D only design without septa where the diameter of detector rings can be made smaller to increase the solid angles. This also allows the use of smaller detectors for better resolution.

Other scanners employ large area position-sensitive sodium iodide [NaI(Tl)] crystals as commonly used in SPECT cameras. Generally they are arranged on hexagonal rings without the installation of inter-plane septa [Karp et al., 1993]. Although hav-

ing lower stopping power than BGO they offer much higher light output and better energy resolution. Detectors are connected to a large array of photo-multiplier tubes (PMTs) to measure coincidence data. The position of interaction in the NaI(Tl) crystal is determined by the weighted average of the PMT responses. These systems provide moderately uniform resolution in 3-D.

In a standard PET system the depth information of activity distribution between two detectors is unknown and the data are reconstructed over the whole image plane. Alternatively, resolution and signal/noise ratio (SNR) can be increased by determining where annihilation occurs on the coincidence line. Known as time of flight imaging this technique depends on very fast scintillators to measure differential arrival times of coincident photon pairs. The resulting information is then used to further refine activity localization [Ter-Pogossian et al., 1982. Trebossen and Mazoyer, 1991]. Current detectors (CsF and BaF_2) have timing differences of 0.3 to 1 nanoseconds which correspond to a spatial uncertainty of F = 4.5 - 15 cm. This seemingly inadequate resolution improves the SNR because of low randoms and deadtime as well as smaller reconstruction fields. For instance it can increase the sensitivity of a uniform activity field (diameter D) by a factor of D/F. Assuming F = 5 cm the gain is 3 to 6 times in a 15 to 30 cm diameter cylinder - roughly the area of a human brain and torso. However this type of scanners have lower resolution and efficiency than conventional BGO-based systems. This limitation is largely overcome with the mass production of LSO.

One of the key issues in PET system design is to identify the position of interaction at each crystal so that the observed data can be interleaved and interpolated correctly for image reconstruction. Most scanners determine coincidence LORs based only on geometry assuming the interaction at the center of each crystal. In a cylindrical

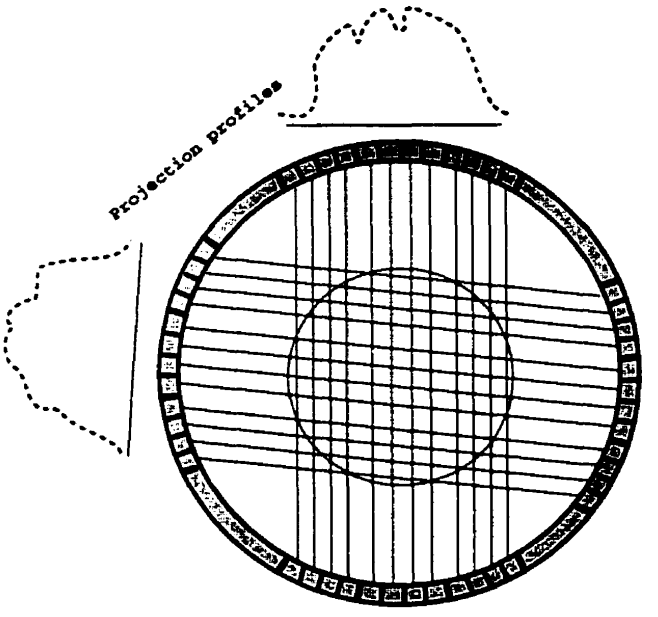

Figure 2.7: Projection data are collected at many different radial and angular positions to form a sinogram.

system their transverse locations are predicted by

$$x = R_e sin(2\pi j/N_d). \qquad j = 0, 1, 2...n \tag{2.6}$$

where $R_e = (D_r + L_d)/2$ is the effective detector radius and D_r is the ring diameter. L_d and N_d are the crystal length and the number of detectors per ring. The presence of small lead septa between the crystal blocks is usually neglected when determining the geometrical location. Thus the LORs in each projection are not equally spaced at a given angle (Fig. 2.7) and the separation decreases from the center to the edge of the FOV.

Historically brain and body scanners are built separately to satisfy their specific requirements. As the technology matured, body tomographs became more commonly used in both applications. With the fabrication of new detector modules high resolution cameras are being made for small animal imaging [Watanabe et al., 1992]. This is desirable to avoid the frequent sacrifice of experimental animals and to validate

new tracers before their use in humans. One recent design employs LSO crystals to achieve a volume resolution of $2 \times 2 \times 2$ mm^3 [Cherry et al., 1997], approximately 10 times better than current clinical PET systems. A more recent innovation is the use of SPECT cameras to detect positron emitters. Some electronic circuits are installed to perform coincidence imaging. Because of the low manufacturing costs this offers tremendous potential in clinical metabolic studies despite the poor efficiency and low resolution this technique has achieved at present.

2.3 Image Reconstruction Algorithms

Data acquisition in a PET scanner handles the forward problem: measurement of a set of projection data from a distribution of radioactive substances. Data at many different angular intervals are collectively referred to as a sinogram. Image reconstruction solves the inverse problem: estimation of internal source distribution from the sinogram dataset. This principle has been used in many scientific and medical fields such as X-ray crystallography and microscopy: and other imaging systems like CT and SPECT. In theory one can even reconstruct MR images from spatially encoded projection data. However the fast Fourier method is used in practice since it is more elegant and accurate.

Mathematically a 3-D source distribution can be faithfully reconstructed if its projections are exactly known around 360^o in infinite numbers of angular and radial positions. It is imperative to understand the notion of the sinogram and its relationship with image reconstruction. Let $f(x, y, z)$ describe certain properties of a physical object in 3-D Cartesian space (x, y, z). Its 2-D projection at each axial position is

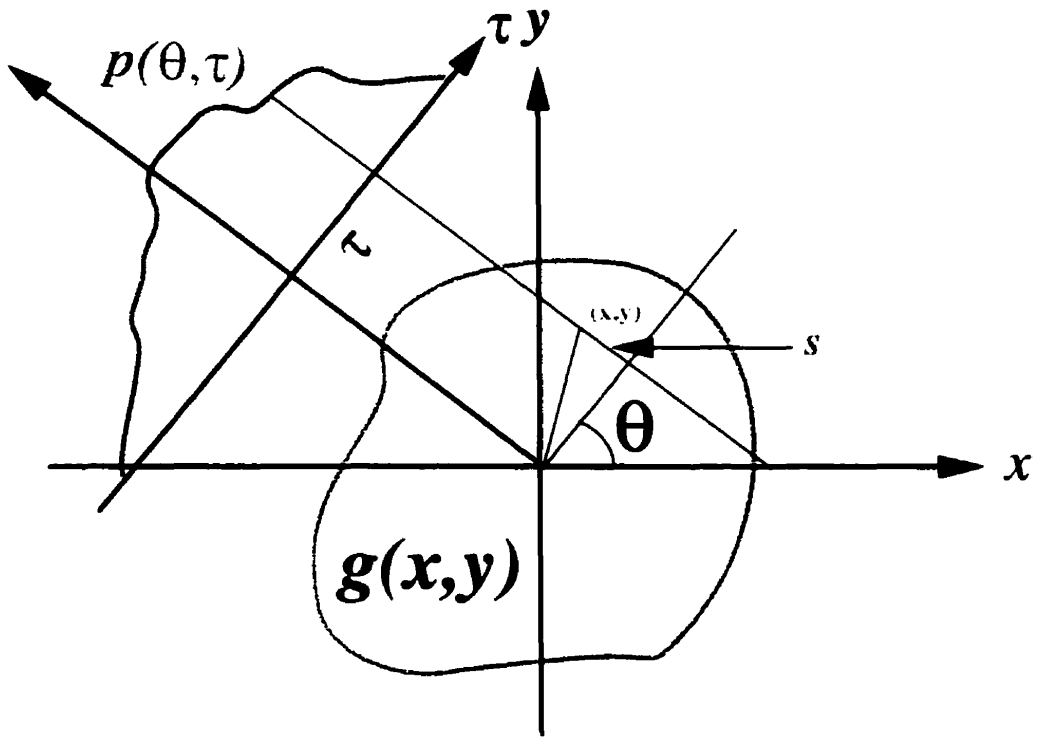

Figure 2.8: Coordinate transformation between image space and projection space. This graph depicts both the forward- and back-projection process.

given by the 3-D Radon transform ($\Re$).

$$p(\tau, \theta, \eta) = \Re\{f(x, y, z)\} \tag{2.7}$$

at ray τ, angle θ and z-position η. We can determine this function by the inverse Radon transform.

$$f(x, y, z) = \Re^{-1}\{p(\tau, \theta, \eta)\} \tag{2.8}$$

There is a direct correspondence between an object function f and its sinogram p. Its simplest form is a sinusoidal for a point source. One can consider any composite sinogram as a weighted superposition of sinusoids of each point source at many different locations in space. For easy discussion we assume that projection is formed perpendicular to the z-axis. In the 2-D condition we can simplify this transformation

by 1-D line integrals as shown in Fig. 2.8.

$$p(\tau,\theta) = \int g(x,y)\,ds = \int\int g(x,y)\delta(x\cos\theta + y\sin\theta - \tau)dxdy \qquad (2.9)$$

where $s(\tau,\theta)$ is the set of parallel lines $\tau = x\cos\theta + y\sin\theta$ with the rotation of the coordinate system given by

$$\begin{bmatrix} x \\ y \end{bmatrix} = \begin{bmatrix} \cos\theta & -\sin\theta \\ \sin\theta & \cos\theta \end{bmatrix} \begin{bmatrix} s \\ \tau \end{bmatrix} \qquad (2.10)$$

We can derive the central slice theorem from equation 2.9 using the Fourier transform (FT). It states that the 2-D FT of $g(x,y)$ along a polar line $G(\rho,\theta)$ is equivalent to the 1-D FT of its projection at the same angle. ρ refers to the spatial frequency in the polar coordinate system. By applying the inverse FT and the convolution property one can then obtain a theoretical reconstruction.

$$\begin{aligned} g(x,y) &= \int_0^{2\pi} d\theta \int_0^{\infty} G(\rho,\theta) exp[i2\pi\rho(xcos\theta + ysin\theta)]\rho d\rho \\ &= \int_0^{\pi} d\theta \int_{-\infty}^{\infty} p(\tau,\theta) * h(\tau)\delta(xcos\theta + ysin\theta - \tau)d\tau \end{aligned} \qquad (2.11)$$

where the projection $p(\tau,\theta)$ at each angle is convolved with the reconstruction filter $h(\tau)$ and then backprojected onto image space according to its angular and radial positions. $h(\tau)$ is the inverse FT of a perfect Ramp filter proportional to ρ in frequency space. Projected data from all angles are summed to give an image. This forms the basis of a general class of reconstruction algorithms called filtered-backprojection (FBP).

In practice, projection data are measured using instruments with finite angular and linear sampling rates. The problem of image reconstruction is then to estimate the source distribution from this limited set of data. We can find unique answers only if we have sufficient numbers of sampled data, consistent with the physical and

statistical characteristics of projection measurement. There are both analytical and iterative solutions as detailed in a historical overview [Cho et al., 1993]. Innovations in this area have laid a solid foundation to fully 3-D image reconstruction in radiology and nuclear medicine.

2.3.1 Filtered-backprojection reconstruction

FBP is the most common method in commercial PET scanners because of its easy and fast implementation. Most often this is done in the real domain:

$$g_i = \sum_{k=1}^{N_p} \sum_{l=1}^{N_r} p_{kl} h_{kl}(x_i cos\theta_k + y_i sin\theta_k - \tau_l) \tag{2.12}$$

where p_{kl} and h_{kl} represent the projection data and the reconstruction filter in the digital forms equivalent to equation 2.11. Note that h_{kl} should be spatially variant in general but an invariant filter is used in practice. In addition it may include any additional interpolations in the backprojection step.

In the ideal case a Ramp filter covering zero to infinite frequency range would be sufficient to generate a complete and accurate image reconstruction. Because of the limited linear sampling and noise in the measured data the Ramp filter is truncated below the Nyquist frequency, above which there can be no useful spatial frequencies from the real data. However, besides amplifying statistical noise inherent in the projection data this also leads to ringing artifacts in the reconstructed image. Both effects can be reduced or removed by additional low-pass filters such as Hanning tapered toward higher frequency. Fig. 2.9 presents several typical Ramp and Hanning filters which produce images with quite different noise and resolution properties as will be seen later in Chapter 6.

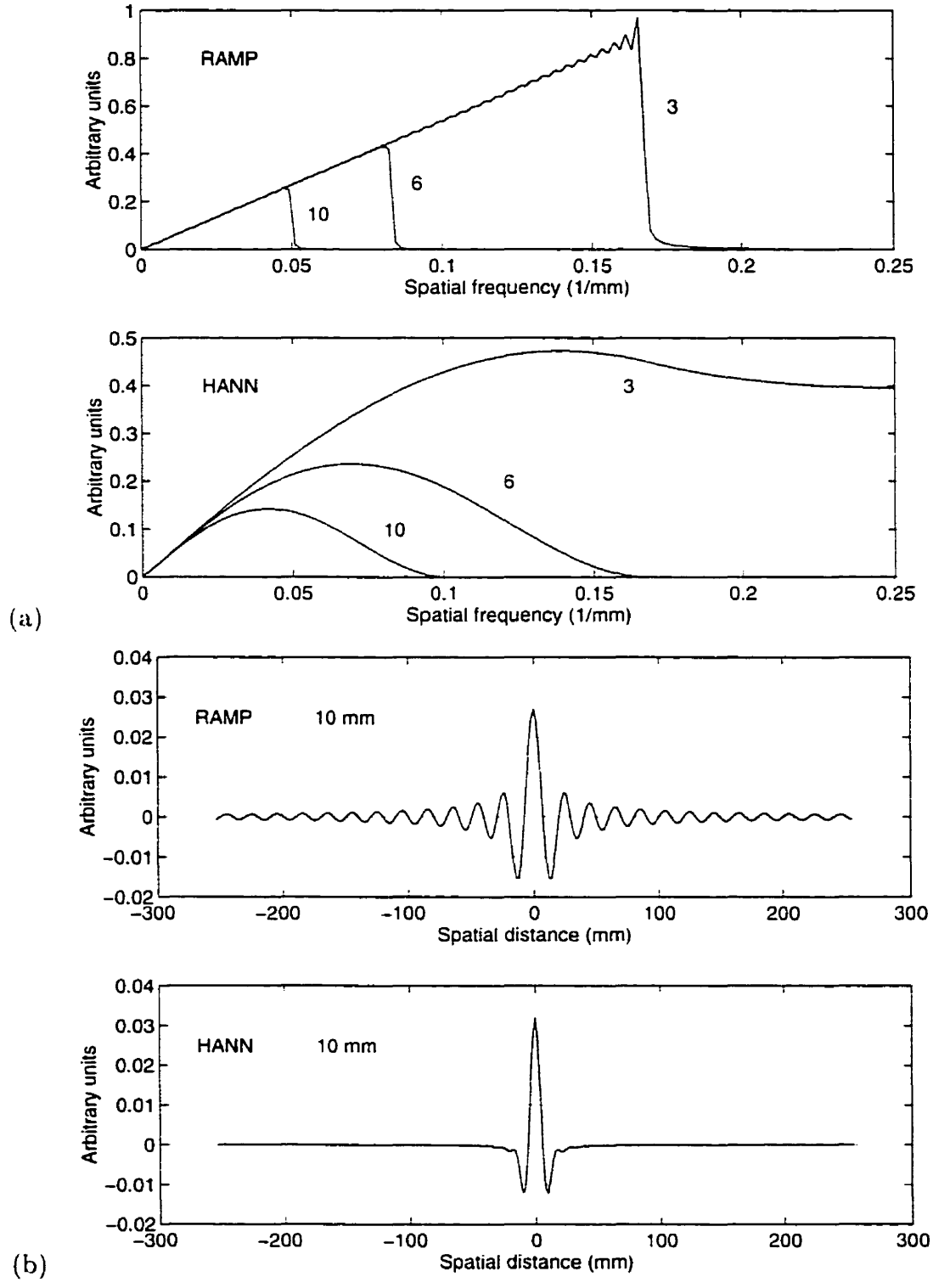

Figure 2.9: Reconstruction filters in both frequency (a) and real (b) domains at different widths in mm.

The FBP algorithm is normally implemented with 1-D convolutions followed by backprojections as shown in equation 2.12. Sometimes one performs the backprojection first to obtain the image and smooth-filtering is then done with a 2-D convolution. We can derive a circularly symmetrical 2-D filter function from its 1-D counterpart. Over the last decade the FBP methods have also been widely used in 3-D PET systems [Defrise et al., 1997]. There are two established approaches: the exact 3-D FBP algorithm based on the inverse 3-D Radon transform and a reprojection step to estimate the missing data. This method takes too much time because of the large numbers of LORs. The other one derives the reconstruction formula from a variety of rebinning algorithms. This algorithm sorts the 3-D acquired data into planar sinograms of independent slices so that they can be reconstructed rapidly with the conventional 2-D method. This is very useful in fast reconstruction of dynamic studies and whole-body imaging. We can realize significant acceleration by doing computations via the Fourier transform.

In most applications h_{kl} is chosen as spatially invariant despite the theoretical argument. Several authors have shown that non-stationary filters are more desirable. Practical solutions include the constrained least squares filtering [Hutchins et al., 1990] and automated bandwidth selection technique [Pawitan and O'Sullivan, 1993]. The first approach performs a partial restoration using a priori tomograph response information. Both allow the design of optimal filter functions adaptive to local noise and resolution variations in the data. In summary the FBP is an analytical approach to image reconstruction based on the Radon transform. It is fast and has been almost universally adopted for commercial tomographic imaging systems. However the method is noisy because the statistical noise in each projection element is spread over the entire reconstruction field leading to a large variance at each pixel.

2.3.2 Iterative image reconstruction

Besides analytical solutions described above there also exist many iterative reconstruction methods in PET imaging. This is motivated by their unique ability to incorporate the physical and statistical characteristics of data acquisition into image reconstruction.

The goal of these approaches is to find estimates of the activity distribution that best match the measured sinogram data. Most early efforts rely on algebra algorithms to iteratively solve a system of linear equations [Hounsfield, 1973]. Besides being computationally expensive they disregarded the unique noise behavior of tomograph data. More efficient formulations have since been implemented, particularly the maximum likelihood (ML)-based methods.

ML reconstruction is derived from expectation maximization algorithm based on Poisson statistics in detection and estimation theory. As in the FBP situation, the original algorithm is initially applied to projection data after post-processing. Theoretically this is not a pure ML algorithm because the noise distributions in the data are no longer Poisson after distortion correction. Many groups have therefore extended it by modeling the entire data collection process [Carson et al., 1994]. The complete equation in emission tomography is as follows:

$$\lambda_j^{(n+1)} = \frac{\lambda_j^{(n)}}{\sum_i C_{ij} A_i N_i} \sum_i \frac{C_{ij} A_i N_i P_i}{P_i^{(n)}} \tag{2.13}$$

with

$$P_i^{(n)} = T_i^{(n)} + S_i + R_i \tag{2.14}$$

and

$$T_i^{(n)} = \sum_k C_{ik} A_k N_k \lambda_k^{(n)} \tag{2.15}$$

where $\lambda_j^{(n)}$ is the current estimate in pixel j at the nth iteration, P_i and $P_i^{(n)}$ are the measured and expected projection counts in ray i, and C_{ij} represents the emission probability from pixel j to ray i with the appropriate 3-D detector response. S_i and R_i denote the scatter and randoms at each ray position with N_i the detector efficiency and A_i the attenuation factor. These physical components need to be determined separately as will be discussed in Chapter 3. We use data estimated explicitly from the imaging experiment to obtain the true counts T_i and other variables. Iterations are initialized by the image reconstructed from FBP to speed up convergence. C_{ij} is a sparse matrix determined by the scanner geometry. It is usually computed beforehand and stored in a file for each tomograph.

Iterative methods can reconstruct unbiased images whose quantitative quality is otherwise compromised by the limited counting density and physical characteristics of the imaging system. Because of the ill-posed nature of the problem, additional *a priori* information has often been introduced to regularize the reconstruction process. Typical priors include time-of-flight constraint [Politte, 1990] and structural boundaries [Ouyang et al., 1994] or Bayesian line sites detected between assumed tissue types in PET image data [Bowsher et al., 1996]. With recent progress MRI-guided ML and Bayesian reconstruction algorithms have become a reality.

The key obstacle of this methodology in the past has been the intensive calculation involved in each iteration. Many iterations are usually necessary to yield clinically useful images. This problem has been more or less solved with improved computer hardware and more efficient implementation, notably the ordered subset formulation [Hudson and Larkin, 1994] which offers a huge speed improvement. In conclusion this fundamental approach allows image restoration on a pixel basis when a realistic model of the scanner is used.

2.4 Data Analysis with Regions of Interest

The reconstructed images are analyzed to generate time-activity curves in selected functional regions of interest (ROI). The mean activity and variance in each ROI are calculated by

$$t_j = \frac{1}{M}\sum_{i=1}^{M} g_i m_i \qquad v_j = \frac{1}{M-1}\sum_{i=1}^{M}(g_i - t_j)^2 m_i \tag{2.16}$$

where g_i refers to the image value at each voxel and m_i is the binary representation of each regional mask with M pixels. Values from different slices of the same structures may be averaged to obtain estimates for each volume of interest. This step usually decreases ROI variability and variance.

By inserting equation 2.12 into equation 2.16 and changing the order of summation one can show that the convolution with the raw sinogram data is replaced by that with the projection of each ROI template [Klein et al., 1997]. It allows calculation and reuse of intermediate vectors at each angle for a given filter function and ROI set. Thus regional activity estimate and variance can be computed directly from sinogram data without image reconstruction. This is particularly useful in dynamic studies by applying the same intermediate terms to each frame. Considerable speedup can be achieved in 3-D systems by avoiding reconstructions of entire images over many frames.

Before accurate regional identification one must address the question of function-anatomy correspondence. It is known that metabolism and blood flow distributions reflect gray matter anatomy to a large degree in normal subjects. This would not be true in pathological conditions such as brain tumors and other neurological disorders. Many other tracers show little structural content as in some receptor ligands and oxygen or glucose extraction fraction. Thus the use of functional data to infer

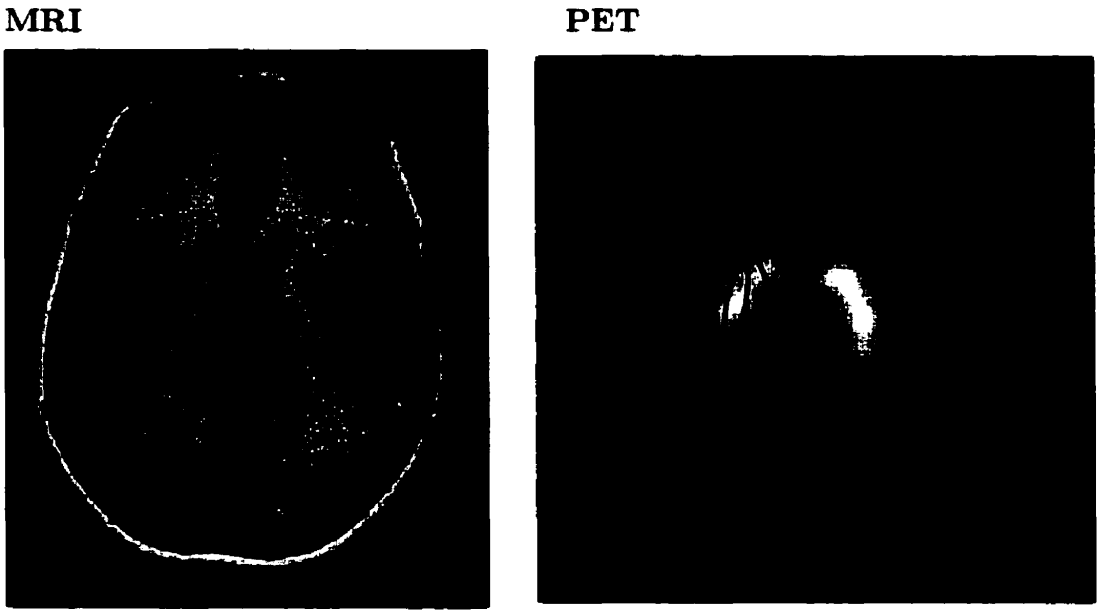

Figure 2.10: The use of co-registered MRI-PET image data to draw regions of interest according to neuroanatomy. MRI shows high contrast between gray matter, white matter and ventricles as well as good delineation of anatomical structures. ROI templates are superimposed onto low resolution, neuroreceptor PET images with high specific tracer uptake in a few small structures.

anatomical correlation is not always applicable. This problem remains despite the improvement in PET image resolution.

In principle, functional regions should be drawn over structures with unique and uniform tracer uptake. There are two general approaches: direct and indirect ROI selection strategy based on anatomical data. Originally these were selected directly from a single PET image. This has very limited values due to low image resolution and poor counting statistics (c.f. Fig. 2.10). The situation is improved slightly by summing all or part of the dynamic frames. With this approach ROIs are often misplaced across structural boundaries because of anatomical distortions inherent in PET images.

Indirect methods employ the matched MRI/CT images to define geometrical and anatomical templates. Fig. 2.10 shows MRI-PET registration with corresponding anatomical ROIs overlaid on both images. Regional data can also be extracted using a customizable 3-D computerized brain atlas [Greitz et al., 1991, Evans et al., 1991a]. With better guidance, this approach improves both accuracy and precision of regional activity determination. Most registration methods depend on anatomical features visible in each modality. Their accuracy can be increased by using the summed PET images or static frames with the highest structural information, which can be matched to corresponding features in the anatomical image. Others use external fiducial markers mounted on a head holder and filled with contrast agent (copper sulfate and radioactive solution).

The combination of PET and MRI data offers a unique opportunity to perform structure and function correlation in the body. It also allows accurate localization of active functional areas in neuroimaging studies. The main problem is the need to register 3-D MRI and PET image volumes collected at different times from the same brain. We can avoid this problem by doing simultaneous MRI/PET imaging with both functional and anatomical information. This novel concept has been demonstrated experimentally in a prototype [Shao et al., 1997]. It will permit perfect image registration and direct comparison between functional MRI and PET activation data.

2.5 Estimation of Physiological Parameters

PET is used to study kinetics of tracer uptake in a wide variety of biochemical systems under living conditions. Labeled compounds in the blood pool are transported across biological barriers, and accumulate in specific tissue areas over a period lasting from a few seconds to many minutes depending on the tracer. While providing quantitative

data of regional radiotracer concentration, its major attraction is in the temporal dimension where serial scans can be done repeatedly in the same human or animal subject. This leads to widespread use of dynamic PET imaging methodology to extract parametric information of tracer uptake from measured TACs and plasma curves. Evolution over last 20 years has made PET a clinical diagnostic imaging modality in neurology, cardiology and oncology.

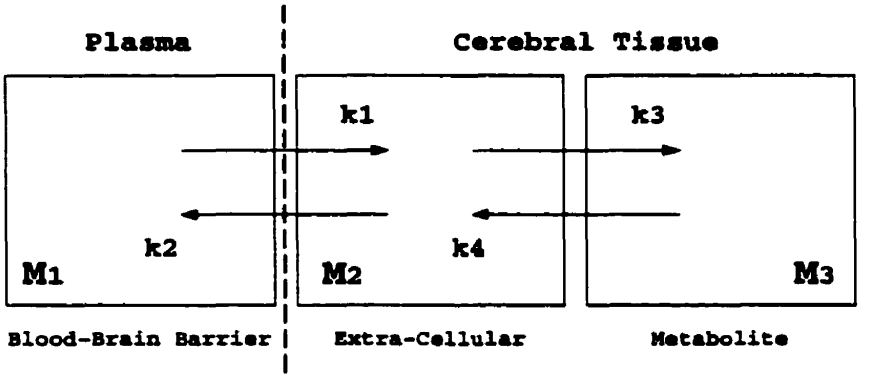

Figure 2.11: Generalized three-compartment model depicting transport of tracer and its derivatives between vascular space and tissue components.

2.5.1 Compartmental models of tracer kinetics

Many new tracers have been synthesized in recent years and there are great increases in viable kinetic models to extract accurate physiological parameters. Besides common methods to measure cerebral blood flow (CBF), metabolism and neuroreceptor density we have also seen secondary or tertiary parametric images and multi-tracer composites resulting from intra- and inter-subject correlation.

The basis of quantitative PET imaging is a comparison of the tracer TAC in plasma with that in the brain. The movement of tracer from plasma to the tissue is assumed to be described by a set of first-order rate constants which can be estimated

from a compartmental analysis of the tissue and plasma TACs at every voxel in the image. We use a three-compartment model (Fig. 2.11) to illustrate the general concept of kinetic analysis in PET studies. This is derived from the principle that rate of transport out of a compartment is proportional to the tracer concentration in the compartment. The basic operational equations are given by

$$\frac{dM_2}{dt} = k_1 M_1 - (k_2 + k_3) M_2 + k_4 M_3 \tag{2.17}$$

and

$$\frac{dM_3}{dt} = k_3 M_2 - k_4 M_3 \tag{2.18}$$

where M_i refers to the total mass of tracer in each compartment and k_j the transfer coefficient between them [Gjedde and Wong, 1990]. k_1 and k_2 are the influx and efflux constants describing the rates of tracer delivery and recirculation. k_3 and k_4 are the exchange rates between two chemical species in the tissue compartment which describe metabolic or receptor binding processes. This model reduces to a 2-compartment system when $k_3 = k_4 = 0$. Note that $M_1 = V_1 C_a$ where C_a is the time course of tracer concentration in plasma called input function. V_1 is the volume of distribution with $K_1 = V_1 k_1$ defined as plasma-tissue clearance.

PET scans are usually done with arterial sampling although blood samples can also be taken from the arterialized (heated) veins. However plasma concentration may differ between arterial and venous blood. Before measurement in a well counter, blood samples often undergo high-performance liquid chromatography analysis to determine the fractions of the free (unmetabolized) tracer and its metabolites in the plasma. This is necessary to obtain a more accurate plasma input function.

Compartmental analysis solves these differential equations within practical constrains. However the solution to the equations and the interpretation of the rate

constants depend very much on the tissue and radiotracer involved. Generally this is done by nonlinear regression such as weighted least squares. It is important to correct tracer delay and dispersion between the tissue TACs and the blood input function [Meyer, 1989]. Most analysis is done on a regional basis although one can also generate 3-D parametric images by applying the kinetic model to each voxel. This approach avoids the need for assumptions of ROI homogeneity at the cost of noiser parametric maps. In the sections below we briefly describe three major categories and cite some recent references.

2.5.2 Blood flow and metabolic imaging

O-15 labeled water, carbon dioxide, carbon monoxide, and oxygen gas are commonly used to measure regional blood flow, blood volume and metabolic rates of oxygen. In most studies CBF is determined by the intravenous $H_2{}^{15}O$ bolus method or following $C^{15}O_2$ inhalation [Lammertsma et al., 1990]. $C^{15}O$ and $^{15}O_2$ are inhaled to obtain blood volume and oxygen extraction fraction (OEF) respectively. Their values are very sensitive to blood pressure in the artery. Local oxygen consumption is then estimated by multiplying CBF with OEF and arterial oxygen content. It has been shown that this quantity can be determined in one step after a bolus inhalation of $^{15}O_2$ with a two compartment model [Ohta et al., 1996]. Other authors have demonstrated the possibility of estimating these variables simultaneously from a single $^{15}O_2$ study collected in dynamic mode over 3 minutes.

Local glucose metabolic rates are measured with F-18 labeled fluoro-2-deoxy-D-glucose (FDG). 2-deoxy-D-glucose is used because regular glucose is too rapidly metabolized to carbon dioxide and water. This compound accumulates in tissue in direct proportion to glucose utilization. A typical study begins with a 40-60 min delay for

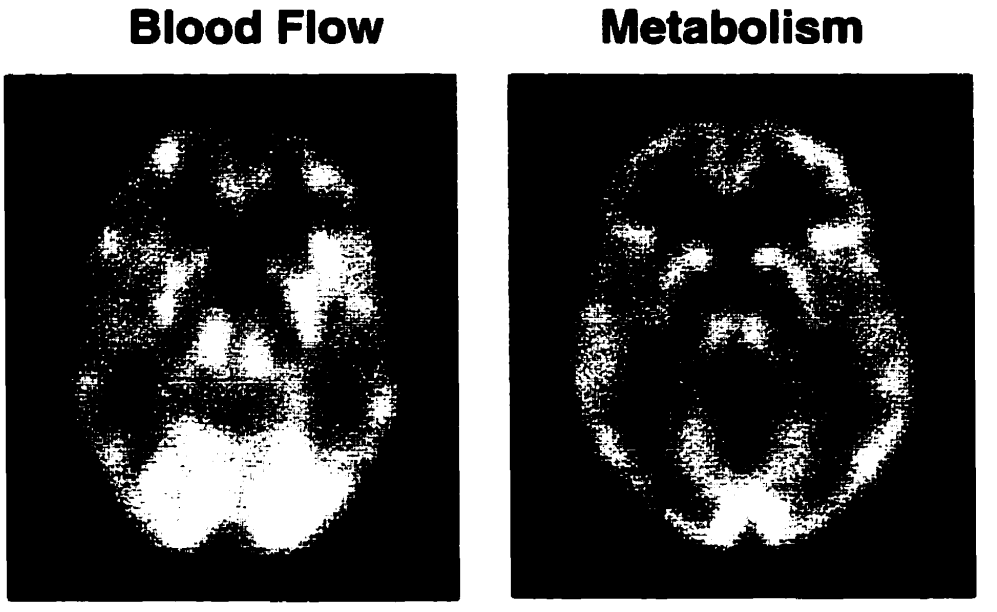

Figure 2.12: Representative PET images of cerebral blood flow and glucose metabolism from a normal human brain showing a dominant distribution throughout gray matter and white matter structures.

the tracer to reach equilibrium with the plasma, followed by a 15-60 min dynamic scan. A three-compartment model with four rate constants is usually assumed to analyze data [Schmidt et al., 1996]. FDG is the most natural choice in the study of human cerebral function since the brain consumes about 80 % of glucose in the body. Numerous studies have been done to identify characteristic patterns of many neurological diseases [Eidelberg et al., 1995] and examine functional impairment from drug addiction [Stapleton et al., 1995]. It is now possible to measure these physiological variables on small animals with the steadily improving image resolution in the new generation of PET scanners [Heiss et al., 1995]. This allows quantitative comparison across different species and validation of animal models.

PET with FDG and N-13 labeled ammonia has become a standard procedure to evaluate myocardial viability in cardiovascular applications. Both provide quantita-

tive measures for cardiac blood flow and metabolism. The myocardial viability is then determined by the mismatch between these two variables [Beanlands et al., 1997]. Because of its high uptake in tumors FDG has been the most useful tracer for assessing metabolic abnormality in oncology. Recent studies include breast cancer imaging with a dedicated positron mammography system [Bergman et al., 1998]. Besides early detection of the disease this also allows us to monitor and examine the efficacy of cancer therapy.

2.5.3 Radioligand receptor imaging

One of the most important applications of PET is in quantifying brain function associated with neurotransmission. This concerns the study of the transmitter recognition mechanism by which neurons communicate with each other. Receptor changes have been observed in post-mortem data with normal aging and mental disorders like schizophrenia. It is also known that Parkinson's disease results from a deficiency of dopamine activity in striatal structures. F-18 and C-11 based radioligands have become widely available to probe metabolism and receptor-ligand interactions in the human brain.

While the tracers in CBF and FDG studies are distributed globally in cerebrum (Fig. 2.12), those used in neuroreceptor imaging are localized specifically in central structures such as basal ganglia and thalamus, with much less uptake in cerebral cortex (Fig. 2.10). Most work has been done to examine pre- and post-synaptic processes involving dopaminergic neurons. With F-18 fluoro-L-dopa (Fdopa) PET can measure the rate of dopamine synthesis [Kuwabara et al., 1993, Takikawa et al., 1994]. This is typically done with a 90 min dynamic scan after 5 mCi Fdopa injection. Importantly these data can be analyzed without taking blood samples [Lammertsma et al., 1996,

Logan et al., 1996]. This is based on the assumption that there is negligible tracer uptake outside striatum and an input function can be derived from TACs in cerebellum or occipital cortex.

Clinical studies have shown that the amounts of dopamine receptors and transporters are reduced in many neurodegenerative processes. This has recently been demonstrated in Huntington's disease and Parkinson's disease using C-11 raclopride and F-18 FPCIT respectively [Ginovart et al., 1997, Kazumata et al., 1998]. In particular the reductions of binding potentials in the striatal structures are correlated significantly with increasing duration and serverity of illness.

PET can localize and measure the distribution of neuroreceptors by detecting sub-nanomolar concentrations of labeled compounds or drugs. This offers the unique potential to evaluate the efficacy of therapeutical drugs in both animal models and human volunteers. Because of these advances PET has become an indispensable tool to understand the function and dysfunction of the central nervous system.

2.5.4 Physiological activation imaging

With O-15 water multiple blood flow scans can be performed rapidly because of the short half-life of O-15 and the high temporal resolution of PET. This has become a powerful imaging tool to localize areas of brain activation based on regional CBF changes. Its goal is not to measure absolute CBF values but rather the difference between distinctive functional states or during external stimuli. Image pairs between activation and baseline conditions are subtracted and averaged together to improve the S/N ratios (SNR). Data are then analyzed using several different methods to generate statistically significant activation maps. Most often this is done by calculating the t-statistic over the brain volume and identifying areas of significant focal

change in CBF [Worsley et al., 1996]. The theoretical formulation is based on the Gaussian random field concept [Worsley et al., 1992] and the general linear model [Friston et al., 1995]. Because of the non-quantitative nature of the method it is no longer necessary to perform dynamic scan and blood sampling as in quantitative measurement. This greatly simplifies the study protocol and increases productivity.

This approach has been implemented with both intra- and inter-subject averaging. Their selection depends on the activation tasks and the SNR achievable with the particular partition of a given radiation dose. One can apply the intra-subject paradigm when the expected activation is large enough to be detected in a single subject experiment. However, in cognitive studies involving more subtle CBF changes, inter-subject averaging is often necessary to increase the SNR. Before subtraction the paired image volumes are normalized to the identical total activity level and transformed into the same 3-D coordinate space [Evans et al., 1992a]. The difference images from multiple subjects can then be combined to produce a composite statistical map of change.

While O-15 water is the most popular choice for activation studies, other radiotracers have also been used to measure the change in brain energy supply and demand during neuronal stimulation. Increases in oxygen and glucose uptake are observed in the visual cortex during continuous light flash. It has been shown that change of glucose metabolism to vibrotactile stimulation can be measured accurately in a single 60 min FDG scan [Murase et al., 1996a]. Studies like this give important answers to the coupling and uncoupling questions of local cerebral oxygen/glucose consumption in both controls and diseases.

2.6 Summary

PET is based on the principle of image reconstruction from projections to measure the regional distribution of many medically important radioactive compounds in the body. It has revolutionized fundamental biological sciences by imaging normal/abnormal function in both humans and animals noninvasively. It has become a viable diagnostic tool in the management of many types of diseases.

Clinical PET imaging protocols address two basic areas. The first concerns the derivation of kinetic models in both normal and disease and is based on biological factors. We are interested in technical factors which affect the optimal use of the imaging methodology. These include not only temporal sampling schedules but also parameter estimation algorithms. The outcome of any study depends critically on the accuracy and precision of the measured image data. In order to improve the protocol design it is necessary to discuss the quantitative capabilities of PET imaging systems.

Chapter 3

Quantification Problems in PET Imaging

A PET imaging system is designed to provide quantitative measurement of regional radiopharmaceutical concentrations in the human body as a function of space and time. This means that each voxel in the image represents the true concentration at that position. However the accuracy and precision of the measured values are reduced because of the presence of many physical distortions inherent in data collection and image reconstruction [Hoffman and Phelps, 1986]. This chapter describes the primary error sources affecting regional radioactivity quantification and discusses projection data correction methods commonly used in practice. It also presents a theoretical analysis of the signal-to-noise problems in PET data.

3.1 Sources of Data Distortion

A PET camera is a sophisticated instrument which collects coincidence data between thousands of detector pairs within a finite time window and a limited energy window. Because of technical limitations, scan data must undergo digital processing to estimate

and correct physical distortions in the measured coincidence rates.

3.1.1 Deadtime effect

As radioactivity levels in the field of view (FOV) increase the ability of the PET scanner to distinguish individual pulses becomes limited due to the delay in crystal response and coincidence electronics. This is known as deadtime effect and leads to a count-rate dependent loss of events. The higher the input rates the lower the observed count rates. It is determined mostly by the total singles rates encountered by each detector block since singles rates are generally much higher than the coincidence rates.

Deadtime may cause a substantial reduction in the measured data and distort the shape of time-activity curves in dynamic imaging studies. Deadtime correction in a PET system depends on both the singles rates in each detector and the coincidence rate [Daube-Witherspoon and Carson, 1991]. This behavior is usually determined using a large diameter flood source decaying over a wide activity range.

3.1.2 Accidental coincidences

This event takes place when two independent annihilation photons are detected within the coincidence time window (Fig. 3.1). The probability of two random photons reaching a detector pair is given by

$$R_k = 2t_c S_i S_j \tag{3.1}$$

where S_i and S_j are the singles rates in two detectors and $2t_c$ the width of the coincidence time window usually measured in seconds. Because the singles rate in any detector is linearly related to total activity in the FOV the randoms rate is proportional to the square of activity distribution. It adds a uniform background

to the measured projection data which becomes dominant at high count rates. Its contribution can be reduced by shortening t_c and counting at lower singles rates.

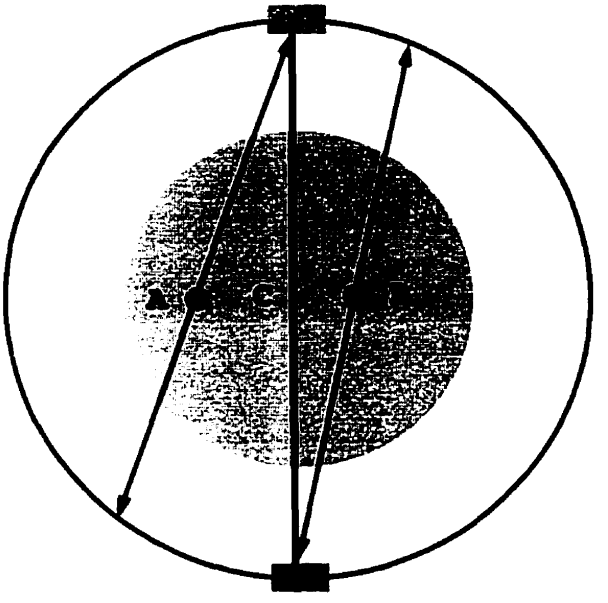

Figure 3.1: Illustration of accidental coincidences (randoms) in PET data collection. A and B represent two independent true events each giving rise to 2 colinear γ-rays with C depicting an apparent coincidence between the two unrelated γ-rays.

Two methods are used to correct randoms. (a) Randoms rate is recorded simultaneously in a separate channel delayed beyond the main time window. Randoms determined in this channel are subtracted from the total count rates automatically during data collection. The main problem is the poor statistics in randoms measurement which will increase image variance after the subtraction. (b) Randoms rate is estimated from the observed singles rates in each detector using equation 3.1. Randoms are then subtracted from the total data to give the true coincidence rates. S_i and S_j can be measured very accurately to calculate the randoms with negligible noise.

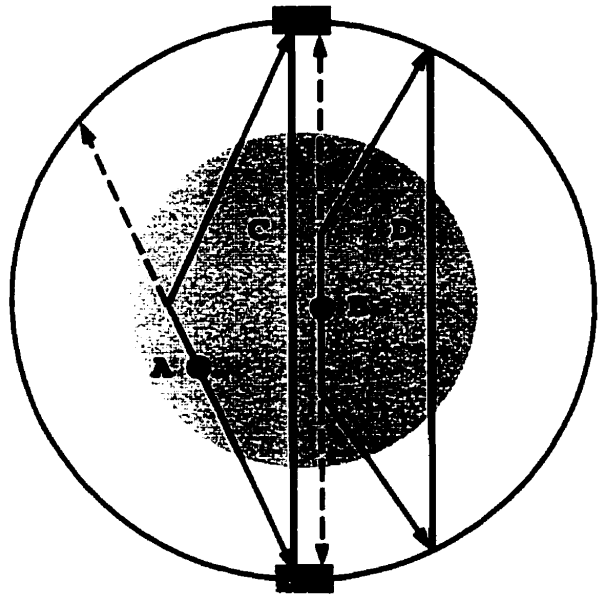

Figure 3.2: Illustration of scatter coincidences in PET data collection. It shows cases where one or both of the two annihilation photons from positron emitting atoms (A) and (B) are scattered to form apparent lines of response (C) and (D) respectively. Scattered γ-rays cause displacement of the true source position.

3.1.3 Scatter coincidences

This occurs because some of the recorded photons undergo Compton scatter in the object and collimators on their way to the detectors. Both effects displace the true location of the annihilation events as shown in Fig. 3.2. Its probability depends on both the activity distribution and the attenuation properties of scatter medium on the path of projection lines.

The relative importance of scatter is described by the scatter fraction $S/(T+S)$ with S and T being the scatter and true rates integrated over sinogram space. Scatter is minimized by proper selection of the energy discriminator. In current PET systems the scatter fraction is 10-15 % in brain studies with septa and increases to 40-60 %

after septa removal. The values are higher in body imaging because of the larger object size. Scatter effects generally overestimate radioactivity concentration and degrade image contrast, and must be excluded from projection data.

Scatter rates can not be measured directly in projection space. Its distribution can be estimated by analytic modeling and then subtracted from the total data. This is normally done by a deconvolution algorithm with a spatially variant scatter filter function. This function is determined by scanning line sources in a water phantom across the imaging field of a tomograph [Bergstrom et al., 1983]. The profiles are extracted with randoms correction and efficiency normalization to generate a set of line-spread functions (LSF) at different locations. Fig. 3.3 plots a typical LSF on a semi-log scale to emphasize the exponential scatter component below the peak. By fitting the data to asymmetric mono-exponentials one can extract the scatter profile and the true peak at each position. We can then obtain a convolution filter from their shapes:

$$f_s(\tau, \tau') = \alpha(\tau) exp(-\beta(\tau)|\tau' - \tau|) \tag{3.2}$$

f_s gives the scatter profile when operating on the peak profile of the LSF. It will be useful in simulation to estimate scatter from true projection data. α is the amplitude and β is the slope with different values on the left and right sides of the peak position away from the center. Both vary with the source position τ but have only a weak dependence on the depth in the object. To reflect the spatial variation of the scatter medium the magnitude depends on the photon path-length inside the object. Note that the intensity of scatter in any material increases with this quantity.

In order to remove scatter from the total data we usually derive another filter h_s whose convolution with the LSF in water gives the same scatter profile. Since both

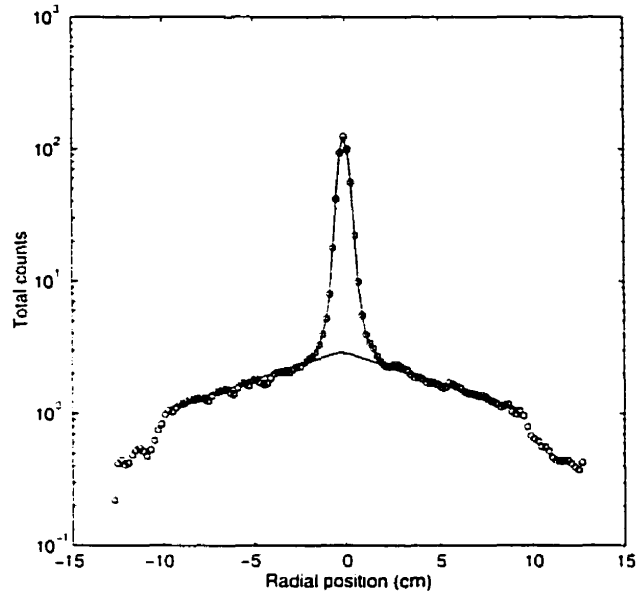

Figure 3.3: A typical line source profile (o) measured at the center of a 20 cm water phantom. Counts outside and under the peak come from scatter only. Note that the line through the tails is generated by convolving the line through the peak with the scatter filter function.

filters can be derived from the same set of data they are related by

$$h_s = f_s(I + f_s)^{-1} \qquad f_s = h_s(I - h_s)^{-1} \tag{3.3}$$

where I is the identity matrix. Consequently one can obtain either filter from the other by matrix inversion.

The second filter is used in most commercial systems to correct scatter counts from the measured projection data after random correction.

$$S_k = \int h_s(\tau, \tau')p(\tau')d\tau' \tag{3.4}$$

Because the scatter distribution is relatively smooth this is done every five angles to reduce computation time. The center of the object and the photon path-lengths in each projection are calculated from the attenuation data described below. By

analyzing the scatter response functions of point sources Shao et al have extended the deconvolution algorithm to volumetric data acquisition [Shao and Karp, 1991]. In an experimental study Bentourkia et al decomposed scatter contributions from object, collimators and detectors [Bentourkia et al., 1995a]. Their results show that the basic concept and functional forms also apply to each scatter component.

Recently several groups have investigated scatter correction methods based on data acquired over several energy windows [Shao et al., 1994, Bentourkia et al., 1995b]. Scatter counts in the main energy window are estimated from those in the lower energy windows and then subtracted on line. The energy resolution of BGO detectors is normally worse than 20 % in FWHM at 511 keV making it difficult to remove scatter by energy discrimination. This approach works to a large degree in NaI(Tl) detectors with higher energy resolution. Generally there will still be some residual scatter which can further be removed with the deconvolution algorithm. Model-based new methods have also been implemented for scatter correction in fully 3-D PET scanners [Ollinger, 1996].

3.1.4 Photon attenuation

Because of the Compton and photoelectric interactions, most γ-rays generated from positron-electron annihilation are absorbed in the body. This is the largest distortion source in PET imaging studies. In brain scans only about 20 % photons escape without interaction as compared to 10 % in a cross section of the human chest. The probability of two photons reaching a pair of detectors in coincidence is described by

$$P_{12} = e^{-\mu a} \times e^{-\mu b} = e^{-\mu(a+b)} \tag{3.5}$$

where a and b are the path lengths of two photons over a uniform object of attenuation value μ (Fig. 3.4). Therefore photon attenuation is determined by the total path-

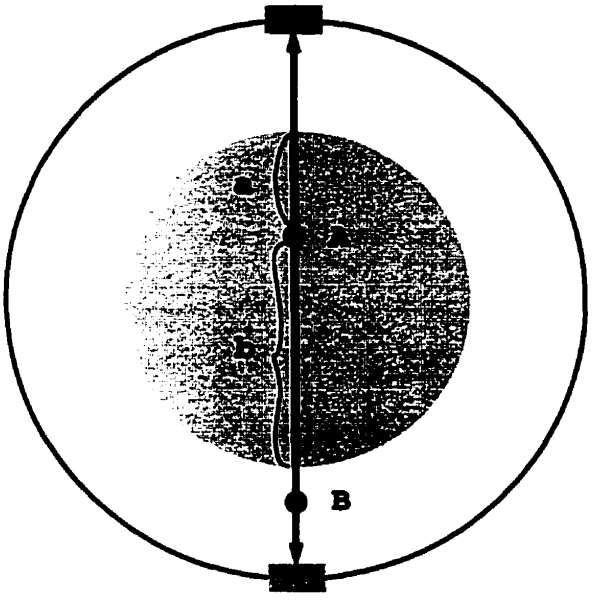

Figure 3.4: A diagram showing depth-independent photon attenuation in PET data collection. Photon pairs originating from inside the object (A) or outside the object (B) have the same probability of being detected as a true coincidence (equation 3.5). a and b are the distances that each photon passes through the object.

length ($L = a + b$) and is independent of the location of the positron source along each line of response. This is a key advantage of PET imaging since one can correct attenuation effects more accurately. In SPECT the likelihood of photon attenuation is a function of the depth of the emitting particle (which is unknown) and attenuation compensation has been a major source of inaccuracy.

In general there is some spatial variation in attenuation property between different tissues and attenuation correction factors are defined as:

$$ACF = exp(\int \mu(x, y)ds) \tag{3.6}$$

where $\mu(x, y)$ is the attenuation map of the object and ds the photon path length along each projection line. Thus the ACF is determined merely by the geometrical

contour of the structure and tissue attenuation values in the body. This allows theoretical calculation from the geometry and average μ of each structure. The body contour is determined from emission projection data or reconstructed images without attenuation correction. This technique is only suitable in semi-quantitative brain studies where attenuation is more or less uniform among soft tissues. Additionally the head contour is easier to identify than that of the torso in a cardiac scan. The method works better with some uptake in the skin and is not applicable to early frames of CBF/FDG or receptor imaging.

In most applications photon attenuation is corrected by transmission scans as in a modern CT system. As shown in Fig. 3.5 an external positron source is attenuated by the object in the same proportion as in the emission scan. The coincidence circuitry is used to locate the rod position. One blank scan and one transmission scan are acquired independently before activity injection. The ACF at each position is then determined from the ratio (c.f. equation 2.2),

$$ACF = I_B / I_X \tag{3.7}$$

where I_B and I_X are the blank and transmission count rates. I_B is normally much larger than I_X and thus has smaller variance but larger deadtime problems. Therefore the ACF is calculated after performing deadtime correction in each scan as well as decay correction to account for the time difference between the two scans. Emission data are then multiplied by this factor at each projection element.

This approach is more accurate but noisy. Transmission data are generally less noisy than the emission data but suffer from more deadtime due to the high count rate of the rod source. To suppress noise propagation from attenuation correction blank and transmission data are smoothed with a normalized Gaussian filter. New scanners install multiple orbiting line sources for better statistics.

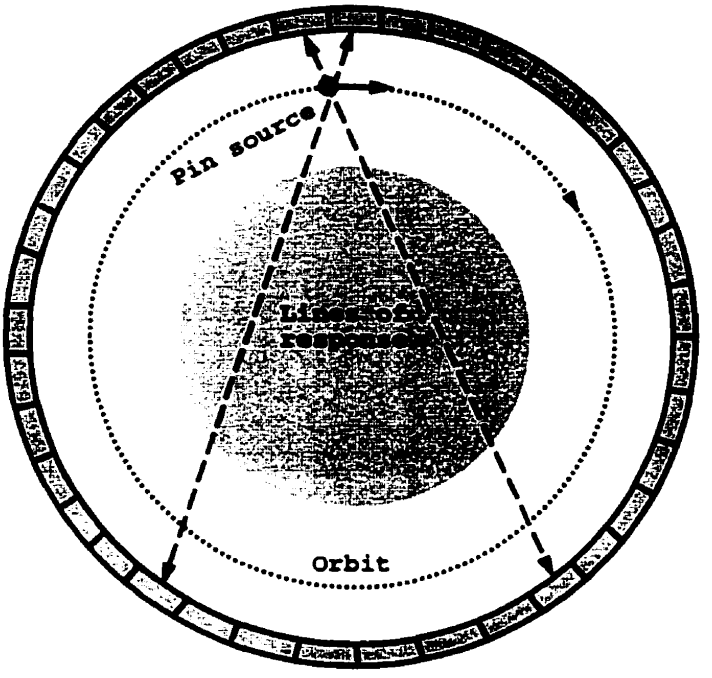

Figure 3.5: Geometrical configuration of PET transmission scans with a pin source rotating around the center of the gantry. Detectors accept only the lines of response passing through the pin source.

The primary purpose of the transmission scan is to measure attenuation correction factors directly. However equation 3.6 and 3.7 can be rearranged to yield

$$\int \mu(x,y)ds = ln(I_B/I_X) \tag{3.8}$$

This allows us to reconstruct images of the tissue attenuation coefficient using the method described in section 2.3. Since the reconstruction filter is also a Gaussian-type function (FWHM $= w_f$) the transmission images have a combined filter width $w_t = \sqrt{w_s^2 + w_f^2}$, where w_s is the FWHM of the smoothing filter. It is known that this method has smaller variance despite the nonlinear logarithmic operation involved in image reconstruction. On some occasions it is also useful to aid registration between MR and PET images with less anatomical features (e.g. neuroreceptor study).

Early PET systems use a stationary hoop source to collect blank and transmission data. It has been known that this source contributes substantial scatter and randoms as in the emission scan. With the current design of an orbiting Ge-68 rod source the undesired radiation is greatly reduced by the use of sinogram windowing mechanism [Jones et al., 1995]. This is done by accepting only coincidence lines that intersect with the instantaneous position of the source. There may still be some scatter and randoms remaining in both blank and transmission data depending on the width of the sinogram window.

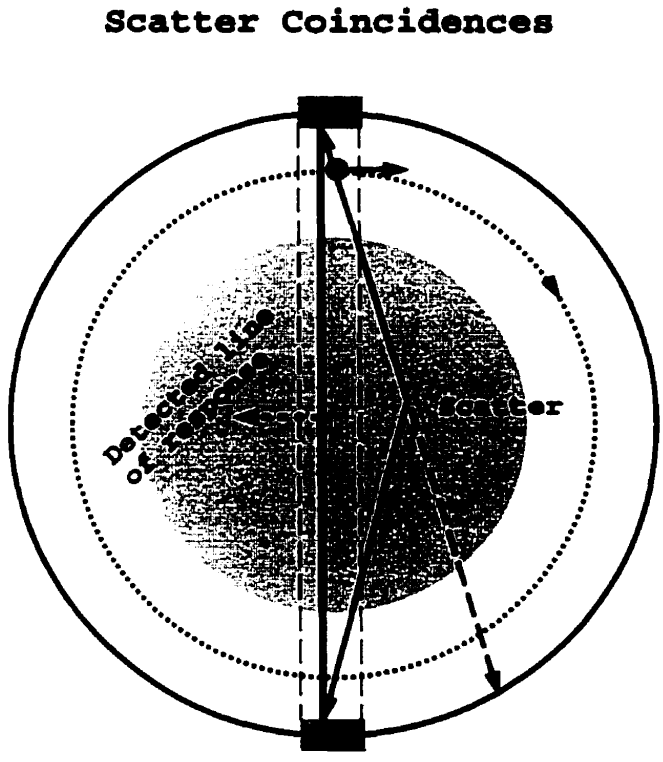

Figure 3.6: A schematic diagram of residual scatter in the transmission scan with a rotating pin source (c.f. Fig. 3.5). One of the paired γ-rays is scattered into the volume between two detectors.

In the absence of any scatter the detected photons travel as a narrow-beam and the measured attenuation coefficient equals the theoretical value. This is represented

by the narrow-beam value μ_n. Because the detector has a finite width some scattered photons can still be detected (Fig. 3.6) and increase I_X particularly toward the object center. I_B can also rise slightly due to some scatter in detectors. Let F_X and F_B be the scatter/true ratios in both transmission and blank data. Equation 3.7 shows that the ACF will decrease by a factor $\delta = (1 + F_X)/(1 + F_B)$ and the wide-beam attenuation value will be underestimated by $ln(\delta)/\mu_n L$. In general $F_B < F_X << 1$. Assuming $F_B = 4$ % and $F_X = 10$ % then $\delta = 5.8$ %. Under this condition μ drops by 2.9 % at L = 20 cm and $\mu_n = 0.096$ cm^{-1}.

Statistical noise can be eliminated by combining the measured and calculated attenuation correction [Xu et al., 1991, Yu and Nahmias, 1996]. These hybrid methods segment short transmission images into different regions and ACFs are computed by assuming a constant attenuation value for each structure. This is highly desirable in body imaging where transmission scans usually have a low count density and the lungs have much lower attenuation than other soft tissue and bone. This approach improves both the accuracy and precision of the emission scan by avoiding noise propagation.

Some PET systems have been modified to acquire the transmission scan shortly after the emission scan [Carson et al., 1988, Hooper et al., 1996]. This is prompted by the need to reduce the long waiting time between both scans and thus the likelihood of patient motion. There is a lengthy (60-90 min) uptake period before FDG/F-Dopa imaging studies can start. While most contamination from emission counts is eliminated by the sinogram windowing the rest is estimated and subtracted from the transmission data before calculating attenuation correction factors. One can decrease the total study time further by collecting both data simultaneously. Activity from each scan is separated based on its unique contribution to the total counts

[Thompson et al., 1991, Meikle et al., 1995]. This type of modifications shortens scan duration and improves throughput in a PET facility.

In the last few years, a new type of method has been explored to perform transmission measurement by using singles data from a point source of radioactivity [deKemp and Nahmias, 1994]. It is motivated by much higher singles rates that will improve counting statistics of transmission data. This approach is potentially important in providing simultaneous attenuation correction in 3-D PET cameras as well as offering a transmission imaging capability for SPECT systems.

3.1.5 Scanner calibration

A PET system is calibrated regularly in order to obtain quantitatively correct values of radioactivity concentration in the image. This procedure is usually performed in two separate steps.

Calibration scan:

This step aims to measure the count rate per 1 μCi/cc activity uniformly dispersed in a 20 cm diameter cylinder with a 20 cm length. A strategy of low count rate and long scan time is used in order to lower randoms and deadtime and achieve high precision in the measurement. This is normally done using a Ge-68 solution at a concentration level of <0.1 μCi/cc. Residual scatter and randoms are subtracted from the raw data to compute the true count-rate in each slice. Tomograph sensitivity is then determined from its ratio to the mean radioactivity concentration measured from a calibrated well counter. Each voxel in the image is scaled by this calibration factor to translate count rates into correct activity concentration. This step is also necessary to correct detection efficiency variation between different slices.

Normalization scan:

Each pair of coincidence detectors has different detection efficiency. This comes from unique properties of each crystal, varying geometrical positions and different gain setting of operational amplifiers in the electronic circuits. It is measured like a blank scan (Fig. 3.5) but with a weaker source to further reduce randoms and deadtime; long scan duration to increase counting statistics. This provides a low scatter source to calibrate both spatial and temporal variations in detection efficiency for each detector pair.

Since the pin source rotates at a constant speed the detector pair at each (radial) projection position receives varying amount of radiation from different exposure. This may introduce some additional variability in the normalization data from the center to the edge. The problem can be corrected by using the orbiting speed and gantry geometry. A better way is to use a uniform slab source rotating around the axis of the tomograph. This source allows simultaneous acquisition of the calibration and normalization data in one single step.

3.1.6 Spatial resolution

One of the key limitations of a PET scanner is the finite 3-D sampling and spatial resolution of the system. This comes from detector size as well as discrete angular and linear sampling. Resolution is characterized by the 3-D point-spread function (PSF) of the imaging system. This refers to both axial and transverse response functions to a small point source. Note that detectors in each ring are actually on a polygon along the circumference as shown in Fig. 2.6. The useful cross-section of crystals and the distances between the coincident detectors decrease as one moves away from the center along the orthogonal direction. Because of the change in solid angles this causes a radial variation in detection efficiency and resolution.

Intrinsic resolution and its spatial variation in the transverse plane are measured with a line source while those in the axial direction are measured with a small, thin disk source across the scanner's imaging field. The source profiles are fit to determine the full width at half maximum (FWHM) at each position. Ideally system resolution should be measured in water to include the positron range of each radioisotope. In practice this is done in air (1 mm tube) and so includes photon non-collinearity effects but not positron range. The latter can be included by performing a convolution of the PSF with that due to positron range. The combined resolution is given by the quadratic sum $w = \sqrt{w_m^2 + w_p^2}$, where w_m and w_p denote the filter width and the positron range respectively. This consideration is particularly important in new scanners with high resolution. Activity concentration in small structures will be in error due to the limited spatial resolution.

3.2 Signal to Noise Properties

The design of PET imaging protocols should achieve maximum accuracy and precision in regional TACs in order to provide the most accurate information about the underlying physiological processes. We have discussed major sources of signal bias in the previous section but ignored noise propagation into the emission data. This section deals with the variance which is affected by every aspect of the study from radiotracer injection to image acquisition and kinetic data analysis.

3.2.1 Projection counting statistics

As in all nuclear medicine imaging we rely on counting γ-rays to estimate the internal radioactivity source distribution. This random process obeys Poisson statistics due to the discrete nature of radioactive decay and the low counting efficiency. At the

raw data level the noise is spatially independent with a variance equal to the total counts at each position: $\sigma^2 = T + S + R$, where T is the true counts. After randoms correction $\sigma^2 = T+S+(k+1)R$, where $k = 1$ if R is removed by a delayed coincidence circuit and $k = 0$ otherwise. Scatter correction introduces only a small variance which can be considered negligible. The S/N ratio in projection data is given by

$$SNR = \frac{T}{\sigma} = \frac{T}{[T + S + (k+1)R]^{\frac{1}{2}}} \tag{3.9}$$

The square of this quantity is defined as the noise effective count rate,

$$NECR = \frac{T^2}{T + S + (k+1)R} \tag{3.10}$$

at each projection position. Note that the NECR is the true count rate which would have the same SNR as we actually see in the presence of S and R. It includes contributions from all physical effects in data acquisition and provides a realistic measure of the count-rate performance of a positron tomograph.

One can obtain the same relationship in the blank and transmission scans. The variance in emission data is increased further by that in the measured attenuation correction factors. Assume that $T_o = T_E T_B / T_N$, it is straightforward to show that

$$\begin{aligned} \sigma^2 &= (\frac{T_B}{T_N})^2\sigma_E^2 + (\frac{T_E}{T_N})^2\sigma_B^2 + (\frac{T_E T_B}{T_N^2})^2\sigma_N^2 \\ &= (\frac{T_E T_B}{T_N})^2(\frac{\sigma_E^2}{T_E^2} + \frac{\sigma_B^2}{T_B^2} + \frac{\sigma_E^2}{T_E^2}) \end{aligned} \tag{3.11}$$

After variable substitution the combined variance and SNR are given by

$$\sigma^2 = T_o^2(\frac{1}{N_E t_E} + \frac{1}{N_T t_T} + \frac{1}{N_B t_B})^{\frac{1}{2}} \tag{3.12}$$

$$SNR = (\frac{1}{N_E t_E} + \frac{1}{N_T t_T} + \frac{1}{N_B t_B})^{-\frac{1}{2}} \tag{3.13}$$

where each pair of variables (i.e. N and t) refer to the NECR and the imaging time for emission, transmission and blank scans respectively. This equation is useful to optimize the total time division between the emission and transmission scans

[Stearns and Wack, 1993]. It can be used as a general figure of merit to guide and improve the system design of a PET instrument.

3.2.2 Image bias and variance

Bias and variance in the regional activity values are determined by the S/N characteristics of image reconstruction methods and the ROI analysis strategy. While the bias is generally unknown in clinical studies it can be estimated from phantom scans. However the variance at each voxel can be predicted from that of the corrected data by FBP

$$Var(g_i) = \sum_{k=1}^{N_p} \sum_{l=1}^{N_r} h_{kl}^2 \sigma_{kl}^2 \tag{3.14}$$

where h_{kl} is the reconstruction filter and σ_{kl} is from the variance equation 3.12. In other words equation 3.14 allows the generation of variance maps for each PET scan. Using the same procedures as described in the previous chapter one can determine regional values from variance images or directly in projection space. Carson et al have derived a formula to estimate ROI variance from clinical images without accessing the raw projection data [Carson et al., 1993]. This information is necessary in order to optimize parameter fitting algorithms.

3.2.3 Partial volume effects

Current commercial scanners have an operational 3-D image resolution ranging from 4-10 mm. This leads to a quantification error referred to as the partial volume effect (PVE). This distortion contains basically two components as illustrated in Fig. 3.7. (a) True activity from small structures is spread over an area larger than the structure itself reducing the apparent activity value. (b) The reduction is partially compensated by activity spillover from adjacent structures. This is particularly true when imaging

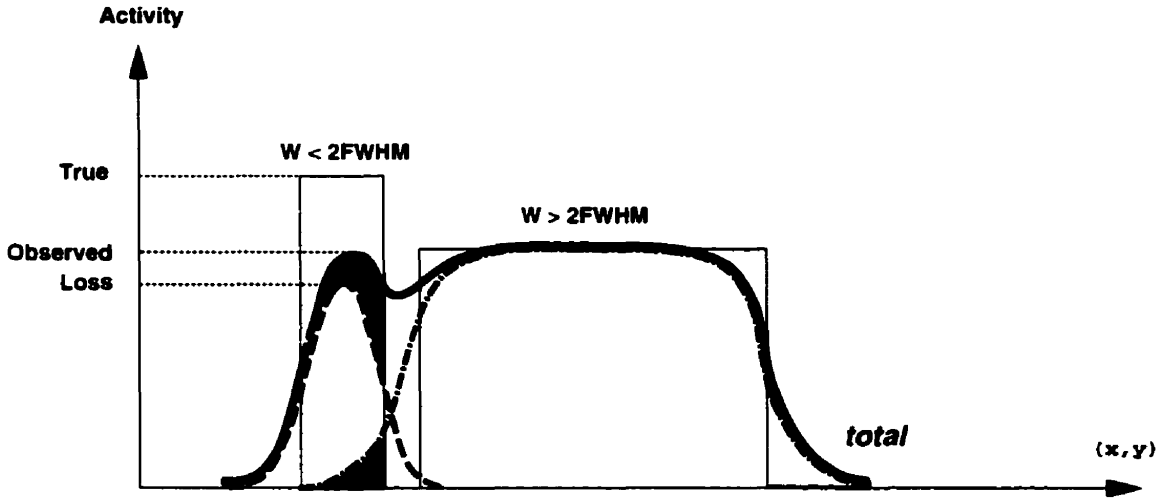

Figure 3.7: A diagram showing the two aspects of the partial volume effect: a loss of radiotracer concentration and activity spillover from its surrounding medium. A structure will suffer more error in the apparent activity as its size (W) becomes smaller than twice the image resolution.

irregular structures smaller than about twice the tomograph resolution in any one dimension. Both the loss of activity from the small volume and the amount of spillover increase with the degrading resolution.

It should be noted that the PVE is a 3-D phenomena limited by both transverse image resolution and axial response (slice thickness). Any structure less than 10 mm cross will be susceptible even when the best resolution of 4-5 mm is used. Many important structures in the brain are smaller than this resolution in at least one dimension. As the resolution becomes worse, activity concentration is progressively underestimated in small structures with high activity but overestimated in those with low activity. Both diminish as the object becomes much larger than 2 × FWHM in all dimensions.

There is no direct way to correct this effect as one would perform in projection data processing. In the absence of background activity the PVE is measured by recovery

coefficient (RC) introduced as the ratio of apparent activity to true concentration in the object [Hoffman et al., 1979]. It has been shown that RC equals 75 % in a 1-D structure of width equal to resolution and a sphere of the same dimension has only 42.2 % of its true concentration. A formula has been derived to calculate this quantity for spherical objects in the absence and presence of background activity spillover [Kessler et al., 1984]. Both vary with 3-D geometrical characteristics of the structures.

PVE can be corrected indirectly knowing the geometry of structure and tomograph resolution. This requires accurate structural information and analytic computation to determine the RC for each structure. However the activity spillover from the background must be estimated and removed from the observed ROI value. Then the true value is equal to the image value divided by RC, with RC a function of the resolution of the PET scanner. In Chapter 7 we will describe a generic methodology for PVE correction in clinical emission scans. Another solution is achieved by using iterative image reconstruction with a realistic 3-D PSF [Carson et al., 1994, Liang, 1994, Mumcuoglu et al., 1996]. This is the most fundamental approach which requires reconstruction of each data frame iteratively. It is not in routine clinical use due to the high computational cost.

It has been known that the measured activity in these areas depends on (1) the volume/shape of the structure, (2) its contrast with the surrounding tissues, (3) its axial position relative to the tomograph planes, (4) 3-D image resolution/sampling, and (5) the shape/size/location of ROI used in data extraction. This is a nonlinear phenomena where each datum on the TAC is a mixture of activity from the structure itself and adjacent tissues having different tracer kinetics. As PET resolution improves this problem remains proportionately in ever smaller structures.

Partial volume effects cause spatially variant image distortions in clinical PET scans [Rousset et al., 1996]. They generally change the shape and amplitude of the observed TACs and lead to systematic bias in parameter estimates with different kinetic models and fitting algorithms. Both are modulated by the anatomical variability of cerebral structures involved in the functional processes. This makes the comparison difficult between subjects and imaging centers, especially when comparing data with varying amounts of atrophy as in the study of brain aging and dementia. Traditionally the problem is reduced somewhat by matching the ages of the subjects between different population groups [Kuwert et al., 1992, Eidelberg et al., 1995]. This is not always possible in any clinical research environment.

Brain activation data are typically reconstructed with large filters to reduce statistical noise and anatomical variability. This leads to much poorer 3-D image resolution and hence a large signal loss and geometrical distortions in many functional areas [Ma et al., 1998]. Consequently current studies focus mainly on the localization of positive and negative peaks of the brain activation foci. Peaks could be localized more accurately at the sinogram level and then mapped into the image space.

Inter-subject averaging improves the SNR but at the cost of a loss in resolution [Cherry et al., 1995]. It is obviously more desirable to conduct activation studies in a single subject. This is made possible by the new 3-D systems which can reduce the number of subjects required to achieve a high degree of statistical significance. Generally randoms affect the S/N ratio much less than attenuation and scatter. The S/N can be improved without correcting randoms and scatter if baseline and activation scans are acquired to have identical total activity. Also the transmission scan and attenuation correction become unnecessary when using the relative CBF change as a benchmark of neural activation.

In clinical observations there is considerable population variability in regional patterns of cerebral radiotracer distribution [Seitz and Roland, 1992, Loessner et al., 1995, Moeller et al., 1996]. Part of the variability comes from the partial volume effects which depend on both object and camera characteristics. In order to determine true biological differences between hemispheres, among subject groups or between diseased and normal brains one must also consider contributions from data acquisition and reconstruction artifacts. This additional variability may prevent us from correctly differentiating normal and abnormal brains.

3.3 Summary

The capability of PET systems for quantitative imaging depends on the accurate correction of many technical factors associated with tomographic data acquisition and reconstruction. In this chapter we have given an overview of the physical mechanisms underlying each distortion and discussed the key software and hardware solutions implemented to correct them. Each of these operations decreases bias but increases variance in the corrected projection data. This makes noise characteristics deviate from the Poisson statistics in the measured coincident data.

We have dealt with the signal/noise issues theoretically by deriving a formula to generate variance maps from the scan data. Besides improving the accuracy of each correction algorithm it is also necessary to minimize noise propagation into emission data. The 3-D partial volume effect is still one of the prevailing limitations in modern PET simply because of the scaling (the smaller structure being imaged with the improvement in resolution). This is especially true in dynamic studies which always require some smoothing operations to reduce noise. In this thesis we have developed a comprehensive simulation environment to investigate these problems.

Chapter 4

Evaluation of PET Imaging Systems

This chapter presents several ways to evaluate the performance of a PET imaging system. It gives a brief survey and review of practical approaches using physical phantom experiments and computer simulations. Although some of the description are based on a Scanditronix PC2048-15B PET scanner the discussion here is generally applicable. We also determine some model parameters to be used in the simulation.

4.1 Experimental Approaches

4.1.1 System description

The PC2048 scanner is a multi-slice brain tomograph with the same design features as the PC4096-15WB body system (General Electric Medical Systems, Milwaukee). The ring diameter and the number of detectors are decreased by half which doubles the true count efficiency while reducing the cost. Both acquire 15 images simultaneously with an inter-slice separation of 6.5 mm and a relatively uniform 3-D intrinsic resolution of 5-6 mm across the central portion of the field of view.

Table 4.1: Geometrical parameters of the PC-2048 PET scanner

Scintilator type	BGO	Ring separation	1.0 mm
Number of rings	8	Ring diameter	50.5 cm
Detectors per ring	256	Septal length	9 cm
Crystal size (mm^3)	6 × 12 × 30	Diameter of FOV	27 cm
Crystal separation	0.2 mm	Transmission source	Ge-68 rod
Packing fraction	92 %	Orbiting diameter	30 cm
Septal thickness	3 mm	Rotation speed	20 rpm
Slice separation	6.5 mm	Tilt angle	± 20°

Table 4.1 describes the physical geometrical configuration (c.f. Fig. 2.5). There are 8 rings in the gantry each with 256 bismuth germanate (BGO) detectors. They have a 50.5 cm diameter and cover an axial height of 10 cm. BGOs are arranged in blocks of 4 × 4 crystals each with a 6 mm width, 12 mm height and 30 mm depth. Five faces of each crystal are painted with light reflective materials and the set of 16 crystals is glued together before being linked to two Hamamatsu R1548 dual cathode photomultiplier tubes (PMTs). The packing fraction is 92 % with a 0.2 mm separation between crystals. Adjacent blocks are insulated by a tapered lead wedge 1 mm thick at the outer end. Thus the detectors form a 64-sided polygon along the perimeter of the ring. Inter-ring lead septa (3 mm thick by 9 cm long) define a 32 cm inner diameter with a patient port diameter of 27 cm.

A tilting mechanism of the gantry with respect to the horizontal axis, coupled with bed translation allows data acquisition at many patient orientations and cross sectional levels (Fig. 4.1). The gantry can perform a wobble motion of 6 mm diameter with 5 bins per stationary member position separated at 1.24 mm. Wobble speed is adjustable between 5-20 rotation per minute (rpm) with an minimum wobble time of 1 second. A laser beam in the form of a cross is mounted with a known position

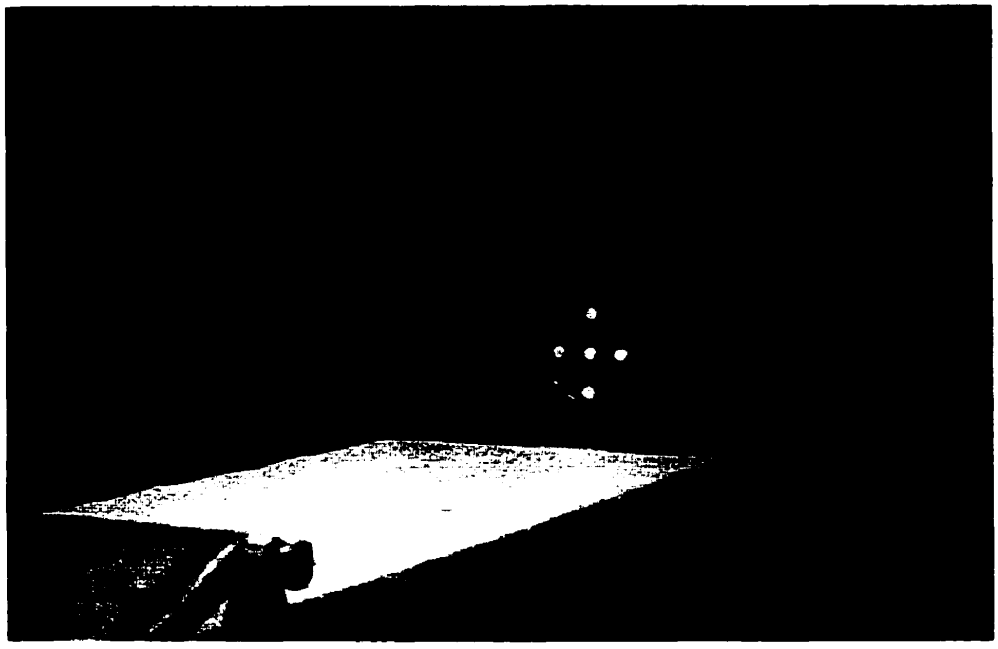

Figure 4.1: Setup of the scanner with the phantom inside the gantry. This photo shows the control panel, laser port, patient couch and head rest.

relative to the center of the lowest slice.

This scanner is hosted by a MicroVax computer under the VMS operating system. Data acquisition and reconstruction programs are driven by a set of parameter files which describe the physical conditions of the tomograph as well as relevant information of the imaging protocols. While some files contain permanent constants many others store variables supplied or measured prior to any study session. Both programs and data structures work on all scanners from the same manufacturer. It maintains extensive databases so that any data acquired in the past can be correctly reconstructed retrospectively.

Each detector is in coincidence with 48 detectors on the opposite side of the ring with a 20 ns coincidence time window and 300-650 keV energy levels. Cross slices are formed from the sum of the lines of response between two adjacent rings. Coincidence data in each plane are subsequently sorted into 256 angles. In stationary mode

each angular projection contains 48 non-uniformly distributed members separated by 6.6 mm at the center to 5.6 mm at the edge of the imaging field. Before image reconstruction the contributions from other physical effects are removed to estimate the true coincidence rates.

$$T_k = [(P_k - R_k)/N_k - S_k]/(A_k D_k C_k) \tag{4.1}$$

where P_k is the measured raw projection, R_k the randoms, N_k the normalization data, S_k the scatter, A_k the attenuation factor and D_k the deadtime factor. C_k is a constant to compensate the effect of scan duration and radioactive decay for each frame. The decay correction is relative to the mean time rather than the midtime assuming that the tracer concentration is constant within the frame.

After randoms subtraction and efficiency normalization the odd/even numbered projection data are interleaved in order to increase the radial sampling. This gives 128 angles × 96 parallel rays with a 3.2 mm average separation. Each angular profile is then interpolated into 128 elements equally spaced at 2 mm. Scatter counts are then removed from the measured data with a deconvolution filter. A standard FBP algorithm is implemented with commonly used reconstruction filters. Images contain 128 × 128 × 2 or 256 × 256 × 1 mm^2 pixels. A set of scan-related variables are stored in the image header from which one can extract many useful parameters for each slice and for each dynamic frame.

Transmission scans are done with a 5 mCi Ge-68 pin rotating at 20 rpm around a 30 cm diameter orbit. Data processing follows equation 4.1. However scatter and randoms in blank and transmission data are assumed to be small and not corrected by the reconstruction program. Nor does it perform detection efficiency normalization since attenuation correction factors depend only on their ratios. Transmission images are then reconstructed by FBP to obtain the attenuation value in cm^{-1}. Attenuation

correction can also be done by the use of computational algorithms based on image segmentation and known tissue attenuation values.

4.1.2 Performance parameters

In practice the quantitative performance of a PET camera must be evaluated in order to optimize its clinical usage and ensure adequate image quality. This follows a set of standard procedures as described in great detail by many authors [Evans et al., 1991b, Spinks et al., 1992, DeGrado et al., 1994, Adam et al., 1997]. In this section we summarize several basic measurements which are necessary for routine quality control of a PET scanner as well as providing the figures of merit for system performance. We show some data from the PC2048 brain scanner and describe how to derive model parameters for each physical factor.

Volumetric Resolution:

Axial resolution was measured in air by passing a series of small disk sources (Ga-68 solution) through the axis of the scanner. Images were reconstructed with decay correction to obtain activity values of each disk as a function of axial source position. Each profile in the axial direction was interpolated to determine the effective thickness of each slice at different radial positions.

Transverse resolution was determined by performing line source scans with stainless steel tubes (1 mm I.D.) filled with Ga-68 solution and placed at several locations in a 20 cm cylinder. Fig. 4.2 plots the measured 3-D resolution and the fitted curves at different spatial locations. It shows a relatively small variation in both axial and transverse intrinsic resolution. Over the central 20 cm of the imaging field, the in-plane resolution is 6-7 mm FWHM whereas the axial resolution is between 5-7 mm FWHM.

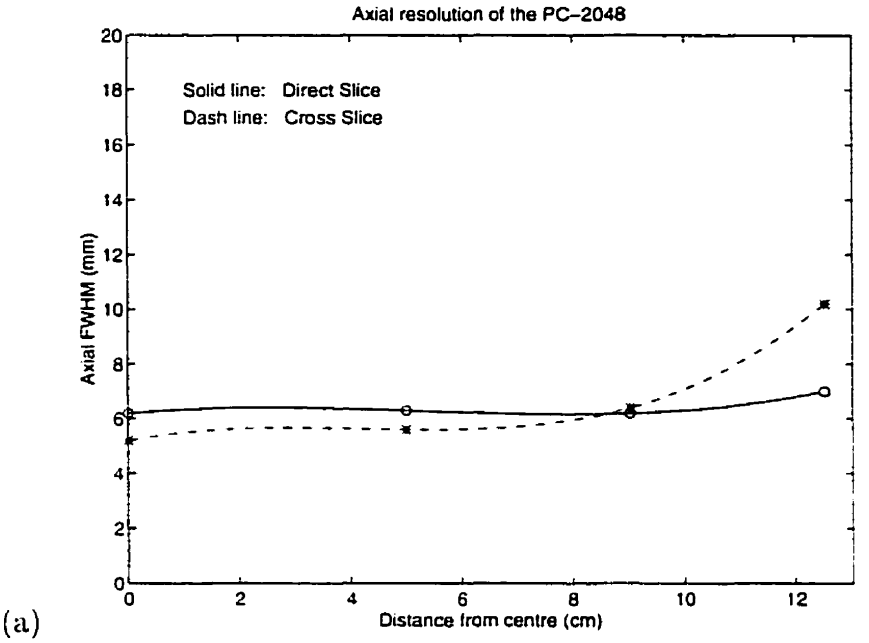

(a)

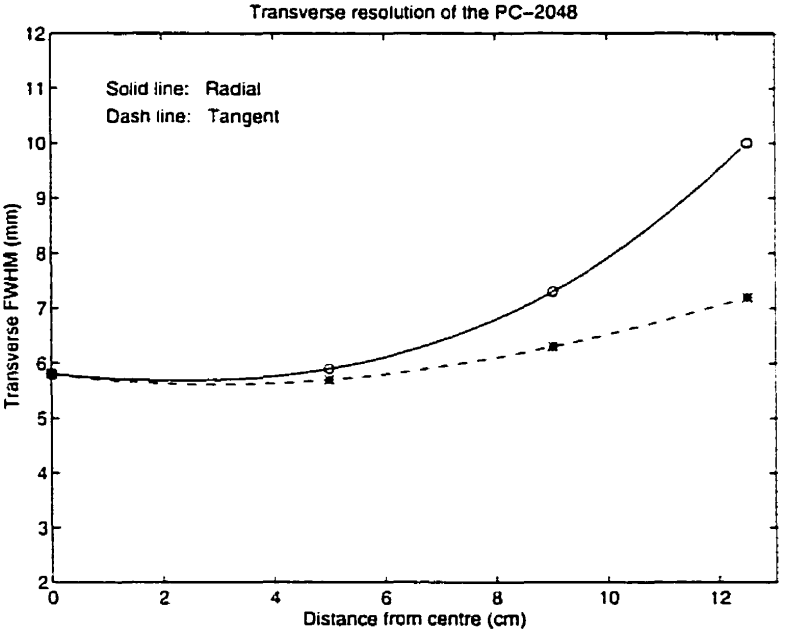

(b)

Figure 4.2: Spatial variation of the measured axial (a) and transverse (b) resolution of the PC2048 scanner along with the fitted curves.

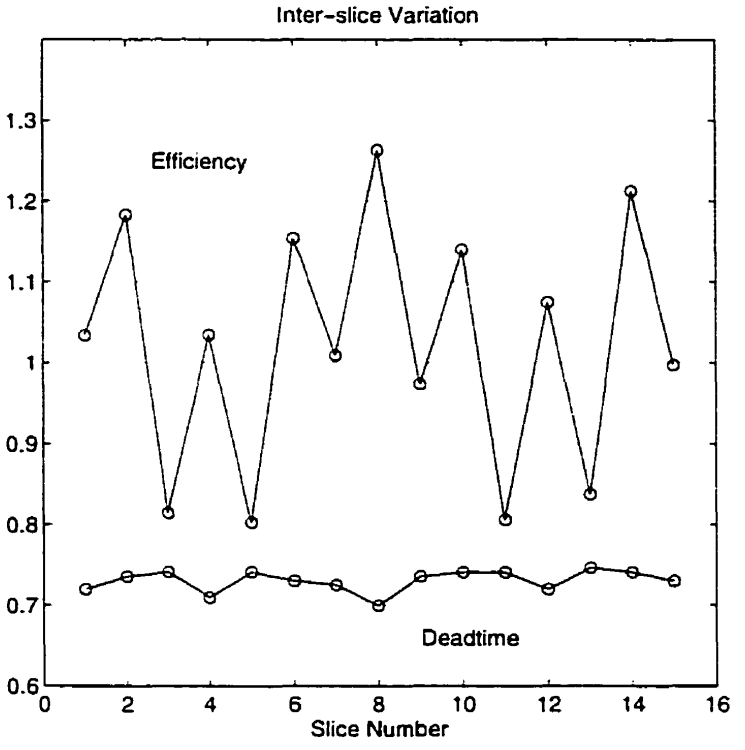

Figure 4.3: Slice-specific detector efficiency in the current system and deadtime factor (relative unit) of the uniform phantom. The efficiency is normalized to the mean value over 15 image planes of 10.7 Kcps/μCi/cc.

System calibration:

The PET camera is calibrated and normalized regularly using a flood phantom and a transmission pin respectively. To ensure negligible randoms and deadtime both are performed at low activity over a long scan time. Fig. 4.3 shows that the detector efficiency in each slice varies by 57.4 %. The mean sensitivity is 9.7 Kcps/μCi/cc in the direct image planes and 11.7 Kcps/μCi/cc in the cross image planes. We observe a high level of modulation reflecting the overall detector properties of individual slices. This pattern arises mainly from gain differences of the discriminator circuits (one per detector ring). This gain is very sensitive to temperature fluctuations on the electronics rack and is therefore measured daily on some systems.

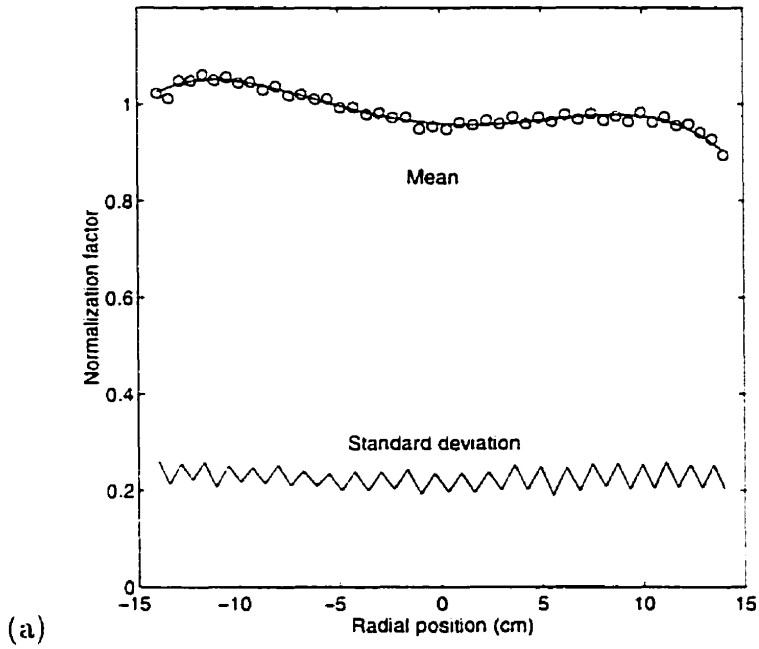

(a)

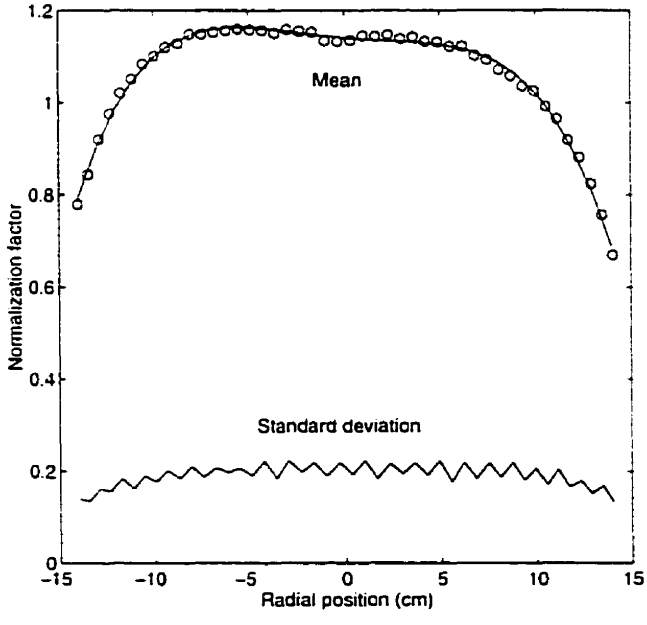

(b)

Figure 4.4: Radial variation of the measured in-plane detection efficiency and the fitted curves in the direct (a) and cross (b) slices.

A typical normalization file was averaged over all angles to obtain the mean and standard deviation profiles in each slice. The mean values were then fitted to polynomials in order to characterize their variation at different radial positions. As Fig. 4.4 shows the cross-plane efficiency increases on average by 50 % from the edge to the center while the direct-plane efficiency remains almost constant. The fitted curves have mean errors of less than 1 % on all slices. This data is more stable over time and is measured less frequently than the slice sensitivity.

Count-rate capability:

This was determined by scanning a 20 cm diameter flood phantom filled with F-18 solution. Components of the total counts in each slice were extracted to generate separate count-rate curves as a function of activity concentration in the cylinder. It is known that the true plus scatter $(T + S)$ and randoms (R) curves fit well with a linear and quadratic functions respectively at the low activity range. Fig. 4.5 plots these data together to demonstrate substantial and nonlinear decreases in $(T+S)$ and R rates caused by deadtime. The deadtime factors related with these two quantities can be estimated by a comparison between the extrapolated and measured data at higher activity values. This offers a useful way to derive numerical models to correct deadtime effects at arbitrary activity levels.

Note that the data measured at count-rates of 12.5 Kcps show a change of 6.7 % in deadtime factor (D_F) over slices (Fig. 4.3). This is much smaller than that in the slice-specific efficiency since deadtime depends mostly on characteristics of detector blocks which cover several slices. To describe the true count-rate response of the system we need the $(T + S)$ rates free from deadtime. The true count-rates were computed with deadtime correction using information in the image header file. The random fraction $R_F = R/(T + S)$ was calculated. In order to derive a theoretical

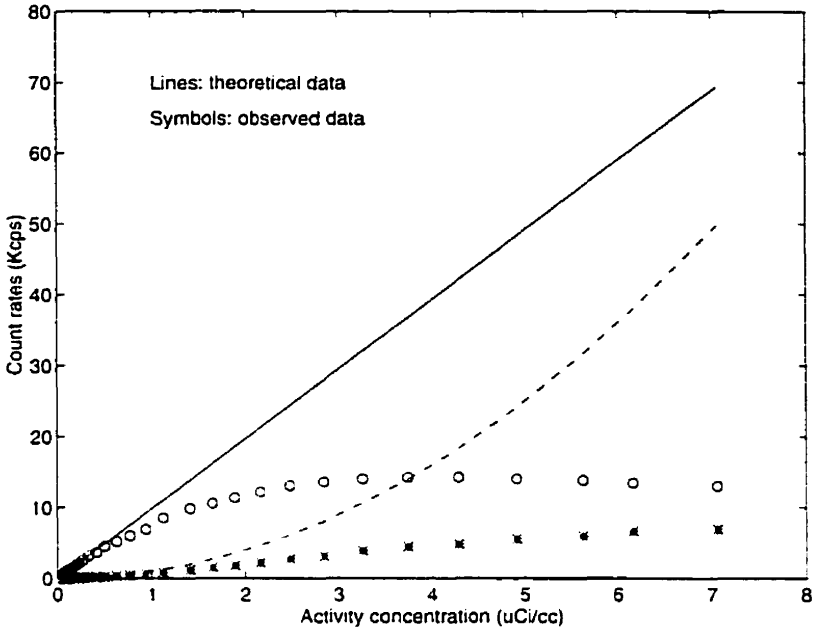

Figure 4.5: Measured true+scatter rates (o) and random rates (*) from a uniform phantom. Solid and dash lines represent the expected data of each component in the absence of deadtime.

model for deadtime we fitted the D_F vs $(T+S)$ curves to polynomials as seen in Fig. 4.6. A randoms model was also derived by analyzing the R_F vs $(T+S)$ data in the same manner. Both have good fits with the mean percentage errors of 1 % and 4 % respectively. Note that D_F drops to 0.42 and R_F rises to 32.5 % at high count-rates of 40 Kcps.

This simple experiment also allows the computation of the noise effective count rate (NECR) using equation 3.10. Fig. 4.7 plots the true and NECR rates vs activity concentrations. Following the initial rise both reach a peak and begin a slow decline at high activity levels. The gain in the signal/noise ratio will disappear if the injected dose in the subject is sufficiently high. This is the basis for the selection of the tracer delivery strategy according to the type of study and the count-rate behavior of the tomograph. Radioactivity below the saturation point is used for optimal dosimetry.

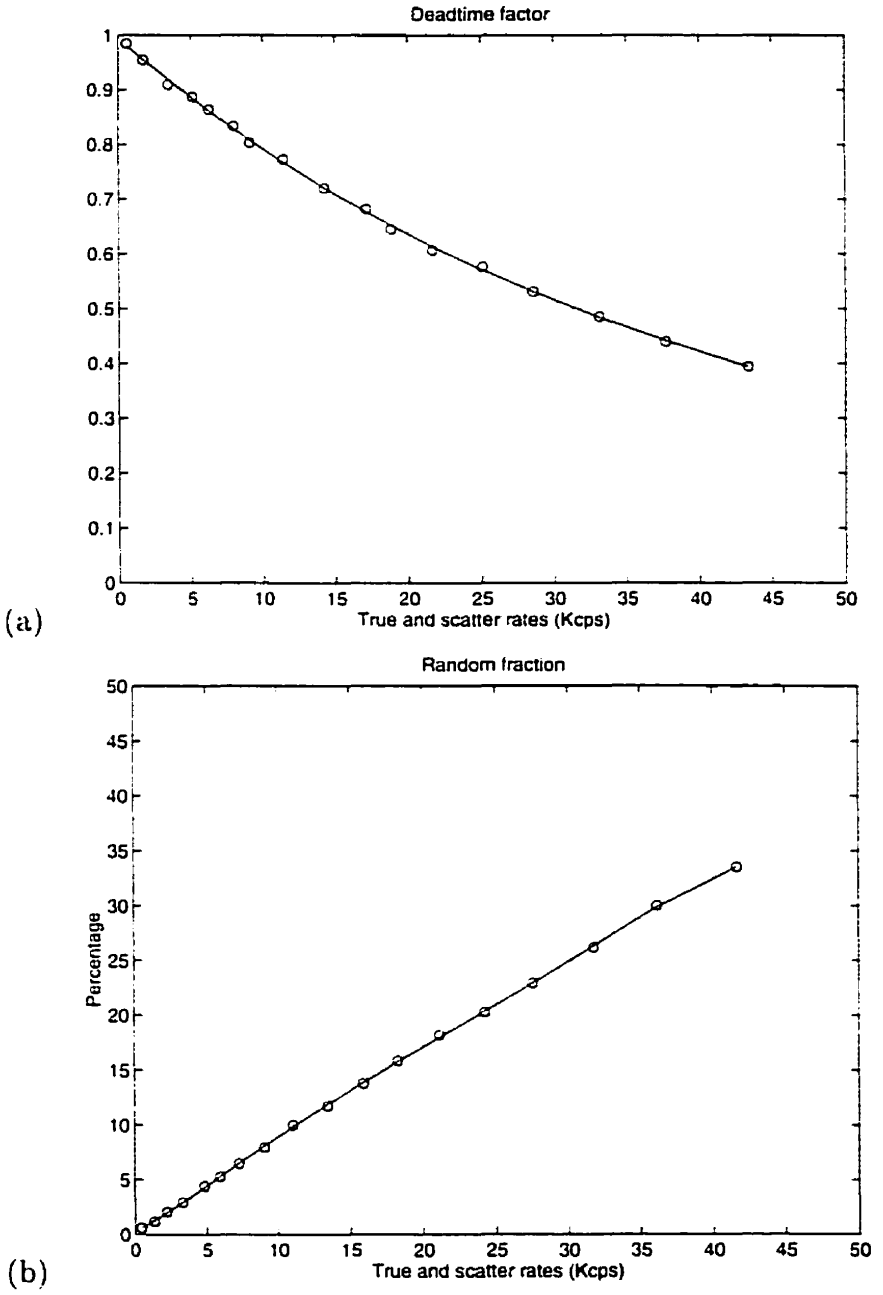

Figure 4.6: Deadtime factor (a) and random fraction (b) measured from a uniform phantom. Data are plotted against total coincidence rates with the solid lines representing the fitted curves.

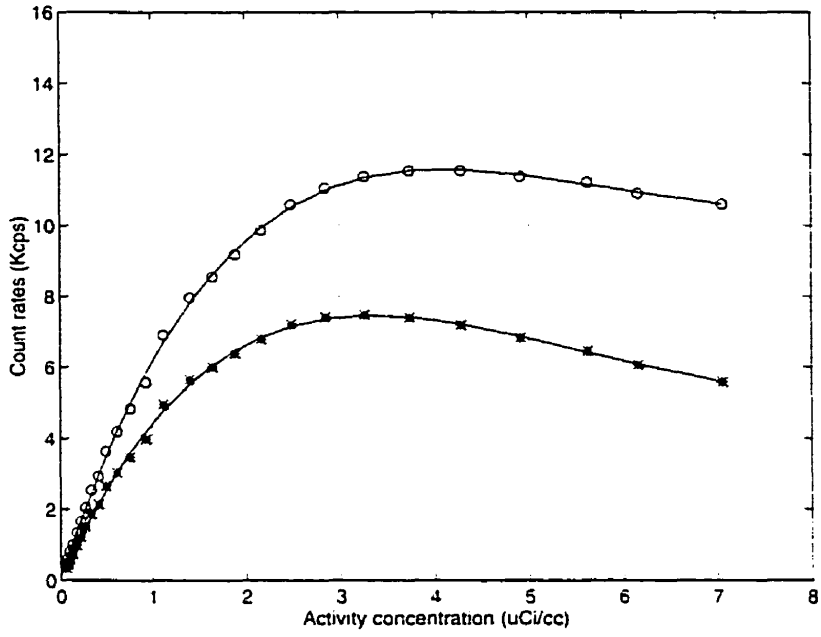

Figure 4.7: Measured true rates (o) and noise effective count rates (*) from a uniform phantom showing saturation at higher activity values.

Data given above fully describe the position dependence of the 3-D detector resolution and efficiency as well as the non-linearity of the PET system from randoms and deadtime effects. These features have been parameterized by using polynomial curve-fitting. This type of analysis can be replicated in both 2-D and 3-D configurations of several new generation commercial PET systems.

4.1.3 Phantom and human studies

The experiments described in the previous section only document the behavior of key physical factors in projection data. The effects of these components on image quantification should be evaluated in each type of study for accurate recovery of functional information from PET scans. In practice this is done using physical phantoms filled with known amounts of radioactive solution to provide uniform and

distributed activity sources. This is advantageous since the measured activity values on PET images can be compared directly with those measured from a calibrated well counter. However most studies use simple geometrical phantoms to represent 3-D activity distributions in brain scans [Adam et al., 1997. Sossi et al., 1998b]. For instance, small objects such as hot/cold spheres are commonly inserted in cylinders to test scatter correction methods. Data are acquired with a low activity to minimize compounding effects from deadtime and randoms. The overall imaging accuracy in the presence of these physical factors is best characterized by using two isotopes with short and long half-lives to provide large changes in image contrast and count rates [Cooke and Evans, 1983]. Small objects with dimensions comparable to the image resolution are often used to assess activity recovery from limited tomography resolution. This is often insufficient to reveal object dependent imaging distortions in dynamic PET scans.

Physical phantoms made from anatomical boundaries of the brain have also been used to evaluate PET imaging characteristics specific to neuroanatomy. The 3-D Hoffman brain phantom [Hoffman et al., 1991] is made of lucite plates of varying thickness created from regional contours on MR scans of a normal human brain. It provides a true contrast of 4:1 between gray matter and white matter structures as seen in cerebral blood flow and metabolic PET images. This anthropomorphic phantom has proved useful in assessing the impact of scatter and deadtime corrections on the accuracy of regional activity values.

The problems of signal/noise ratios (SNR) in activation imaging studies have been investigated by scanning a 3-D Hoffman brain phantom with small radioactivity inserts [Votaw, 1996]. This is conducted under varying conditions of signal size and intensity as well as different image resolution and noise in the acquired data. It

confirms that there are slight gains in SNR without performings random and scatter corrections. While useful for testing camera response to particular imaging conditions this approach is not applicable in more general situations.

Several authors have studied partial volume effects extensively with 3-D brain phantoms. For example, recovery coefficients have been measured from a unilateral basal ganglia (BG) brain model as a function of image contrast and axial positioning in the gantry [Bendriem et al., 1991]. This single BG structure is used to estimate quantification errors in a dual isotope experiment simulating the activity distribution encountered in neuroligand studies. Using the Hoffman phantom we have observed large variability in the measured regional values in both cortical and subcortical gray matter structures [Ma and Evans, 1996]. This depends significantly on the reconstruction filter parameters and on the size and shape of regional templates. These phantoms can provide different contrast/noise and count-rate situations, but not a realistic dynamic tracer distribution reflecting the nature of human anatomy and physiology.

The third type of methods evaluate PET cameras with real human brain scans. Since the radiotracer distribution is unknown with human studies this only allows relative comparisons of data acquisition and processing protocols which may have already been validated with phantom studies. It has been shown that correlation patterns between regional glucose metabolic rates depend strongly on resolution when scanning the same subjects on two different tomographs [Grady, 1991]. Although the regional rates between the two scanners have no simple relationship the ratios of lobar to global gray matter metabolism show significant correlation. A recent brain study has compared 3-D and 2-D scanning protocols on the same scanner using data from F-18 glucose metabolism and two C-11 radioligands involved in the action of dopamine

receptors [Sossi et al., 1998a]. No significant difference has been found between the two methods with the same level of counting statistics. This is not surprising since both modes have similar image resolutions. However the 3-D mode does allow the injection of a much lower activity than the 2-D mode.

4.2 Computer Simulation Approaches

Computer simulations have long been a powerful tool for modeling data acquisition and image reconstruction processes of tomographic imaging systems. This approach offers several key advantages: (1) physical degrading factors that normally contribute simultaneously in an imaging experiment can be separately included; (2) their effects on imaging quantification can be individually estimated under realistic conditions. There exist two broad methods based on either Monte Carlo or analytical modeling. Both have been used to improve camera design and optimize data analysis algorithms in clinical PET studies. In this section we review the previous methodology and introduce our simulation approach.

4.2.1 Monte Carlo simulations

Monte Carlo simulation (MCS) is the fundamental approach for examining the physical performance of a positron tomograph [Lupton and Keller, 1983]. It works by tracking γ-ray transport from emission at positron sources to their detection in the crystals. Photon energy, position and direction after each scatter interaction are recorded and analyzed until the photon is either absorbed or escapes from the detection system. Physical effects related to positron range and photon non-collinearity can be included in the calculation. This method provides energy spectra for both single and coincidence radiation. One can then apply coincidence condition, energy

differentiation and appropriate deadtime behavior between each pair of detectors. Besides singles and total coincidence rates it can give data components of true, scatter and randoms in each projection.

The key advantage of this approach is that computations for source distribution, collimation, detection geometry and electronics can all be done independently in a cascade process [Thompson et al., 1992]. This allows one to compare different combinations of design parameters and scintillator materials using the same prior history files. As in the experimental approach this method employs geometrical phantoms along with point and line sources. There have been extensive investigations to evaluate the count-rate capability of several commercial scanners with and without septa [Moses et al., 1997]. This gives important information on overall sensitivity and NECR at different activity levels. MCS is best suited to study scatter and attenuation problems in emission and transmission scans. It provides objective means for comparing the accuracy of scatter correction algorithms.

Another important application is the prediction of 3-D detector response functions. This is used to correct the photon penetration effect among PET detectors and estimate the detection probability in iterative image reconstruction [Huesman et al., 1989, Llacer et al., 1993]. Other workers computed spatially variant 3-D resolutions in great detail and compared them with the measured values from two PET scanners [Michel et al., 1991]. By such a comparison they also estimated contributions from multi-crystal encoding to both axial and transverse resolution components. This type of calculation is especially valuable for determining physically realistic locations of photon interaction in each pair of coincident detectors. The effective detector positions from the MCS have been used in data interpolation of the PC2048 scanner [Picard and Thompson, 1994]. The use of these parameters improves resolution and

removes small geometrical distortions in image reconstruction.

However this approach is limited in practical applications by the enormous computation and data storage requirements. With these constraints it is often difficult to generate a sufficient number of counts for adequate precision in the simulation. Simulated projection data are generally too noisy to perform any meaningful reconstruction. Many efforts have been made to improve the accuracy and precision of MCS. This involves mostly recycling some photon history files and variance reduction with fast computers. Despite moderate progress most studies still rely on simple geometrical objects to represent activity and attenuation distribution in the human body [Wang et al., 1992]. One can employ anatomy-based models only in organs with relatively simple shapes. This has been demonstrated in the simulation of gamma camera data with a human phantom [Zubal and Harrel, 1991]. Because of the weak dependence of scatter radiation on radiotracer uptake patterns these methods have also been implemented to estimate and remove scatter coincidences in clinical scans. However the computation cost is prohibitive for modeling data acquisition with any realistic phantoms.

To have some speed advantage over the MCS several analytical formulae have been derived in both multi-slice and volumetric configurations [Tanaka et al., 1982, Maze and Lecomte, 1990]. They calculate theoretical count-rates from geometrical phantoms using rigorous numerical integrations. This is a simplification generating reasonable agreement with the experimental data. Recently others have improved and validated this alternative method on two PET scanners in 3-D mode [Moisan et al., 1997]. In particular they have predicted big gains in NECR when using lutetium oxyorthosilicate crystals within practical constrains in camera design. However this approach has the same objective and limitations as the MCS. Both of

them could not evaluate the effects of physical factors in the image space, nor do they reveal additional distortions from image reconstruction.

4.2.2 Analytical simulations

Analytical modeling is the more practical approach for characterizing the behavior of a PET imaging system. This is desirable not only to counter the limitation of the MCS but also to evaluate data processing and image reconstruction algorithms. In particular it allows repeat simulations of dynamic PET scans rapidly from 3-D radiotracer distribution information. The basic methodology is to incorporate the dominant characteristics of any tomograph imaging system into efficient computational models. This has been done in both image space and projection space.

Before discussing more rigorous methods we briefly mention a very simple simulation widely used to compare kinetic data analysis algorithms. It is normally done by adding varying amount of Gaussian/Poisson noise to theoretical time activity curves (TAC). As discussed in section 3.2 this approximation is inadequate and does not reflect study-specific bias and variance. A more realistic noise model has been derived by considering scan intervals in order to optimize temporal sampling of data acquisition [Jovkar et al., 1989]. The variance of the TAC is assumed to be proportional to its integral in each interval with the proportionality constant determined by matching the predicted noise level to that observed in real data. This empirical approach has been employed to evaluate many aspects of dynamic PET imaging protocols [Feng et al., 1995]. Its most common use is to examine the interaction between model parameters with different estimation techniques. In a noted example other workers have investigated the effects of tissue heterogeneity by mixing distinct kinetic curves with different fractions [Blomqvist et al., 1995]. Although many esti-

mation algorithms work well with simulated data their good performance often deteriorates with real data because of the presence of the potential distortions described above.

Image-based simulations rely on the assumption that the observed image is a convolution of the true activity distribution with the 3-D PSF of the scanner. This holds true only if all other physical distortions are properly corrected. The effect of counting statistics is modeled by adding random noise to each image voxel before or after the convolution operation. Its use would require accurate mapping of the image PSF corresponding to each reconstruction filter. This is not a trivial task considering large variations of filter types and sizes used in clinical data. Additional difficulty arises from the modeling of the PSF which becomes increasingly anisotropic away from the center as shown earlier. Although potentially allowing quantitative restoration of image bias this approach does not provide much information on variance which is difficult to predict in the image space.

This method is most useful in the study of image resolution problems. For example it was employed to estimate the effect of activity spillover from the background [Kessler et al., 1984] and that of axial sampling and slice thickness [Miller et al., 1990]. Both depended on integrations of uniform spheres and rectangles with 3-D and 1-D Gaussian functions respectively. More complex phantoms could be created using anatomical images and tissue biodistribution data. This simulation was a useful tool to evaluate errors in MRI-PET image registration algorithms [Andersson et al., 1995]. Its most valuable application is the correction of 3-D partial volume effects in both brain and cardiac scans as will be discussed in more detail later in Chapter 7. However most groups use a 3-D PSF uniform in each direction. In addition this approach can not model other physical factors underlying sinogram data acquisition and recon-

struction.

Projection-based simulations can overcome these limitations. We require some basic knowledge of the scanner at the sinogram level which needs to be measured only once as part of quality assurance of every PET camera. General methods have been demonstrated in the simulation of a CT scanner [Herman, 1980]. Sinogram data are generated with all physical effects and Poisson statistics as in tomographic measurement. One can then explore signal detection and noise propagation issues through data correction and image reconstruction chains. Most early work depends on geometry-based objects since their projection data are known exactly. This has been used to validate many iterative deconvolution algorithms in both emission and transmission tomography.

Since the 1980s simulations using anatomically realistic phantoms have become a popular approach to study accuracy and precision in quantitative PET imaging. Several early studies employed a digital brain phantom created from one tissue slice of a human brain cadaver [Mahoney et al., 1987]. Anatomical contours were drawn around gray matter, white matter and CSF structures which were then assigned relative activity concentrations. A 2-D simulation was implemented to verify some design parameters of a body tomograph and SNR gains with smaller detectors [Phelps et al., 1982]. This was also valuable for documenting the in-plane partial volume effects in many neuroanatomical structures and nonlinearity problems in parameter estimation algorithms [Huang et al., 1987]. However the 2- D approach is clearly limited to study the axial sampling and resolution problems inherent in a PET scanner.

While considering only the detector resolution and filtering during image reconstruction this early work did not include attenuation and scatter in the object. The

omission of these effects would underestimate the noise levels in the simulated projection. It has been shown that the magnitude of noise could be 10-100 times smaller than that seen in typical PET scan data [Rowe and Dai, 1992]. By analyzing the observed relationship between the noise power spectra and total projection counts they have derived an empirical noise model from both brain and body scans. Although this model can add the right amount of noise in such situations it is applicable only to the particular radiotracer system and PET camera in question.

Subsequently 3-D simulations have been developed in several imaging centers. For instance some investigators have evaluated the localization accuracy in PET activation scans by inserting small objects in the 2-D brain phantom [Mintun et al., 1989]. While including photon attenuation from brain tissues they omitted contributions of the skull bone and the noise from attenuation correction. In addition scatter and randoms were ignored along with spatial variations in the detector positions and sensitivity.

A better algorithm has been implemented by considering the detector geometry and efficiency along with some limitations of coincidence detection [Hutchins, 1991]. The author also initiated a procedure to generate a 3-D brain phantom from segmented MR images and simulated tracer kinetic data. This was then used to investigate the effect of image resolution on signal loss and contrast recovery in the rate constants of neuroreceptor binding studies. Simulations of a heart phantom were also applied to compare the influences of ROI placement on the bias and variance in kinetic model parameters [Hutchins et al., 1992]. The results provided a valuable guide for selecting the optimal analysis strategy that gives minimal errors in human myocardial scans. However this method disregards attenuation effects while adding noise in the image space.

Most studies incorporate only uniform sampling and use a stationary PSF to model resolution but ignore their spatial variability throughout the field of view. They do not properly include the nonlinear components related to randoms and deadtime. Nor did they consider image distortions associated with attenuation correction. Simulated noise characteristics in both projection and image space differ from reality particularly with the increased tomograph resolution. Consequently they provide only a relative evaluation of the S/N problems in regional functional data.

In many imaging centers MR data have been routinely collected and registered to PET images for regional correlative analysis [Pelizzari et al., 1989, Evans et al., 1992b, Woods et al., 1993]. With automated image segmentation and tracer kinetics data one can create a customized 3-D object model to represent regional activity concentration and attenuation maps in each subject. Since 1992 we have introduced a complete simulation system based on the measured physical and statistical characteristics of a PET scanner. In a preliminary report [Ma et al., 1993] we have described its basic structures and initial validation with a geometrical phantom.

Over the last several years our sinogram modeling and image reconstruction programs have undertaken numerous expansions and revisions [Ma and Evans, 1997]. We have incorporated key features involved in PET imaging methodology and performed rigorous validation before applying them to clinical problems. Many useful options have been added to accommodate increasingly realistic clinical situations and support some collaborative projects.

4.3 Summary

In this chapter we have examined several methods commonly used to evaluate the performance of a PET imaging system. While phantom studies offer the most objective

assessment of imaging accuracy and precision they suffer from an unrealistic representation of the radioactivity distribution and an inflexibility in experimental conditions. Human studies permit relative evaluation and clinical verification of many imaging procedures and computational algorithms established through phantom scans. Although playing a very important role in evaluating the limited capability of PET systems both are insufficient because of the interplay between individual physical components of the tomograph.

Computer simulation is a viable alternative which can overcome these limitations. However it must combine anatomically correct radiotracer distribution data with a sinogram model that recognizes each physical distortion source inherent in coincidence detection. In principle PET cameras are sufficiently characterized by a set of design and performance parameters. This information is available from phantom scans or Monte Carlo simulations and can be incorporated into simulation models as described in the next chapter.

Chapter 5

Simulation Methods and Implementations

The core of this project is the analytical modeling of the PET data acquisition and image reconstruction process with realistic tracer biodistribution among cerebral structures. This chapter describes the design and implementation of the 3-D simulation system (PETSIM) in detail. Fig. 5.1 is a flow chart that highlights its principal constituents. The intention was to simulate dynamic PET imaging studies by combining the spatially correlated MRI data with tracer kinetic models. This process was made more efficient by providing a set of object and scanner specific parameter files.

Although the simulation approach is general to any PET imaging systems this work will concentrate on key physical and statistical factors of a multi-slice scanner. The following sections cover these matters and show some typical image data. Section 1 discusses procedures used to create 3-D brain phantoms representing tissue activity concentration and attenuation coefficient in the human body. Section 2 presents simulation algorithms of projection data to include the measured 3-D detector response functions and count-rate characteristics described in Chapter 4. Section 3 summarizes the basic components and usage of the PETSIM program along with its file

structures. A short discussion is also given on image reconstruction algorithms and some computational issues.

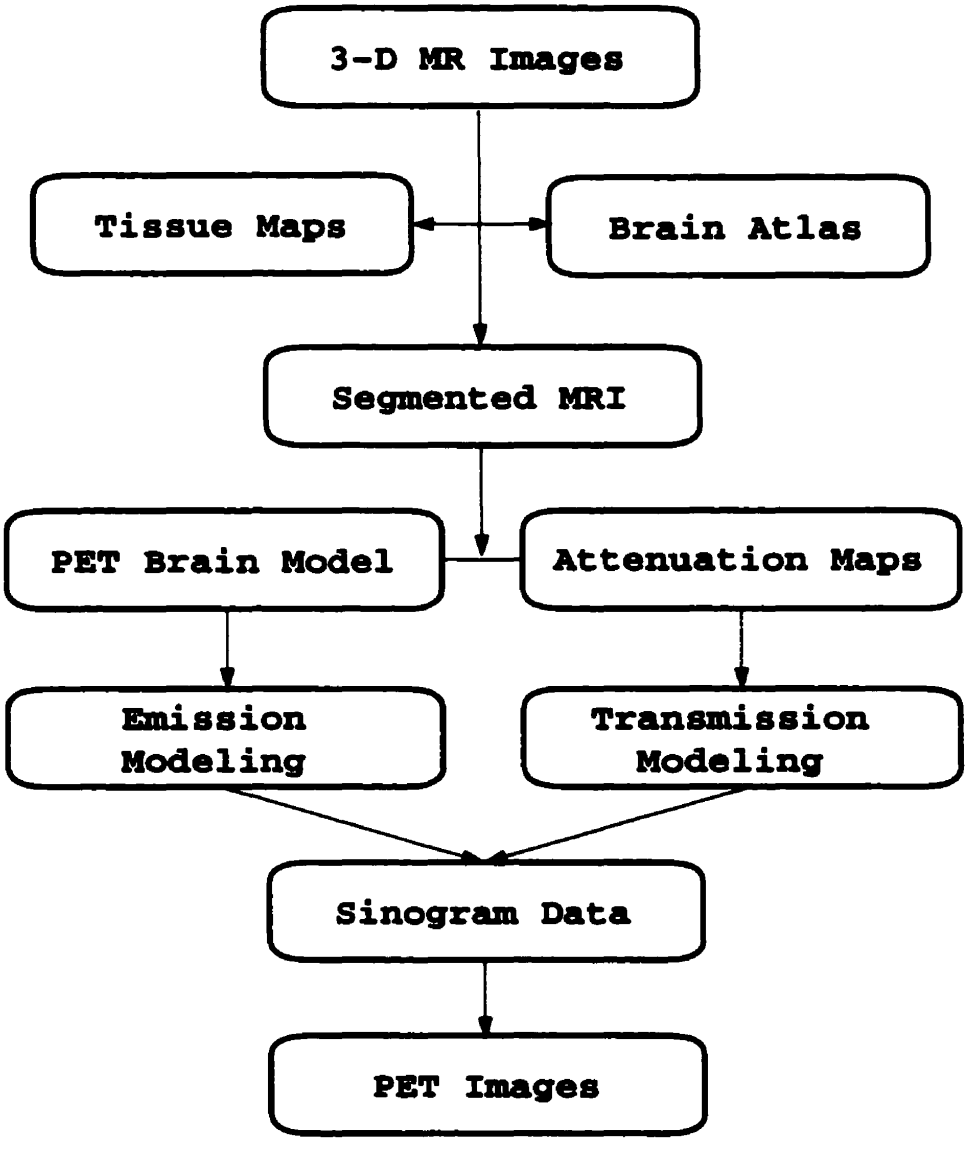

Figure 5.1: A computational block diagram of PETSIM system. It is designed to generate simulated emission and transmission PET images from segmented MRI data.

5.1 Computerized 3-D Brain Phantom

5.1.1 Acquisition of MRI data

In MR imaging the body section is placed in a strong magnetic field and stimulated intermittently by radio-frequency pulses. Protons in water have an intrinsic resonance frequency proportional to the field strength. After absorbing this external radiation they will reach a higher energy level and then emit radio-waves within a few hundreds of milliseconds. Spatial encoding is introduced by adding gradient coils so that echos from each 3-D location in the image (voxel) experience a unique magnetic field and hence have a characteristic frequency. The radio-waves emitted as the excited protons revert to their ground state contain a wide range of spatial frequency components. This signal is then received by antenna and reconstructed by the fast Fourier transform into 3-D images of the proton density distribution.

The magnetic field is provided by a superconducting magnet submerged in liquid Helium. It has a very high degree of uniformity over the imaging field. Image contrast comes from differences in water (proton) content and magnetic relaxation time of each tissue. In general the image quality depends not only on the echo time T_E and repetition time T_R but also on the selection of voxel size and total scan time. By changing acquisition parameters one can probe various aspects of the spin-spin and spin-lattice interactions to generate T_1/T_2-weighted images. This allows contrast enhancement of different tissues and blood vessels and also provides some chemical information of certain biological molecules. With the continued improvement in the scanner the multi-spectra MR data have become easily available from each subject to better label major tissue structures in the brain.

In this work MR data of the human brain are acquired on a Philips Gyroscan 1.5

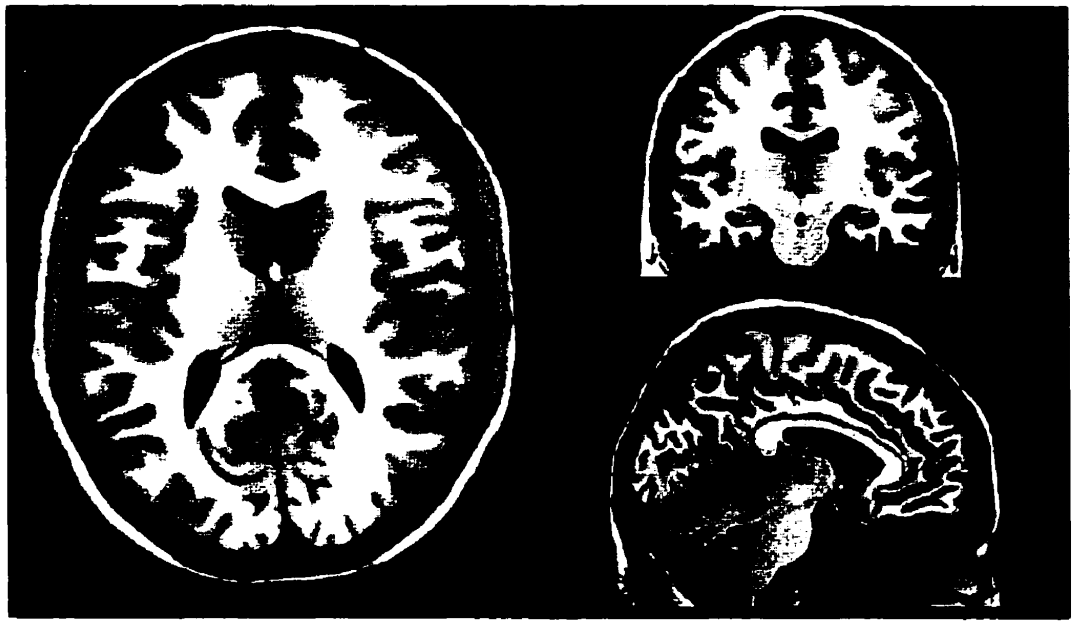

Figure 5.2: 3-D high resolution T_1-weighted MR brain images with 1 mm^3 voxel size. (a) transverse (b) sagittal and (c) coronal views.

Tesla system. Typically we collect multiple contiguous slices using a T_1-weighted 3-D gradient echo sequence. Each transverse slice contains 256 × 256 1 mm^2 pixels with 1-2 mm thickness. Image volumes from the scanner are reformatted and transferred to Unix workstations for further processing. Some correction programs may be used to reduce small intensity nonuniformity caused by the magnetic field inhomogeneity. Fig. 5.2 shows typical volumetric MR images of a normal volunteer with high resolution and excellent contrast between gray matter, white matter and ventricular structures (T_R = 18 ms, T_E = 10 ms and Flip angle = 30°).

5.1.2 Segmentation of anatomical structures

In many neuroimaging study protocols MR scans are registered with PET images and resliced at the desired orientation and thickness. Most registration is performed with Woods' correlation method which minimizes the variance of the ratio between voxels

within the brain volume [Woods et al., 1993]. A manual preprocessing step is required to remove the non-brain regions from the MRI data. Recent work has made this procedure completely automated by fitting a standard 3-D brain mask to MR images of each subject [Collins et al., 1994]. In order to construct computerized 3-D brain phantoms we need to partition MR data into different tissue types and anatomical structures. This is done to identify neuroanatomical structures with unique functional characteristics and tissue attenuation properties.

On the first level we segment MR images into gray matter (GM), white matter (WM), cerebrospinal fluid (CSF), skull bone and skin surface using several automated tissue classification tools [Kamber et al., 1995, Kollokian, 1996]. These algorithms are based on cluster analysis of the mean intensity and variance in small voxel cells using many different classifiers. Both supervised and unsupervised methods exist ranging from simple thresholding to a neural network approach. We select the minimum-distance classifier to generate either discrete or continuous tissue maps representing the fraction of each tissue type belonging to each voxel. This probability (between 0.0 and 1.0) is estimated to be inversely proportional to the distance between each voxel intensity and the mean value of each tissue class. Misclassification in the tissue maps can be corrected by manual editing and by reference to a standard brain atlas.

It may also be necessary to delineate specific, localized anatomical structures such as caudate nucleus, putamen and thalamus in the basal ganglia. They may have unique uptake property for different radiotracers but are indistinguishable on the basis of tissue class alone. For instance the primary regions visible in neuroreceptor imaging studies are the caudate and putamen which belong to gray matter structures. Using image analysis programs available at our laboratory we draw anatomical boundaries of each structure manually on the MR slices [Evans et al., 1991a]. This can also be

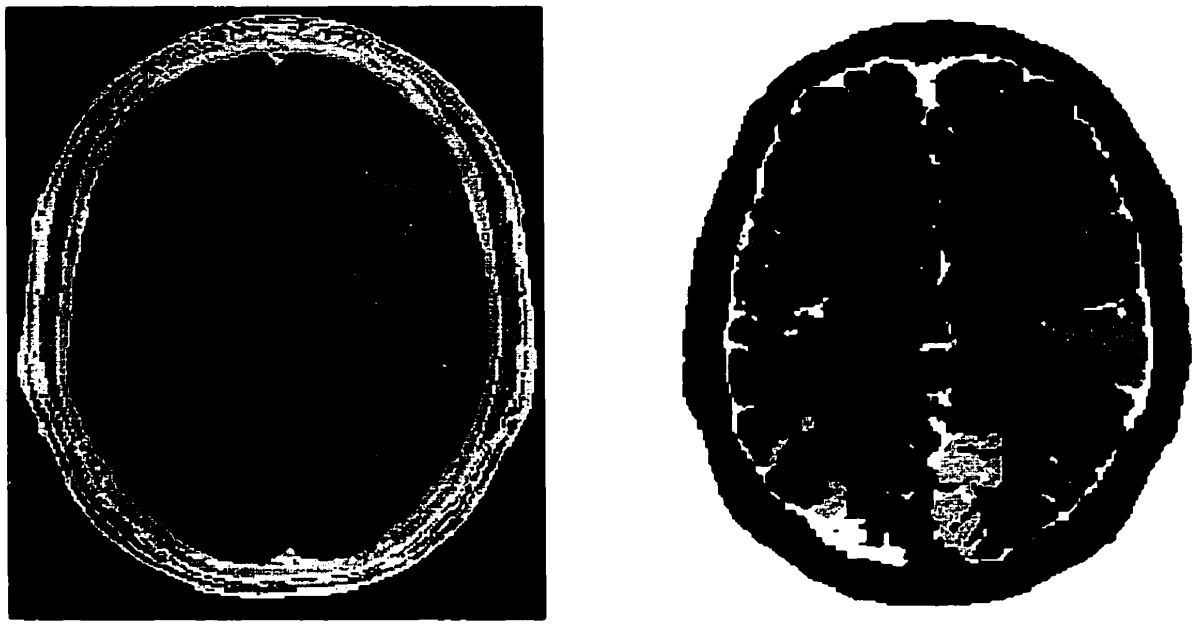

Figure 5.3: 3-D brain phantom of individual tissue maps and neuroanatomical structures (c.f. Fig. 5.2). Courtesy of Drs Louis Collins and Noor Kabani.

done by deformation of any computerized 3-D brain atlas. With recent technological advances we can now identify them using automatic feature-matching algorithms [Collins et al., 1995]. The structural contours from the brain atlas are transposed to the MR images by linear or nonlinear elastic transformations. This allows regional segmentation of anatomical structures with the minimal user intervention.

Consequently the internal voxels of each brain volume are labeled by a tissue or structure ID according to neuroanatomy. Although this binary segmentation is a reasonably good representation of the human brain, it does not reflect the gradual change of tissue contrast at the structural interface. A single voxel in the image may contain several different tissue types. A set of probabilistic tissue maps have recently been created from the 3-D MR images given in Fig. 5.2 [Collins et al., 1998]. Fig. 5.3 shows a discrete version of this digital brain phantom and the corresponding hand-drawn volumetric brain atlas provided by neuroanatomist Dr. Noor Kabani.

Both volumes represent typical examples achievable with the current technology at the MNI. It is possible to generate probabilistic segmentation of individual cerebral structures by combining them.

As an adjunct to this anatomical phantom generator we have also written a program to create geometrical phantoms of varying sizes and shapes. Simple 3-D objects can be inserted into the segmented brain volume to emulate diseased or activated areas. In practice all the procedures described above are combined to model functional regions of interest in PET simulation studies. For instance this would allow us to investigate the influence of scanner or protocol design factors on signal detection in small structures.

5.1.3 Creation of 3-D brain models

In order to perform PET simulations we need to generate brain models to represent realistic 3-D radionuclide distribution in typical neurological imaging studies. This requires a prior knowledge of radiotracer biodistribution in each brain structure. Theoretically this information should come from the observed mean tissue values across the population [Brooks et al., 1987]. It has been shown that the true uptake ratio between GM and WM structures in normal blood flow and glucose metabolic PET imaging is about 4:1 with no activity in CSF space. This corresponds to the relative metabolic rate in each tissue of the monkey brain as determined by autoradiography [Kennedy et al., 1978]. These values can be assigned to each structure in the anatomical brain phantom.

As stated in the first chapter the main objective of this project was to study tissue kinetics. Therefore we created a 3-D dynamic brain model by assigning regional tracer concentration data from a set of theoretical time-activity curves (TACs). The curves

may be generated from any kinetic models with given physiological constants and measured/simulated arterial input function. As shown in neuroreceptor studies both *in vivo* and *in vitro* parameters produce equivalent kinetic curves [Zeeberg et al., 1990]. This process can be done according to the specific imaging protocol used for a given tracer. Fig. 5.4 gives a schematic where $C_i(t)$ denotes the TAC value of each tissue at time t.

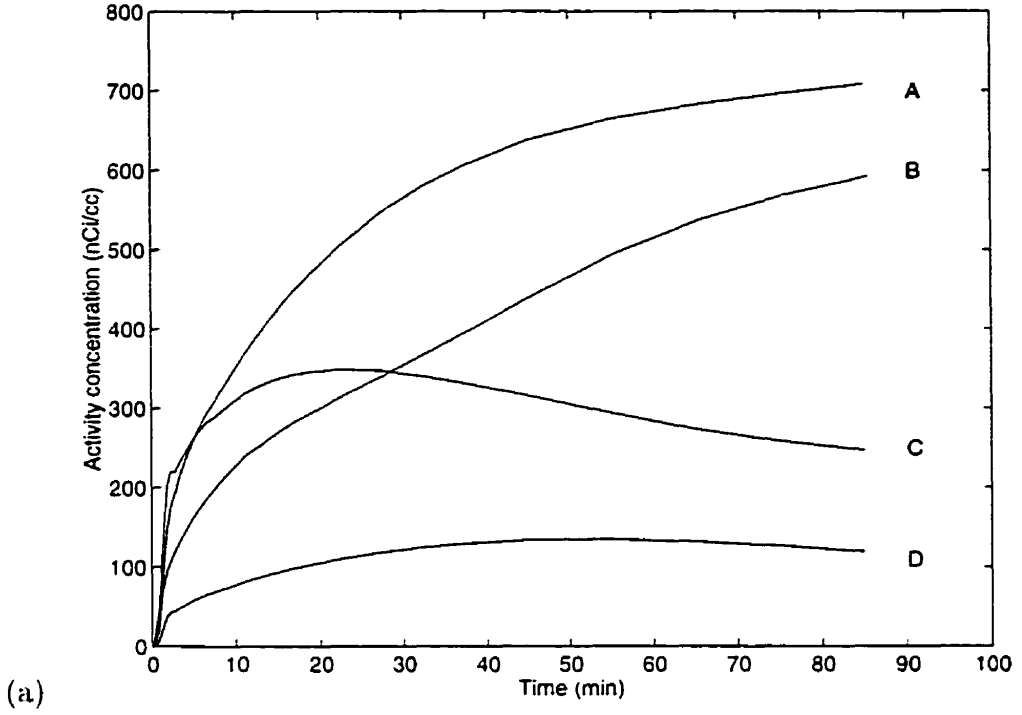

(a)

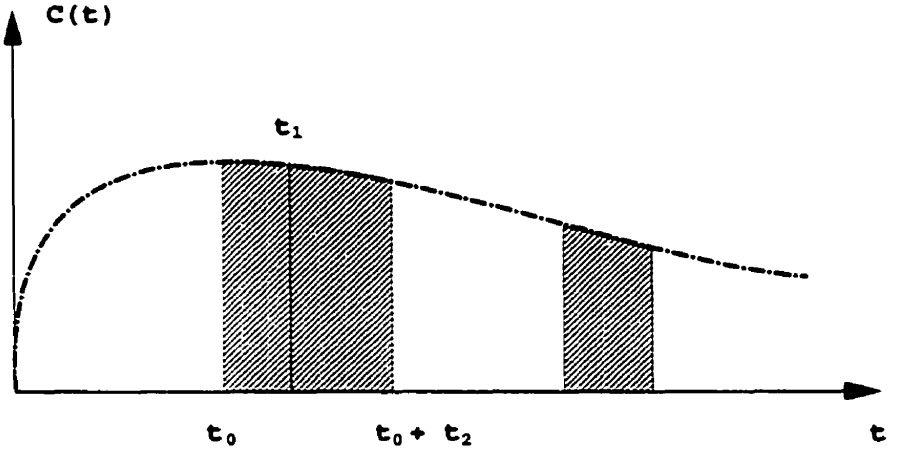

(b)

Figure 5.4: (a) Schematic time-activity curves in a set of tissues with different kinetic properties: dopamine receptor studies with specific (A,B) and non-specific (C, D) tracer uptake. (b) Illustration of temporal sampling where parts of each TAC are integrated over the scan duration (shaded area) to obtain the total and mean activity in each frame. t_0 and t_2 are the start time and scan length while t_1 refers to the mean frame time where the activity value equals the mean activity of the frame.

For rapid generation of PET images it is necessary to sum regional activity concentrations according to the desired temporal sampling strategy (Fig. 5.4). The mean value of each PET frame is calculated for each tissue or structure type by

$$A_i = \frac{1}{t_2} \int_{t_0}^{t_0+t_2} C_i(t)dt \tag{5.1}$$

where t_0 and t_2 denote the start time and scan duration of each frame.

In order to model photon absorption effects in both emission and transmission PET scans we also generate 3-D tissue attenuation maps. Each structure in the brain phantom is assigned with a linear attenuation coefficient. Since Compton scatter is the dominant interaction mechanism for the 511 keV γ-rays, we use the theoretical values for major tissue types in the human body listed in Table 2.2. This information could also be derived from measured PET transmission scans.

It is possible to use spatially correlated X-ray CT scans to verify and obtain attenuation maps with high resolution. This would allow easier identification of bone, soft tissue and sinuses with the largest contrast in their attenuation values. However we should then calculate the linear attenuation coefficient from the CT numbers at each voxel and adjust for the photon energy difference between the CT and PET transmission sources as suggested by other workers [Chen et al., 1992].

In the previous section we assumed that tracer uptake and attenuation values are homogeneous in each structure of the 3-D brain phantom. In biological organs their distributions may be variable both within a given tissue type and across structural boundaries. This arises from non-uniformity in the uptake properties of each tissue and the absence of any barriers between them. We could incorporate some gradients based on heterogeneity data from clinical observations. This can be done by regional activity assignment with some form of spatial weighting. In most cases we smooth sharp edges in discrete image volumes using a uniform 3-D Gaussian filter.

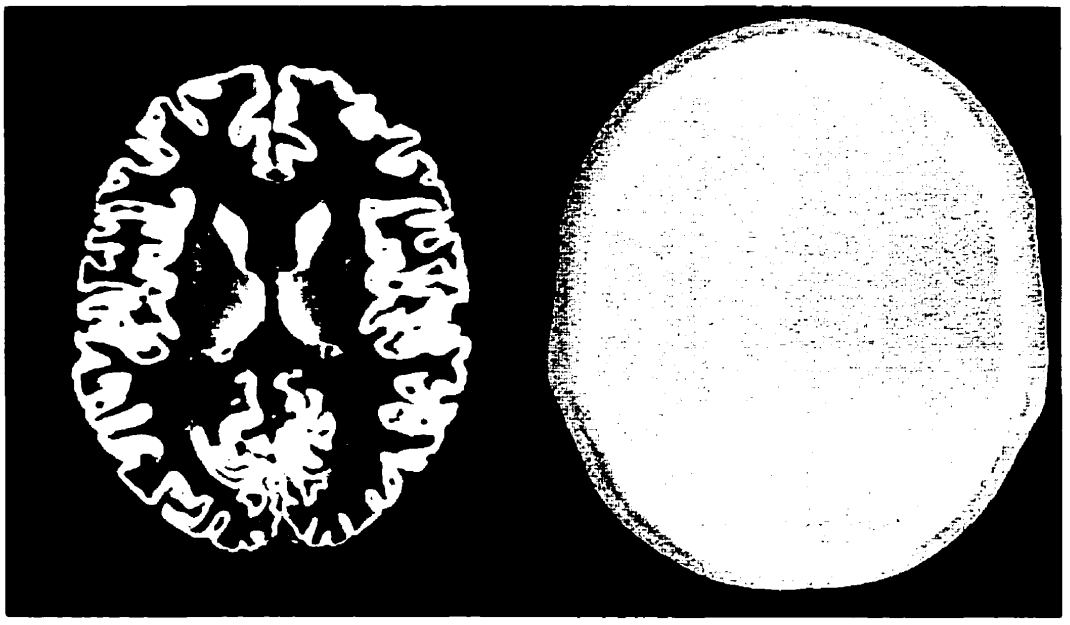

Figure 5.5: (a) 3-D brain model representing realistic activity distribution as in blood flow and metabolic images. (b) tissue attenuation map with only soft tissue (plus skin) and skull bone. Both are equivalent to ideal emission and transmission PET images without any physical distortions.

We can create a more realistic brain model by the weighted sum of regional activity and attenuation data with the probabilistic tissue phantom. Each voxel has a value

$$B_i = \sum_{j=1}^{N} A_j V_j \tag{5.2}$$

where A_j is the mean activity value calculated above and V_j is the probability of each tissue type within each voxel. Fig. 5.5 shows the continuous 3-D brain model with non-uniform radioactivity and attenuation distribution in each structure. A brain phantom can also be created from *in vitro* autoradiographic data of the animal population with both anatomical and functional content. These volumes are calculated before considering the physical factors which degrade the PET image in practice. Both are required in subsequent projection simulation and image reconstruction.

5.2 Physical Models of Data Acquisition

PET cameras acquire projection data of an unknown radiopharmaceutical source distribution at many axial, angular and radial positions. This section describes the mathematical models of data collection. We use $f(x, y, z)$ and $\mu(x, y, z)$ to denote the activity distribution and tissue attenuation map in the voxel-based 3-D brain phantom. We ignore the time variable to simplify the presentation. Time-varying changes in regional contrast are simply handled by calculating the ideal image at each time point in a dynamic series of PET scans. In digital terms both functions f and μ are represented by a set of 2-D slices stacked together. 3-D matrix and voxel dimensions are selected according to (a) size and accuracy of the object representation; (b) resolution of the imaging system; and (c) computation considerations.

Realistic simulation of projection data should incorporate all physical components inherent in tomographic coincidence imaging. Besides the non-uniform 3-D sampling geometry and resolution this must also include other distortion factors defined in the equation below. The total counts at each detection position is given by

$$P_k = [(T_k + S_k)D_k + R_k]W_k \tag{5.3}$$

$$T_k = I_k A_k N_k C_k \tag{5.4}$$

where T_k, S_k and R_k are the estimated rates for true counts, scatter and random events respectively. I_k denotes the activity projection with finite 3-D tomography resolution. A_k, N_k and D_k represent the attenuation factor, detector efficiency and deadtime factor. Note that these variables are all sinograms for each image plane. C_k refers to the radioactivity decay while W_k is the fraction of total exposure time in each wobble position independent of slice and angle. W_k equals the total scan time in stationary mode. The next sections describe the calculation of these components.

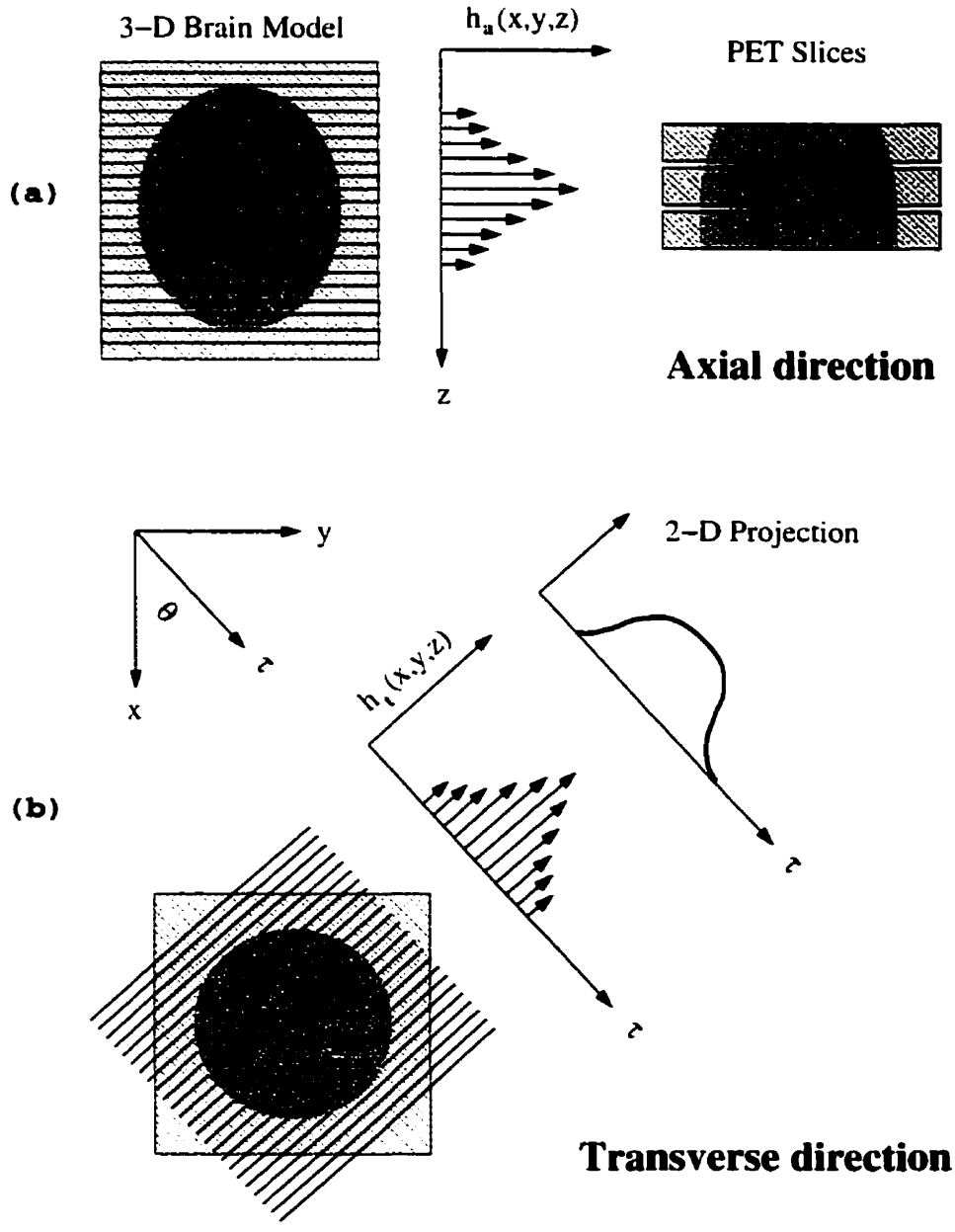

Figure 5.6: A schematic diagram of simulation geometry in a multi-slice system. The upper portion (a) shows how activity in the phantom is integrated with axial response function h_a to form PET slices. The lower one (b) illustrates in-plane projection through the object and convolution with weighting function h_t to create a particular profile at angle θ.

5.2.1 True coincidence rates

The measured projection data of any source distribution can be modeled by a convolution between the true projection of the source and the 3-D detector response function of the scanner. This operation becomes a weighted integration since the point-spread function (PSF) is generally spatially variant over the imaging field. Because PET systems transform 3-D activity distribution into a stack of transverse slices, the sampling process can be handled separately in the axial and in-plane direction. Fig. 5.6 shows the coordinate system of forward projection to compute I_k in equation 5.4.

Step 1: Axial convolution:

For computation efficiency we model the axial sampling and resolution effects before the reprojection step. Transverse slices in the 3-D brain model are weighted and summed along the z-axis. This gives the axially-smoothed source distribution $g(x, y, \eta)$ and attenuation map $v(x, y, \eta)$ as a set of cross sections.

$$g(x, y, \eta) = \int_{-\infty}^{\infty} f(x, y, z)\, h_a(x, y, z, \eta)\, dz \tag{5.5}$$

$$v(x, y, \eta) = \int_{-\infty}^{\infty} \mu(x, y, z)\, h_a(x, y, z, \eta)\, dz \tag{5.6}$$

where $h_a(x, y, z, \eta)$ represents the axial component of the 3-D PSF at each position. The variable $\eta = (i-1) \times Z + Z_0$ corresponds to the location of each image plane with i = 1,...N_S. N_S is the total number of PET slices and Z the inter-slice spacing. Z_0 is the axial distance between the MRI and PET volumes. usually known with respect to some anatomical landmarks (e.g. orbito-meatal line) after registration. We can control the position of the brain model relative to the scanner by selecting different Z_0 in the axial direction following any other 3-D transformation. Fig. 5.7 presents typical images of the 3-D brain model after the axial resampling and convolution.

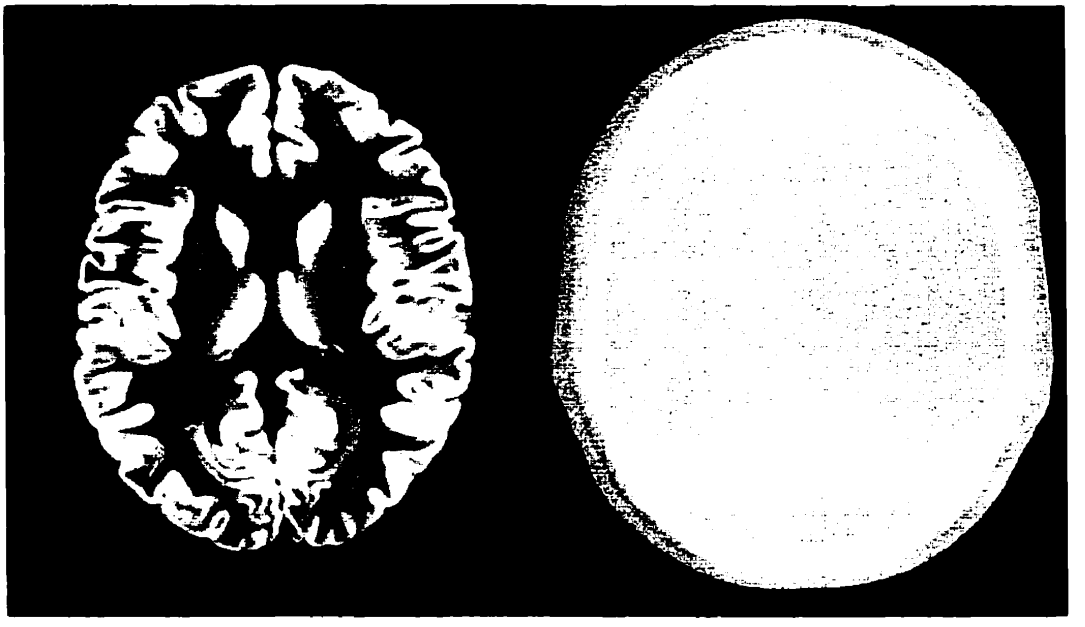

Figure 5.7: 3-D brain phantom after the axial weighting but prior to the in-plane projection. It has a 6 mm thickness and a 6.5 mm separation (c.f. Fig. 5.5). Notice the image degradation introduced by the finite axial resolution and sampling of the PET system.

Step 2: Transverse projection

We compute the projection data for each image plane at appropriate angular and transverse positions. For easy discussion we use both subscript k and coordinates (τ,θ,η) to represent variables at the same location of the projection space. In the absence of any distortion and with a delta-function detector response, we obtain the idealized line integral by the projection operator.

$$I_k = p(\tau,\theta,\eta) = \int\int_{-\infty}^{\infty} g(x,y,\eta)\, w(x,y,\tau,\theta)\, dxdy \tag{5.7}$$

where $w(\tau,\theta,\eta)$ refers to the fraction of each pixel intercepted by a projection strip at angle θ and ray τ. This integration is done with uniform sampling at the corresponding angular positions in the scanner. Currently this is computed using a reprojection routine available as part of a X-ray CT simulation package called SNARK89 [Herman et al., 1989]. Since this program can handle only odd numbers of rays and

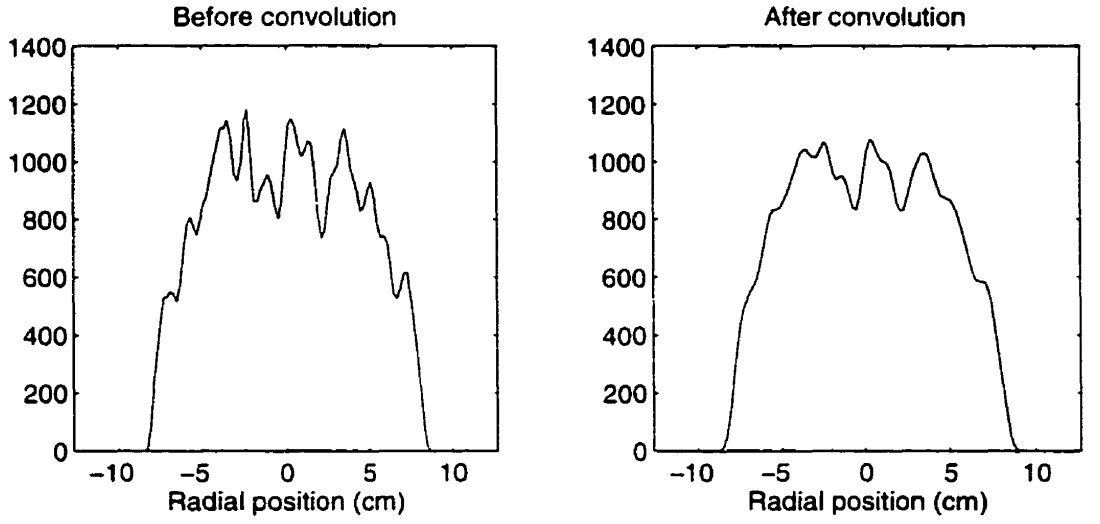

Figure 5.8: Simulation of detector resolution effects where projection profiles are smoothed by convolving with a 6 mm FWHM Gaussian at each angle.

image sizes we perform some interpolations to map data between the coordinate systems.

In the presence of finite transverse detector response we adjust the projection data by the convolution equation

$$I_k = p(\tau, \theta, \eta) = \int_{-\infty}^{\infty} p(\tau', \theta, \eta)\, h_t(\tau', \tau, \theta, \eta)\, d\tau' \tag{5.8}$$

where $h_t(\tau, \theta, \eta)$ refers to the in-plane PSF of the system. At this stage we use thin and equally spaced rays in the calculation to avoid undersampling. Fig. 5.8 shows sample data extracted from the simulated sinogram of the 3-D brain phantom. For each image slice the complete data contain 128 angles and 128 rays with an increment of 1.406° and a ray spacing of 2 mm respectively.

Most photons from positron sources are absorbed in tissues before reaching the coincidence detectors. This attenuation effect may increase by a factor of eight from the edge to the center of the human head. We determine the amount of photon

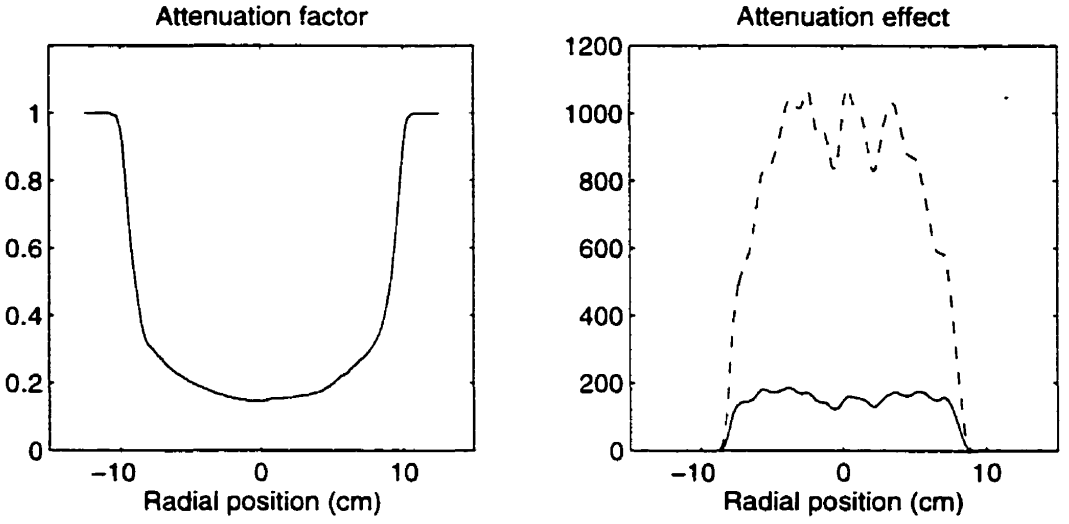

Figure 5.9: Simulated projection profiles before (- -) and after (—) applying the photon attenuation factors on the left. Note the great drop in the magnitude of projection data by attenuation.

absorption by calculating the attenuation factors.

$$A_k = a(\tau, \theta, \eta) = exp(-\int\int_{-\infty}^{\infty} v(x, y, \eta)\, w(x, y, \tau, \theta)\, dxdy) \tag{5.9}$$

where $v(x, y, \eta)$ is the axially-weighted attenuation maps obtained above and the computation follows the same procedure as used for equation 5.7. Projection data from equation 5.8 are then multiplied by the corresponding attenuation factors at each angle and position. As shown in Fig. 5.9, it is necessary to include attenuation effects in the object to correctly model counting statistics in the projection data.

Each projection profile is then modulated by the detection efficiency in the form of the inter-slice sensitivity (cps/nCi/cc) and spatially variant normalization factors. We use the measured efficiency data and its position dependence as derived from Chapter 4. By this calibration step one can assign radioactivity to the brain phantom in absolute units of nCi/cc. In addition we apply a radioactivity decay factor to each

projection element,

$$C_k = exp(-t_1/\tau^*) \qquad t_1 = t_0 + \tau^* \, ln(\frac{t_2/\tau^*}{1 - e^{-t_2/\tau^*}}) \tag{5.10}$$

where $\tau^* = T_{1/2}/ln(2)$ and $T_{1/2}$ is the half-life of a particular radioisotope. Note that $C_k < 1$ and it can be calculated relative to any starting point based on the temporal sampling of each frame (see Fig. 5.4). Given the start time t_0 and the scan length t_2 in each frame, the mean time t_1 is reduced to the midtime $(t_0 + t_2/2)$ when $t_2 \ll T_{1/2}$.

5.2.2 Scatter coincidence rates

For one image slice scattered radiation may come from activity in the direct plane and adjacent planes. At present we model only intra-plane scatter analytically by means of a 1-D convolution algorithm in the projection space. This is applicable in multi-slice PET systems where inter-plane septa effectively eliminate most other scatter events. Scatter count rates in each projection position are computed by

$$S_k = s(\tau, \theta, \eta) = \int_{-\infty}^{\infty} p_a(\tau', \theta, \eta) \, f_s(\tau', \tau, \theta, \eta) \, d\tau' \tag{5.11}$$

where $p_a(\tau, \theta, \eta)$ is the true coincidence rates and $f_s(\tau, \theta, \eta)$ the spatially variant scatter response function. The latter is derived from the line-spread function (LSF) in water such that its convolution with the peak equals the count profile below the tails. A similar algorithm has been implemented in iterative image reconstruction [Daube-Witherspoon et al., 1992]. As described in section 3.1.3 this filter is represented by a sum of multiple exponential functions in the form of $\alpha \, exp(-\beta \, |\tau|)$. Both coefficients α and β vary with spatial location. It is further modulated by the corresponding attenuation factors of the scatter medium.

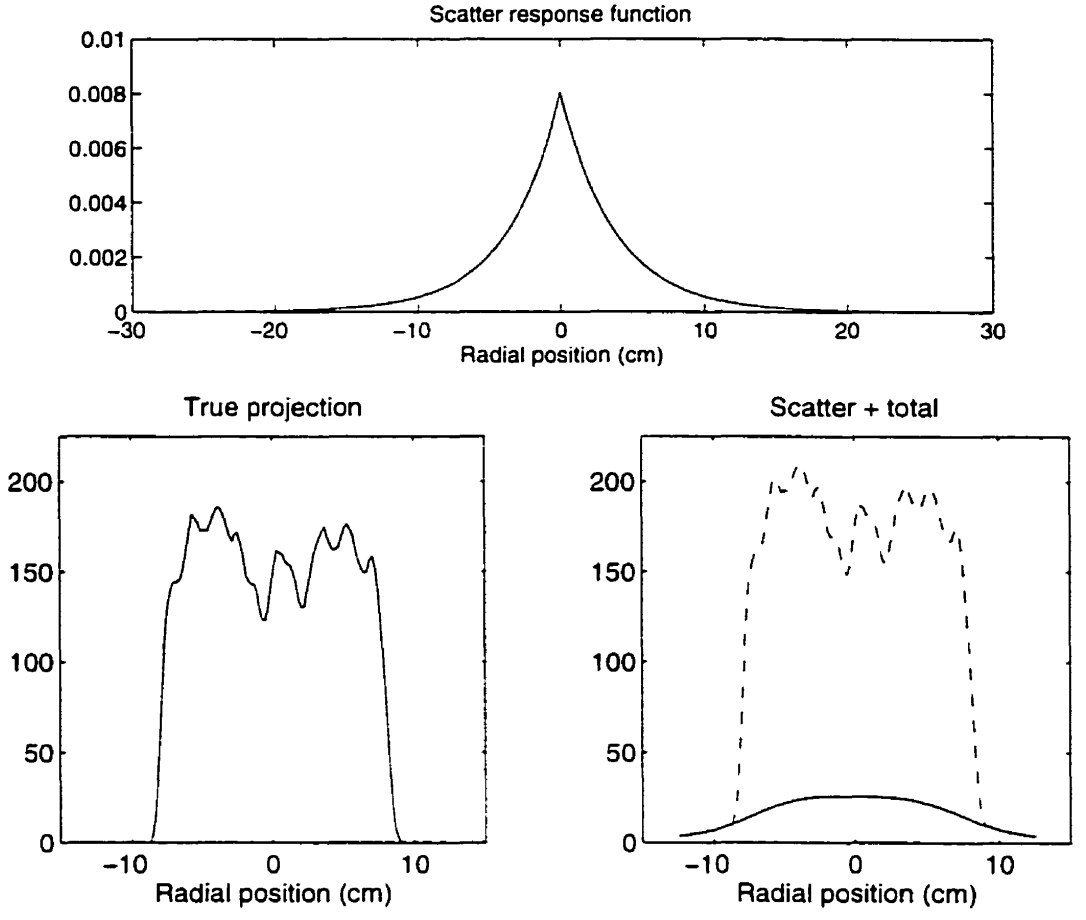

Figure 5.10: Demonstration of scatter simulation: the attenuated projection data on the lower left are convolved the exponential scatter filter function (top) to give the scatter (—) and total (- -) profiles on the lower right. Note that scatter is only a small fraction of the total with slight spatial variation.

A different version of this filter (h_s) is usually available in the image reconstruction program of individual tomographs. It gives the same scatter profile when convolved with the observed LSF in water. We employ the algorithm that is used in the PC2048 scanner for scatter correction from the total projection data. However we use the simulated true projections and attenuation factors and modify the filter function by the relationship

$$f_s = \sum_{n=1} h_s^n = h_s + h_s^2 + ... \tag{5.12}$$

This simple formula is derived from equation 3.3 in section 3.1.3 by expansion since h_s is much less than 1. In the present work we choose only the linear term because scatter forms a low and smooth background with a slight increase towards the center (Fig. 5.10). The smaller amount of additional scatter contributed by the higher order terms is handled explicitly by a scaling factor. This empirical parameter is determined for each PET camera to have the same total scatter counts as in phantom scans.

In a Monte Carlo study with geometrical objects Thompson has demonstrated accurate scatter estimation by the 1-D convolution method even in volumetric imaging [Thompson, 1993]. It is known that the scatter fraction in 3-D systems is more than 3 times higher than that in the multi-slice 2-D scanner. As one would expect this method does not provide a good solution with a complex 3-D source distribution. In such situations we can further simulate the inter-plane scatter using equation 5.6. However it would then be necessary to derive a different filter function by modeling point source profiles in both the in-plane and axial directions.

5.2.3 Deadtime and randoms rates

Deadtime effects begin to dominate at high count rates as seen in blood flow studies with O-15 bolus water. We have the same kind of problem with randoms. Both depend on singles rates and lead to nonlinear distortion of raw projection data in any dynamic series. Ideally one should model them based on the observed deadtime and randoms data between each pair of detectors. However we expect their distributions to be more or less uniform in the projection space because singles rates vary slowly across the imaging field.

While the deadtime factor (D_k) and randoms (R_k) may greatly change the total count rates between dynamic data frames as seen in equation 5.3, they only affect

count statistics slightly among projection positions within individual slices. As a result we choose one easy way to estimate the deadtime and total randoms for each image plane. The deadtime factor of the slice is used as D_k at each member position. We distribute the total randoms (R) uniformly into all detector pairs to obtain

$$R_k = r(\tau, \theta, \eta) = R/(N_P N_R) \tag{5.13}$$

where N_P is the number of angles over 180° and N_R the number of rays at each angle. This is done according to the measured deadtime factor (D_F) and random fraction (R_F) curves of the flood phantom given in Chapter 4. We add both randoms and deadtime factors based on the total count rates ($T + S$) in each slice calculated from T_k and S_k data generated above.

5.2.4 Projection interpolation

Simulated components are put together to form total projection data. Count rates at each projection element are further multiplied by a time varying factor representing the scan length of each frame. Note that these computations are done with uniform angular and linear steps so that they can be subsequently mapped into desirable detector positions of any particular tomograph. As shown in section 2.2.2 the locations of the coincidence lines of response are non-uniformly distributed and depend on the gantry geometry. The count profiles are then interpolated and integrated onto individual detectors using the geometrical specifications of each scanner. This is important since the total counts in the raw projection data determine the noise characteristics in each detection channel.

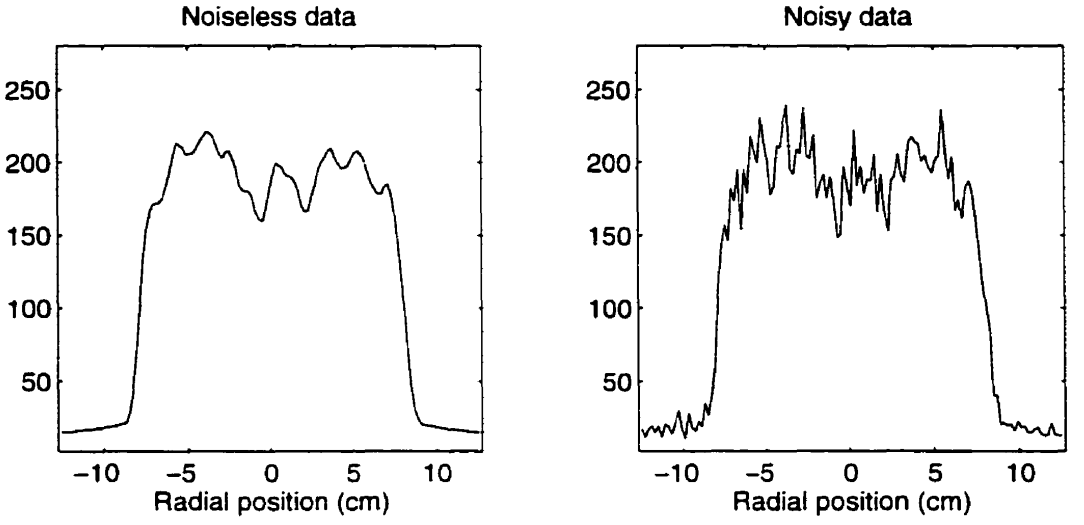

Figure 5.11: Simulated total projection data before and after including statistical noise. Both data correspond to 2 M slice counts with a scatter fraction of 14.5 % and a random fraction of 10 %.

5.2.5 Counting statistics

Realistic simulation of a PET imaging system must recognize the counting statistics of projection measurement. We generate multiple realizations of noisy projection data by replacing the counts at each element with random numbers (Fig. 5.11). In theory they can be drawn from a Poisson probability distribution whose variance equals the total counts (p) computed above for each line of response. We employ two random functions from the numerical recipe book [Press et al., 1992]: Poisson $posdev(p)$ and Gaussian $gasdev(p) = p + q\sqrt{p}$. q generates normally distributed values between [-1,1] with zero mean and unit standard deviation. We initialize the random number generators with the computer clock to ensure that each noise run is independent. Histogram analysis shows that both functions are equivalent when $p > 10$. Simulated total counts at each position match those collected in typical imaging applications making statistical noise consistent with that measured in PET scan data.

5.2.6 Transmission count rates

We simulate PET transmission scans in order to investigate the effect of attenuation correction on regional image quantification. We can use a stationary ring to model radioactivity distribution of the rotating pin source in the scanner. Blank (I_B) and transmission (I_X) data are then generated without and with attenuation from the 3-D brain model. Physical effects can be incorporated into the simulation as discussed in the previous sections.

At present we implement an empirical transmission model based on the measured blank data. The raw projection data of a typical blank scan are extracted and averaged over all angles. The angular mean profiles are fitted to a cubic polynomial and used as the input sinogram from a rod source. Note that this sinogram contains the effects of detection efficiency and deadtime as well as a small amount of scatter and randoms. Noisy projection data I_B and I_X are then obtained using a Poisson distribution, with the mean values at each projection element calculated according to the same steps given in section 5.2.1. Due to the very long half-life of the radioactive pin source we neglect the decay effect between them. When generating I_X we include all physical factors inherent in PET transmission measurement except scatter and randoms. Both effects are assumed to be small and ignored in the PC2048 scanner.

This simple model allows us to simulate blank and transmission sinogram data from the attenuation maps of the 3-D brain phantom. As shown in Fig. 5.12 one can then compute noisy attenuation correction factors to either reconstruct emission data or generate realistic PET transmission images.

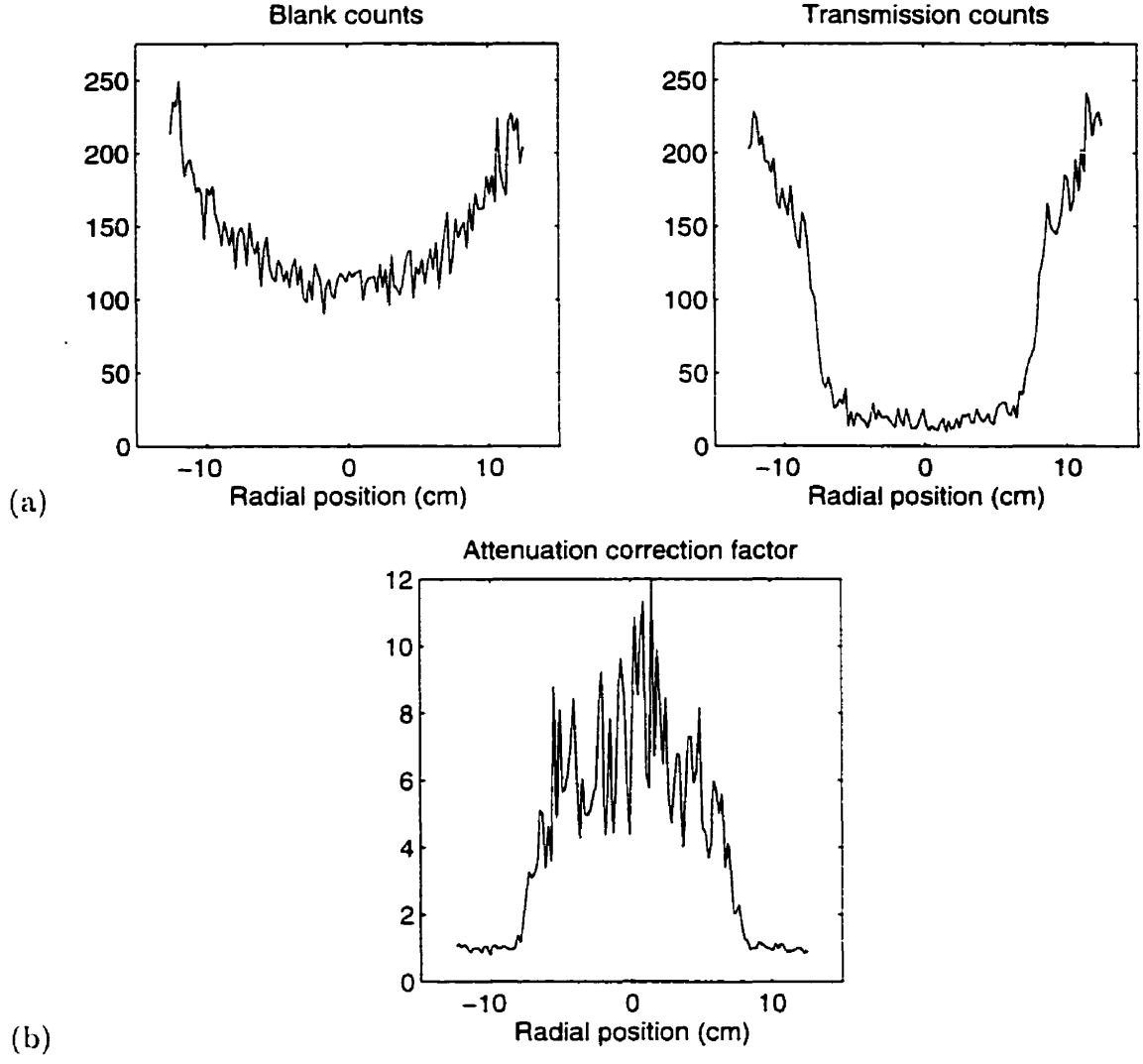

Figure 5.12: Illustration of PET transmission simulation with noise: (a) Count profiles of the simulated blank and transmission scans. (b) Attenuation correction factors calculated from (a) showing noise magnification.

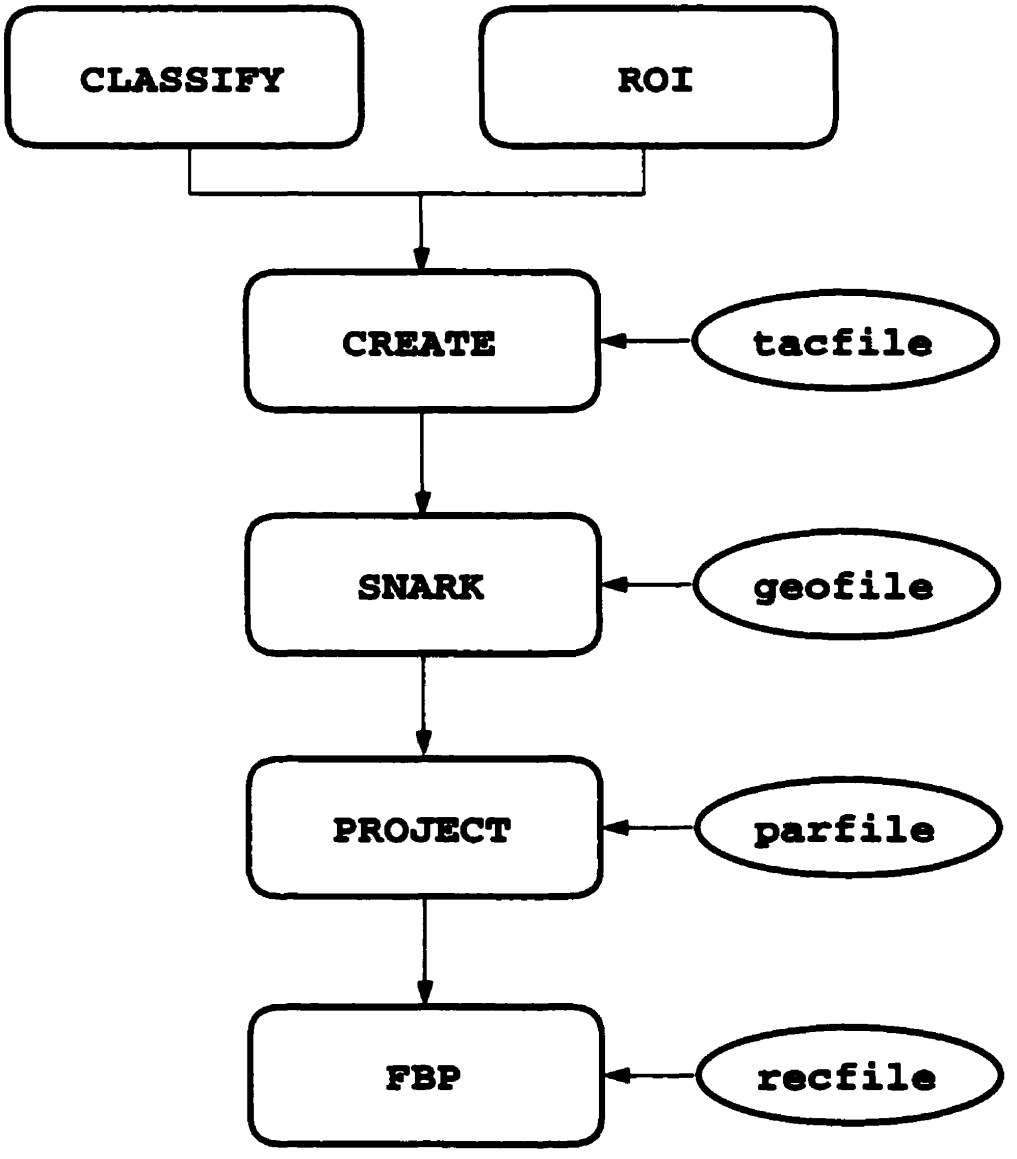

Figure 5.13: Program structure of PETSIM system. These software tools carry out the simulation tasks listed in Fig. 5.1 with the functionality of each program and file described in the text.

5.3 Implementation and Computational Issues

Our simulation system has been implemented on Unix workstations using the *C* and *Fortran77* programming languages. Fig. 5.13 is a block diagram to link the program components and parameter files. We take a modular approach so that one can perform object creation, sinogram generation and image reconstruction separately. In addition each physical effect in the projection and backprojection chains can be included independently or together. This tool works for any 3-D object models and multi-slice PET scanners. A shell script *PETSIM* is currently used to control the simulation programs as summarized below.

CLASSIFY and *ROI* perform tissue classification and structure delineation respectively with both manual and automatic methods. Using *CREATE* we generate 3-D activity phantom and attenuation maps with both binary and continuous intensity distribution. This depends on the nature of image segmentation and biodistribution data provided in *tacfile*. This file stores necessary tissue time-activity curves (TACs) and time information of each frame as well as the attenuation value of each tissue. axial weighting and interpolation. *SNARK* is then used to compute 'ideal' projections from each axially-weighted slice according to the geometrical data in *geofile*. With *PROJECT* we calculate realistic sinogram data and include physical effects as described above. This is based on *parfile* representing a list of simulation parameters of key characteristics of each scanner. Finally we perform filtered-backprojection image reconstruction with *FBP* which reads input parameters from *recfile*.

PETSIM is driven by many command-line options and a set of study and camera specific parameter files. Users can specify any numerical and character variables from these standard text files. In practice we create typical imaging protocols, each with a standard *tacfile* and *recfile*. We also have sample *parfile* for each tomograph based on

the performance figures available. These files are stored permanently as a common database and define default settings except those supplied from the command-line argument. After proper preparation *PETSIM* runs in batch mode to simulate both static and dynamic studies.

PETSIM produces a set of sinogram and image data along with a log file to record the progress of the simulation. Individual header files keep all information related to simulation and reconstruction. These auxiliary files are necessary to examine the results and to diagnose errors. Logically this is done in the order of blank, transmission and emission scans. Dynamic emission data are created and stored separately for each frame in the dynamic sequence. These may be acquired continuously or intermittently from any number of slices and frames. Once the simulated sinograms have been generated, they can be submitted to regular reconstruction algorithms in a manner identical to that used for real data.

During the early development of this project we modified the image reconstruction program on the Scanditronix PC2048 scanner to serve two purposes: (1) handle emission and transmission scans from simulations; (2) extract components of the measured projection data at different processing stages. The second aspect is necessary for the validation of the simulation system in the next chapter. Prior to backprojection we correct for physical effects in the simulated data in the same manner as is done in real image reconstruction. Fig. 5.14 presents the simulated blood flow and transmission PET images generated from the 3-D brain model in Fig. 5.5. With a 6 mm slice thickness, both contain noisy data with 2 M and 10 M total counts respectively and are reconstructed with a 8 mm Hanning filter.

As part of an ongoing collaboration our simulation programs have also been implemented at the Johns Hopkins University PET center. The primary goal of this was

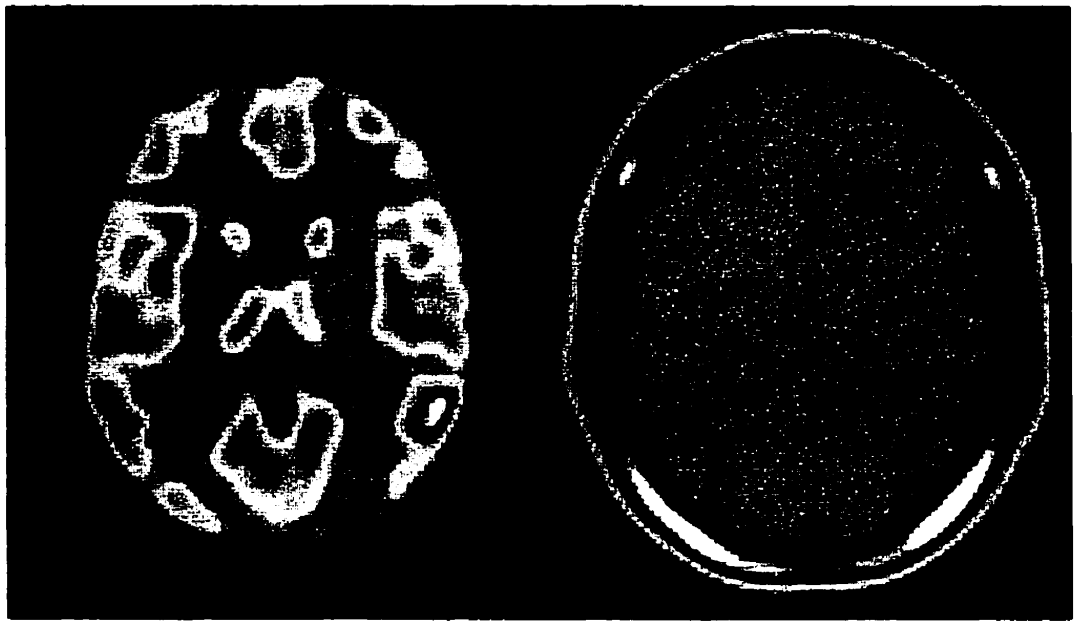

Figure 5.14: Simulated emission (a) and transmission (b) images reconstructed to a 10 mm resolution. Voxel size is $2 \times 2 \times 6$ mm^3.

to study and correct the 3-D partial volume effects in clinical neuroreceptor imaging. We have made software modifications to the PC4096 body scanner to reconstruct the simulated images as in the PC2048 system. In both cases it was necessary to transfer the simulated sinogram data over the network to the tomograph's storage space. In order to increase overall efficiency, we translated portions of the reconstruction program from *VMS Fortran* to *C*. This code was ported to Unix computers along with the scatter/attenuation correction methods and related filter functions. We have also added different smoothing filters for the blank and transmission data before calculating attenuation correction factors.

This programming work not only enhances the structural integrity of *PETSIM* but also improves its portability. The ported program and the scanner software have been compared using scan data from a uniform phantom. Both the mean and standard deviation values have a discrepancy of less than 0.5 % over a 16 cm circular

region. This confirms that the two reconstruction programs are equivalent within the rounding errors. Corrections of physical distortions can be done independently or intertwined between real scan and simulation data. This feature is very useful to evaluate the validity and performance of different compensation algorithms.

We have incorporated many additional steps to achieve fast computation and to ease the use of *PETSIM*. The main feature allows one to execute each component of *PETSIM* successively and save intermediate results. In a subsequent study, one can rerun later portions of the simulation in a different way by recycling data from an earlier step. Users also have options to run only a couple of computation modules at a time before proceeding to the next one. We gain most speed by performing temporal and axial integrations before transverse projection. The basic data are usually generated without noise so that they can be further processed without repeating the costly projection step. This is very valuable since it allows us to model different activity injection or scan conditions and obtain multiple noisy samples with identical counts. One may also want to reconstruct noisy data with different filters or distortion correction methods.

Most studies reported in this thesis have been performed on the PC2048 system described in Chapter 4. We modeled its 3-D PSF by a spatially-invariant Gaussian function normalized to unity and defined by FWHMs along each direction. A typical simulation employs brain models with 1 mm pixels and 2 mm thick slices. Coincidence data are generated with 128 angles and 128 rays with a transverse distance 2 mm, and reconstructed onto a 128 $\times$ 128 matrix with 2 mm pixels. On an SGI Challenge server (150MHz R4400, 98 specfp92, Silicon Graphics Inc.) it takes about 10 minutes of CPU time to produce 15 slices of data incorporating all physical effects of the tomograph. Reconstruction of each image takes 5 seconds and only a few slices are

needed in most imaging applications.

In addition to forward and back projections, mathematical operations involved in *PETSIM* include interpolation and integration in both image and projection spaces. We perform them in the real domain in order to handle the nonstationary PSF down the road. When its spatial variation is negligible, the weighted sums become simple convolutions which could be computed rapidly by the fast Fourier transform. In practice this happens when imaging small objects such as animals with large body scanners. Compared to the 3-D resolution of the scanner, the voxel size in the brain model and sampling rates in projection simulation are adequate - 1.5 times higher than that required by the Nyquist theorem. Although still finer spacing could be used to calculate projection data at the 'infinite' resolution one may not gain any more information except increasing computation time.

5.4 Summary

In this chapter we have presented an extensible software system to perform projection data simulation and image reconstruction in dynamic PET studies. In particular the methods use 3-D brain models created from volumetric MR images and generate sinogram data by incorporating all features of a PET scanner. Besides detector efficiency, deadtime and resolution we also include photon attenuation, scatter and accidental coincidences along with temporal sampling and radioactive decay of each frame. Additionally, blank and transmission data are simulated for realistic attenuation correction. This combination offers a powerful tool to evaluate PET imaging methodology involving both emission and transmission scans.

Chapter 6

Experimental Validation and Verification

In this chapter we describe a series of phantom studies to validate the computational algorithms detailed in Chapter 5. As a general strategy we compare the measured and simulated data in both sinogram space and image space. In particular we want to verify physical components of resolution, attenuation, scatter and randoms. Every component is evaluated independently to avoid any confounding effects between them. This process should be done on each type of PET camera based on physical performance parameters. Besides using available tools, a set of new computing programs has been written to analyze projection profiles and some image data.

Our simulations match the configurations of the PC2048 brain and PC4096 body scanners (see Chapter 4) used at the MNI and the Johns Hopkins University respectively. Several geometrical and anatomy-based physical phantoms were scanned under a wide variety of imaging conditions. In each case they were first filled with water and centered in the gantry via laser beams and external markers. Blank and transmission data were acquired for 10 minutes each and smoothed with a 10 mm Gaussian in order to perform attenuation correction. After filling with radioactive solution the same

physical markers were used to reposition the phantom. Simulated projection data of the digital phantom were generated with all scan-related parameters extracted from the image header of each study.

6.1 Sphere Phantom

In order to verify the accuracy of the simulated point-spread function (PSF) we used six hollow spheres with inner diameters of 4, 7.5, 8.5, 11, 13 and 15.5 mm (Fig. 6.1). They were filled with a uniform activity of Ga-68 solution and inserted in a 20 cm diameter water cylinder. This phantom was then scanned on the PC4096 tomograph with the equators of spheres aligned with one image plane. The starting activity concentration was 56.3 μCi/cc and 2 M counts were collected in the central slice within 10 minutes. Transmission attenuation correction was performed after randoms and scatter subtraction.

A simulated sphere phantom was created with geometrical dimensions and configuration identical to those of the physical phantom [Rousset et al., 1993]. This digital phantom was represented by a series of 2 mm thick slices, with a constant activity in each sphere but in the absence of background activity. We generated noisy projection data with 2 M total counts while simulating all other physical effects.

Real and simulated data of the phantom were reconstructed with a 5 mm Ramp filter to the intrinsic image resolution of 6.8 mm (Fig. 6.1). Note the decrease in activity values as the spheres become smaller, with the smallest ones invisible in both cases. Recovery coefficients (RCs) were then determined for each sphere by normalizing the mean activity of the 5 maximum pixels (20 mm^2) to the true isotope concentration. We also calculated their theoretical values from the Gaussian integral over spheres [Kessler et al., 1984].

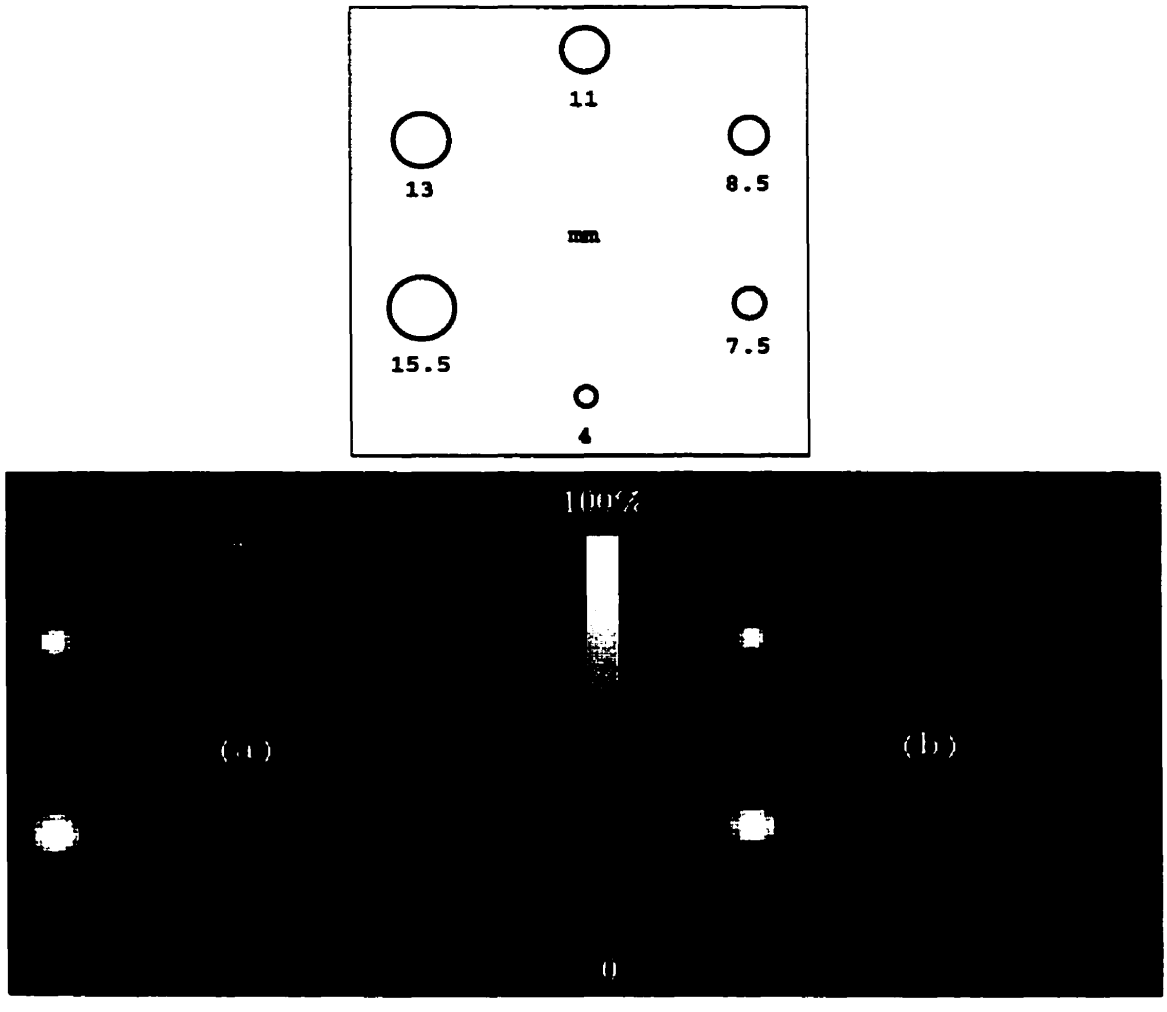

Figure 6.1: A schematic illustration of six spheres with diameters ranging from 4 to 15.5 mm. Note that the spheres are inside a cylinder. (a) Real and (b) simulated images of the sphere phantom.

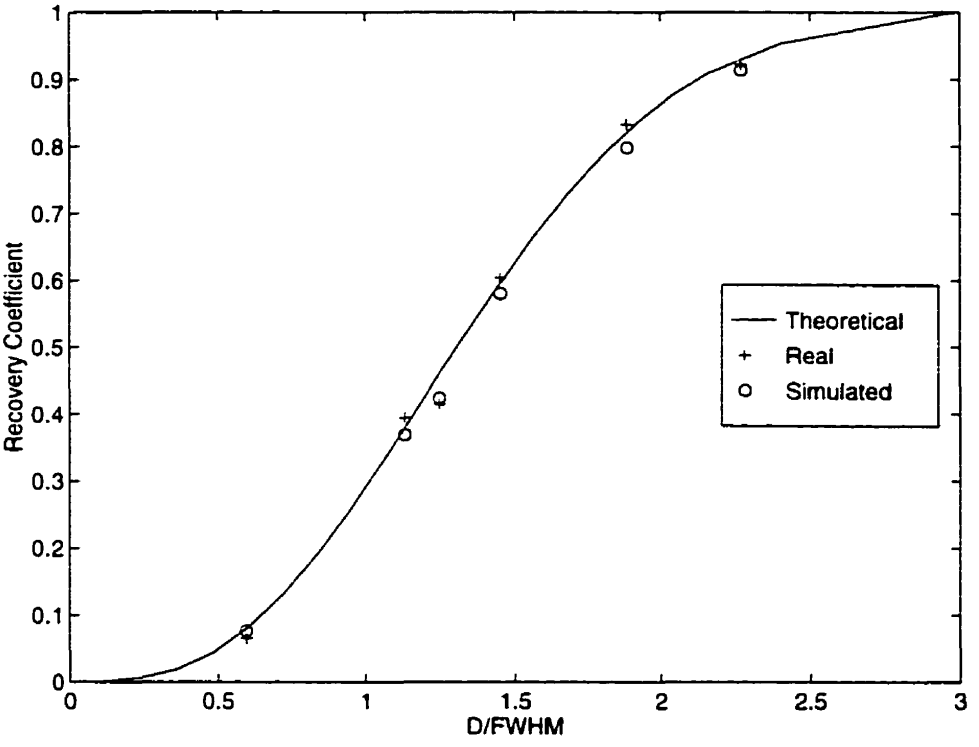

Figure 6.2: Recovery coefficients as a function of sphere diameter (D) normalized to the image resolution (FWHM).

Fig. 6.2 compares RCs versus the ratio of the sphere diameter to the FWHM of the system PSF. The measured and simulated values agree with the theoretical data within 2 %. RC rises from 0.3 to 0.8 as the object size increases from 1 to 2 FWHM, and approaches 1 when the ratio is more than 2.5. It clearly shows the underestimation of activity concentration which becomes more significant in smaller structures or at lower image resolution. This simply confirms the partial volume effect in a cold background. More importantly these results demonstrate accurate agreement between the simulated and real resolution of the scanner.

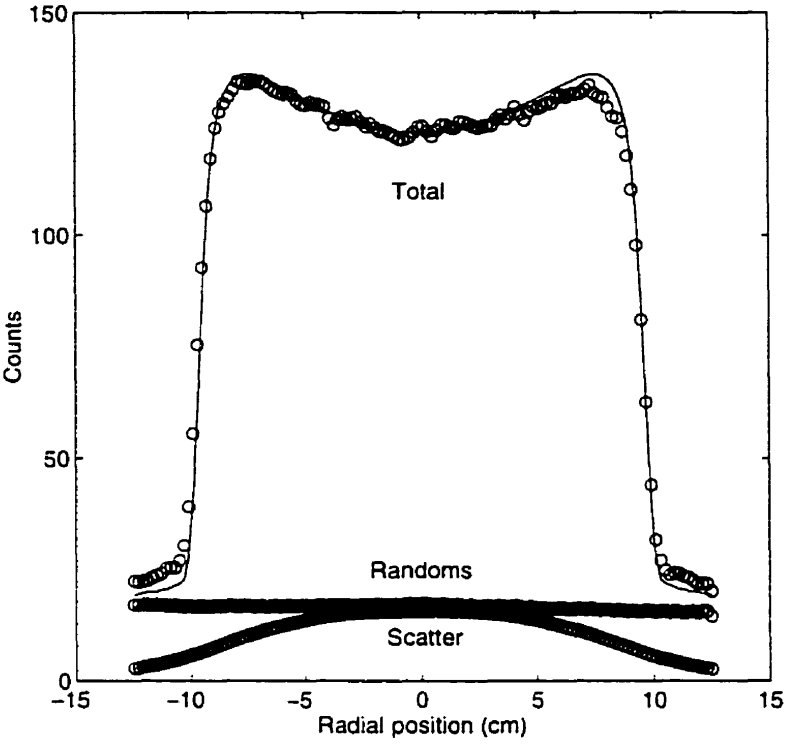

Figure 6.3: Simulated (—) and measured (o) projection components of a 20 cm flood phantom: scatter, randoms and total counts.

6.2 Flood Phantom

In order to evaluate the basic performance of the simulation methods we choose a geometrical phantom whose object characteristics are precisely known. We performed a 2 minute scan of a flood phantom on the PC2048 brain scanner. The lucite phantom (20 cm diameter × 18 cm long; 4 mm thick walls) was filled with a uniform F-18 solution at an initial concentration of 1.4 μCi/cc. Total counts in direct and cross slices alternated between (1.33 - 2.13) M with scatter fractions of (11.8 - 12.5) % and randoms fractions of (16.4 - 27.2) %. This corresponded to an imaging situation with high count rates ranging from 11 to 17.75 Kcps. Simulated projection data were then

generated from a digital phantom of the same geometry and size. Water and lucite regions were assigned with the attenuation coefficients in Table 2.2. We extracted the components of projection data in each slice. Because of the symmetrical activity distribution around the center we averaged them over all angles. A series of images were then reconstructed and analyzed with a 16 cm diameter circle placed at the center of the phantom.

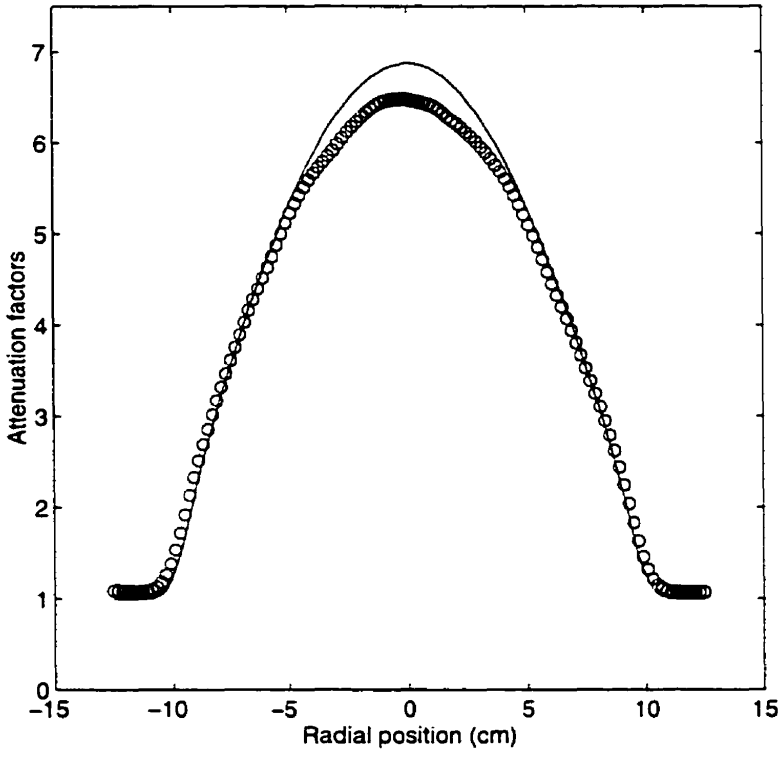

Figure 6.4: Simulated (—) and measured (o) attenuation correction factors of a 20 cm flood phantom. Notice the underestimation in the measured data due to residual scatter radiation in the transmission scans.

6.2.1 Sinogram analysis

Fig. 6.3 compares real and simulated projection data for a direct slice averaged over all angles. The ratio of simulated to measured data, when averaged across projection

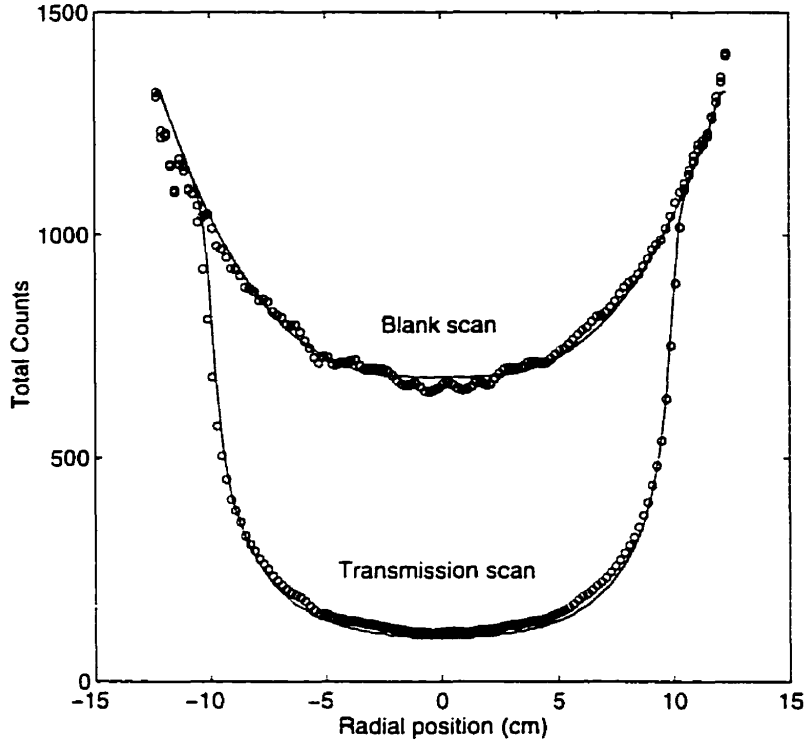

Figure 6.5: Simulated (—) and measured (o) blank and transmission data of a 20 cm uniform phantom with 14 M and 6 M total slice counts respectively.

positions, has mean of 0.974±0.072 for total counts, 1.043±0.014 for scatter and 0.997±0.035 for randoms. However Fig. 6.4 shows that the measured attenuation correction factors (ACFs) for the same slice are underestimated by 6.3 % at the center, with a mean ratio of 1.001±0.065. As discussed in section 3.1.4 this stems from scatter and randoms in transmission data, neglected in the attenuation correction method of the PC2048 scanner. Such disagreement has also been seen in a CTI-831/08 NeuroPET system [Hoffman et al., 1991] and its impact on attenuation coefficient is given below.

To emphasize this point further we also performed transmission simulation following the steps given in section 5.2.6. We used 'ideal' input data derived from the measured blank sinogram which contain some scatter among detectors. We observe

good agreement between the simulated and measured blank and transmission data in Fig. 6.5. The slightly higher counts in the middle of the real transmission scan reflects scatter inside the object.

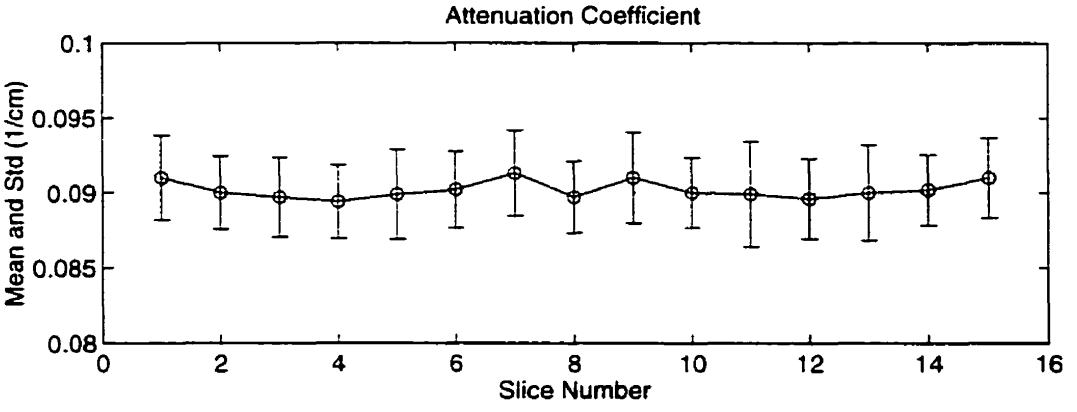

Figure 6.6: Attenuation values measured from the real transmission images of a water phantom at each slice position. Small variation across slices reflects different amounts of scatter accepted in the scan data.

6.2.2 Image analysis

Firstly we reconstruct the simulated and real attenuation data in Fig. 6.4 to verify their overall accuracy in the image space. As expected the simulation data recover the assumed narrow-beam attenuation coefficient of water (0.096 cm^{-1}). However Fig. 6.6 shows that the measured attenuation values of the real data over all slices have a mean of 0.090±0.001 cm^{-1} and a reduction of between 5-7 % relative to the simulated value. Note that the coefficient of variation (COV) data range from 2.6 % to 3.9 % with a mean of (3.0±0.4) %.

Secondly we examine emission images reconstructed under different conditions. A 6 mm Hanning filter was used as typically done in clinical studies at similar counts. Randoms were removed with the corresponding simulated and real randoms data

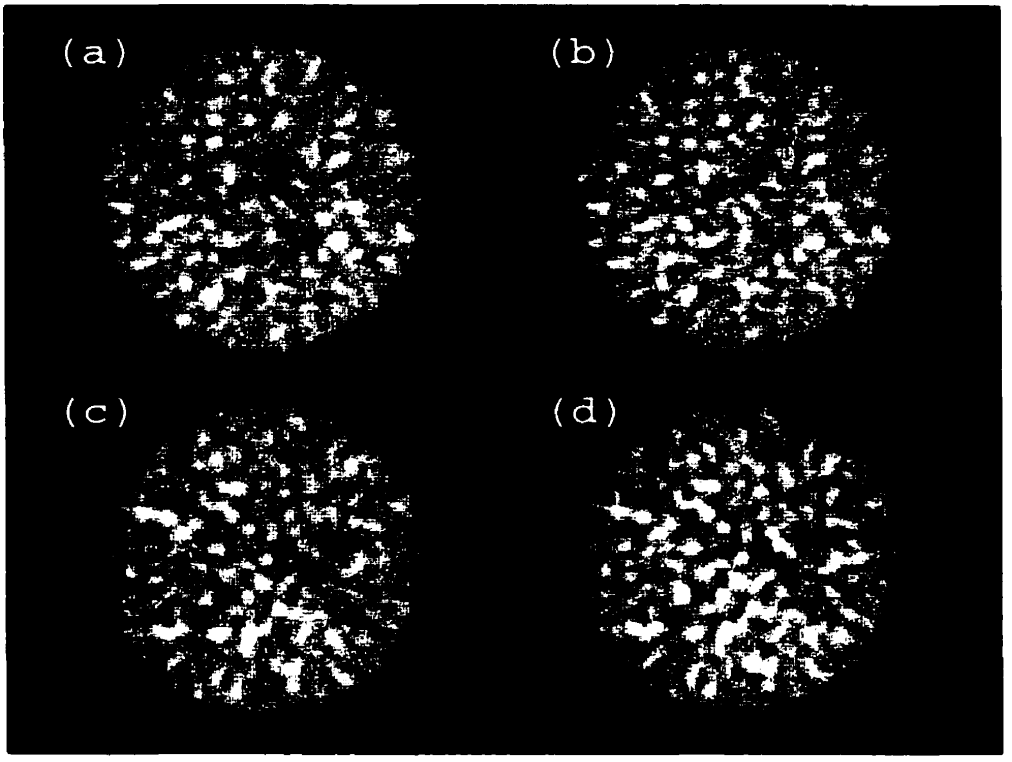

Figure 6.7: Simulated images of the flood phantom with the measured (a) and simulated (b) attenuation correction factors. Real images with the measured (c) and simulated (d) attenuation correction factors. Note the similarity in the intensity and noise structures between images in each column.

while scatter events were corrected using the deconvolution algorithm on the PC2048 scanner (section 3.1.3). To evaluate the accuracy of the scatter correction method we also reconstructed simulation data by subtracting the known simulated scatter counts. Since the scatter counts are removed 100 % we call this step 'subtraction scatter correction' below. In addition we compensated attenuation effects with the attenuation data from simulation and transmission scans respectively to assess their impact on activity values. This was done because of the difference shown in Fig. 6.4.

Fig. 6.7 shows some images reconstructed from simulated and real emission data. Fig. 6.8 plots the regional mean activity concentration and its standard deviation

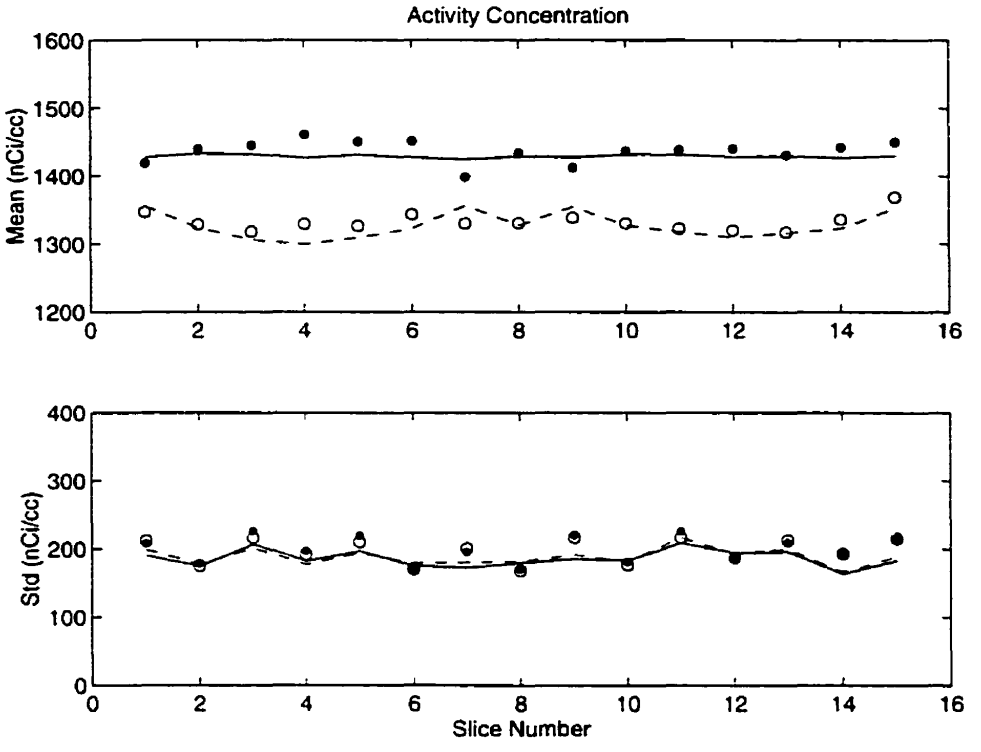

Figure 6.8: Activity values over the flood phantom: simulation (—) and real data (•) with simulated attenuation correction factors; simulation (- -) and real data (∘) with measured attenuation correction factors. The differences between the two sets of curves come from the discrepancy (Fig. 6.4) and variation (Fig. 6.6) in the attenuation data shown above.

(SD) for each slice. The activity levels vary with a COV of <1.5 % over 15 slices, while the SD data have COVs of less than 6.8 % and 9.8 % in the simulated and real images respectively. Table 6.1 summarizes the ROI values using different correction methods as described above. Comparing Sim1 and Sim2 shows that the scatter deconvolution algorithm changes the mean activity over slices by <1 % and increases the SD by <2.5 % with both the measured and simulated ACFs. Thus this method is accurate for removing scatter counts from simulations.

We compare only Sim2 and Real data in the following discussion. The simulated ACFs increase the mean activity by <7.9 % in both simulation and real data, but

Table 6.1: Regional values of the flood phantom with the measured (A1) and simulated (A2) attenuation correction factors.

Data	A1			A2			Units
	mean	SD	COV	mean	SD	COV	
Sim1	1313	185	14.1 %	1432	181	12.7 %	(nCi/cc)
Sim2	1327	188	14.2 %	1429	186	13.0 %	(nCi/cc)
Real	1332	198	14.8 %	1437	200	13.9 %	(nCi/cc)
Sim1	0.986	0.934	0.953	1.075	0.914	0.858	—
Sim2	0.996	0.950	0.960	1.073	0.939	0.878	—
Real	1.000	1.000	1.000	1.079	1.010	0.939	—

This table evaluates the effects of different scatter and attenuation correction methods and compares simulations with real data. Sim1: subtraction scatter correction (see text); Sim2: deconvolution scatter correction. Columns show the mean, SD and COV data from averages over 15 slices as indicated in Fig. 6.8. For easy comparison we normalize all other values to real data as shown in the lower part of the table. Notice the higher activity from the simulated attenuation correction. The simulated and real data agree well when using the same type of attenuation correction.

decrease the COVs by 8.5 % and 6.1 % respectively. This arises from the simulated ACFs which are noiseless in this experiment. The purely simulated images are 7.3% higher on average than the measurement with the SD values differing by -6.1%. When using the real ACFs these differences become -0.4 % and -5 % with a discrepancy of <4 % in the COV. Note that real images are somewhat noisier than simulations because of the noisy transmission scan and the additional rebinning process in the real sinogram data.

In conclusion the flood phantom experiments show accurate agreement of projection components and underestimation of real attenuation correction factors. Mean activity values over 15 slices match within 1 % with either simulated or measured

ACFs. Despite the use of uniform linear sampling in data simulation their SD values are smaller than the real ones by <7 %. Large SD variations in the image ROI data follow the zigzag pattern of the detector efficiency across slices. While this simple phantom study is valuable and easy to perform, it does not allow us to evaluate object/resolution characteristics of the simulation system. More realistic validation is necessary using phantoms based on brain anatomy.

6.3 Hoffman Brain Phantom

The 3-D Hoffman brain phantom (Data Spectrum Corp.) is a physical counterpart of the computerized 3-D brain phantom [Hoffman et al., 1991]. It is made of water-equivalent polycarbonate layers cut in the shapes of gray matter (GM), white matter (WM) and ventricles (VE). They are glued together to form individual transverse slices of the brain. The GM space is air-filled but the WM and VE areas contain 75 % and 100 % plastics respectively. Hence the relative concentration in the three compartments is 4, 1 and 0 when radioactivity is introduced. This emulates activity distribution in normal blood flow and metabolic PET imaging studies. As shown in Fig. 6.9 the assembled phantom consists of nineteen separate plates held together by removable nylon screws and inserted in a 17.5 cm height × 20 cm diameter cylinder (4 mm thick lucite). It has a mean slice thickness of 6.4 mm and a fillable volume of 1.15 liter.

After performing a transmission scan the phantom was filled with a uniform F-18 solution (slowly to reduce air bubbles) and repositioned in the scanner. Care was taken to remove large air bubbles from the phantom using a syringe. A long scan was then collected over 3.75 hours at initial activity levels GM = 1094.4 nCi/cc and WM = 273.6 nCi/cc (total activity = 1.2 mCi). This was done to provide a large

Figure 6.9: Photograph of a 3-D Hoffman brain phantom with the internal, anatomical slices removed.

number of projection counts and hence a nearly noiseless situation. It represented a low count-rates imaging condition with <5 % randoms and deadtime over 15 slices. Data were reconstructed onto 128 × 128 slices with a 3 mm Ramp filter.

MR data for the phantom were acquired on a Philips 1.5 T system. Slice thickness and position were selected carefully to avoid partial overlapping between adjacent planes. This was necessary since the phantom contains a set of discrete plates. MR images were then registered to PET scans using a landmark-based matching algorithm and segmented into GM, WM and VE structures using the technique described in section 5.1.2. We also identified plastics outside the brain volume by fitting the external contours of the cylinder on MR data. Each structure was assigned with its correct activity concentration. We used the attenuation values of water and lucite in GM and VE structures respectively. The attenuation coefficient of WM was estimated from the weighted sum of the water and lucite values in a 1:3 ratio. Fig. 6.10 shows

typical slices of the MR images and the digital models of the Hoffman phantom.

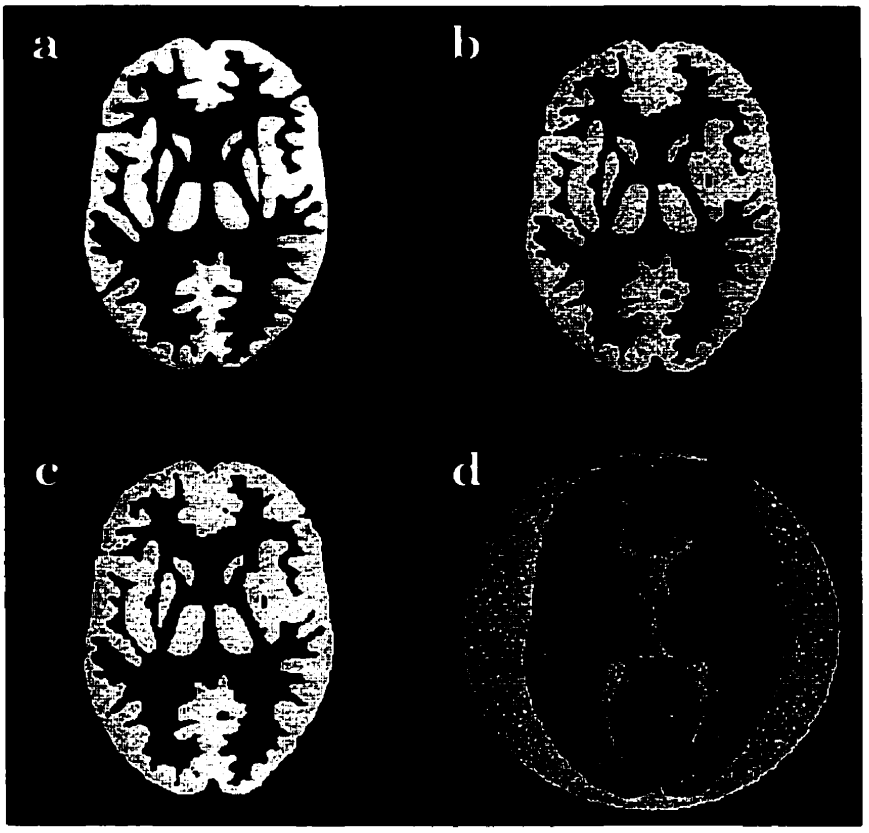

Structure ID	GM	WM	VE	Plastics
Activity ratio	4	1	0	0
Attenuation (cm^{-1})	0.096	0.106	0.110	0.110

Figure 6.10: 3-D Hoffman brain phantom (a) MR image; (b) segmented data; (c) activity distribution; (d) attenuation map. Matrix size is 256 × 256 × 1 mm^2 with the image in (d) windowed for better visualization (<15 % difference in attenuation between GM and plastics). MRI contrast comes from water filled in the phantom.

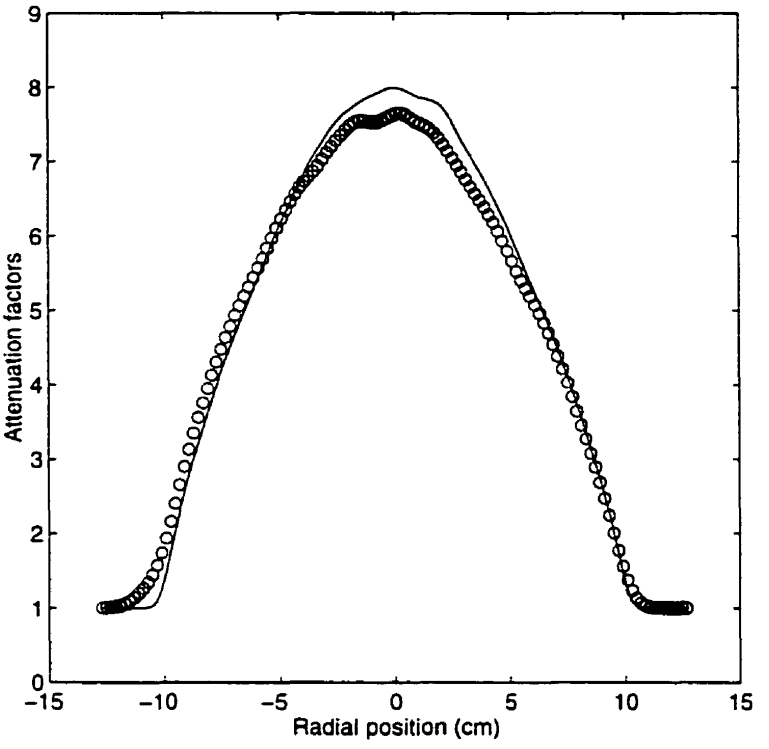

Figure 6.11: Angular averages of the measured (∘) and simulated (—) attenuation correction factors of the Hoffman brain phantom. As in Fig. 6.4 this graph gives higher values in simulation since it ignores scattered events in transmission data.

6.3.1 Sinogram analysis

Sinogram data of the Hoffman phantom were computed with the same imaging parameters as in the PET scans. Data were generated on a 256 angle × 128 × 2 mm ray grid and then mapped onto the 48 non-uniform detector positions available from the interpolation table of the scanner. Besides the slice-based efficiency and deadtime we incorporated the physical effects of attenuation, scatter and randoms. Simulated projection components were compared with their measured counterparts. We also calculated angular mean values of the attenuation data and randoms to examine their spatial distribution. This was done since the attenuation map is nearly symmetrical (Fig. 6.10) and we anticipate a weak asymmetry in randoms data as shown below.

For illustrative purposes we concentrate on one cross slice in the middle of the Hoffman brain phantom. In Fig. 6.11 the measured attenuation correction factors are slightly underestimated toward the object center because of some scatter and randoms in the blank and transmission scans (refer to section 3.1.4). Since we use the theoretical attenuation values in simulations this agrees with the results from the uniform phantom in the preceding section.

The emission data contain 30 M total projection counts with a scatter fraction of 16 % and a randoms fraction of 4 %. Fig. 6.12 plots the measured scatter counts against the simulated data along the line of unity. This graph can be fitted by $Y = 1.094 + 0.999X$ with a correlation coefficient of 0.996. It confirms that the scatter response function used in the simulation works well at realistic activity distribution. Measured data in Fig. 6.13 show that randoms are relatively uniform over the imaging field as expected for uncorrelated coincidences. Their averages over angles and radial positions have COVs of <20 %. Because both randoms and deadtime are dominated by singles rates we infer that deadtime factors behave similarly at different detector positions.

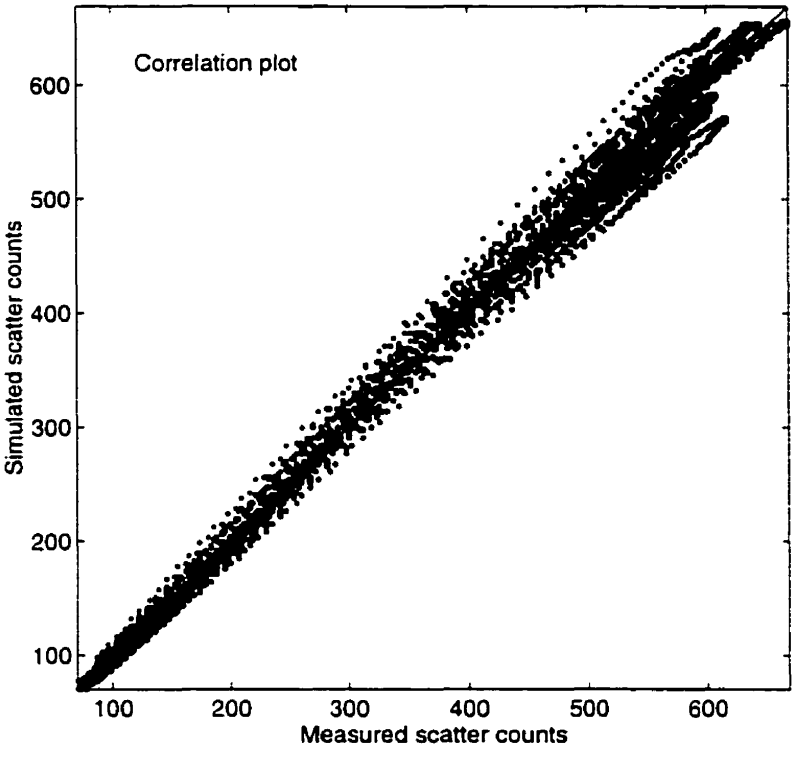

Figure 6.12: Measured versus simulated scatter counts at every projection position of every angle in one slice of the Hoffman brain phantom. Both have total scatter counts of about 6 M and a scatter fraction of 22 %.

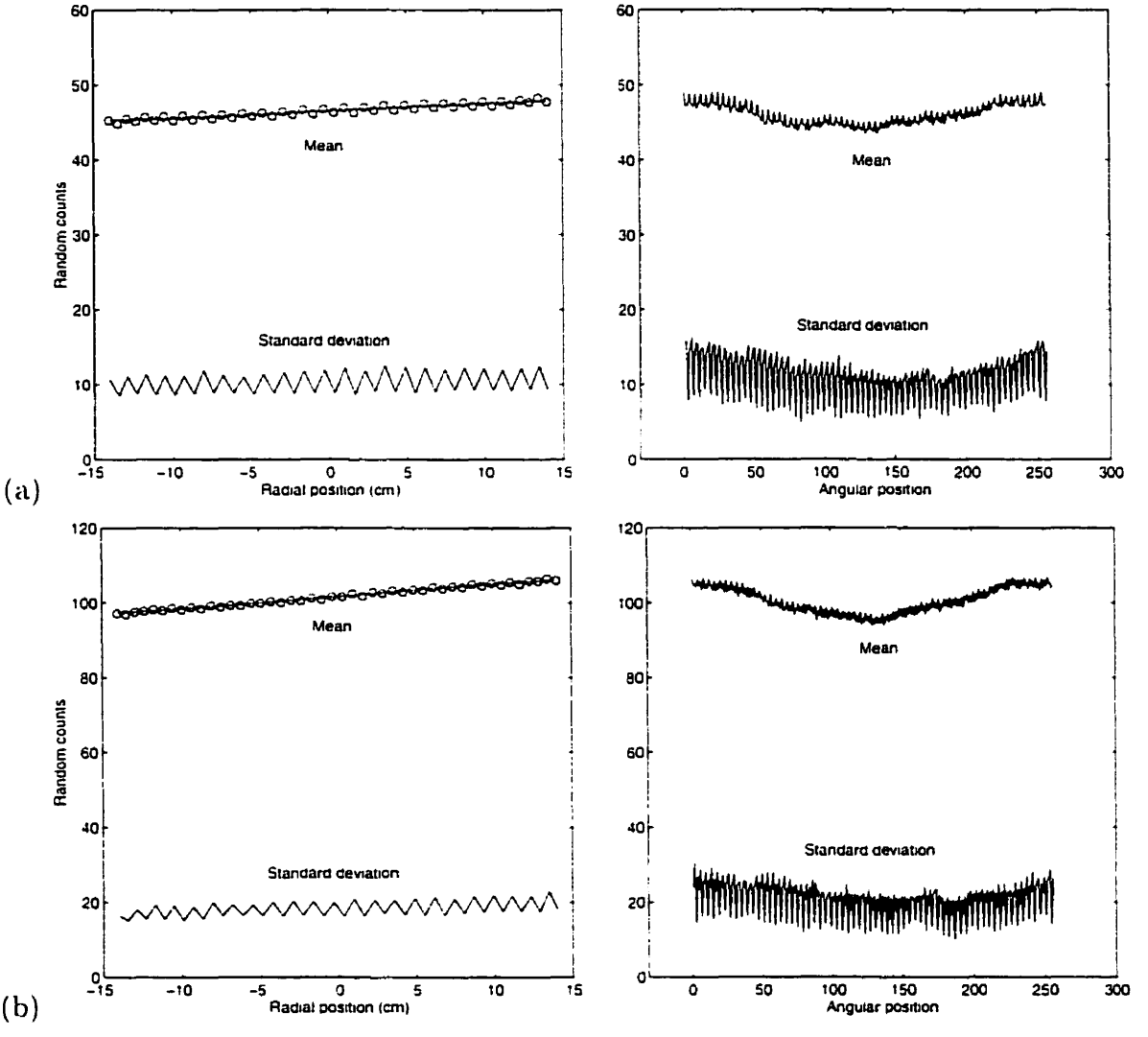

Figure 6.13: Spatial variation of the recorded randoms of the Hoffman phantom. (a) direct slice with 0.5 M total randoms and a randoms fraction of 3.5 %. (b) cross slice with 1.2 M total randoms and a randoms fraction of 4.5 %. The zigzag shapes may come from the data rebinning procedure. The slight dip on the right panel indicates a small asymmetry caused by anisotropic attenuation of singles rates.

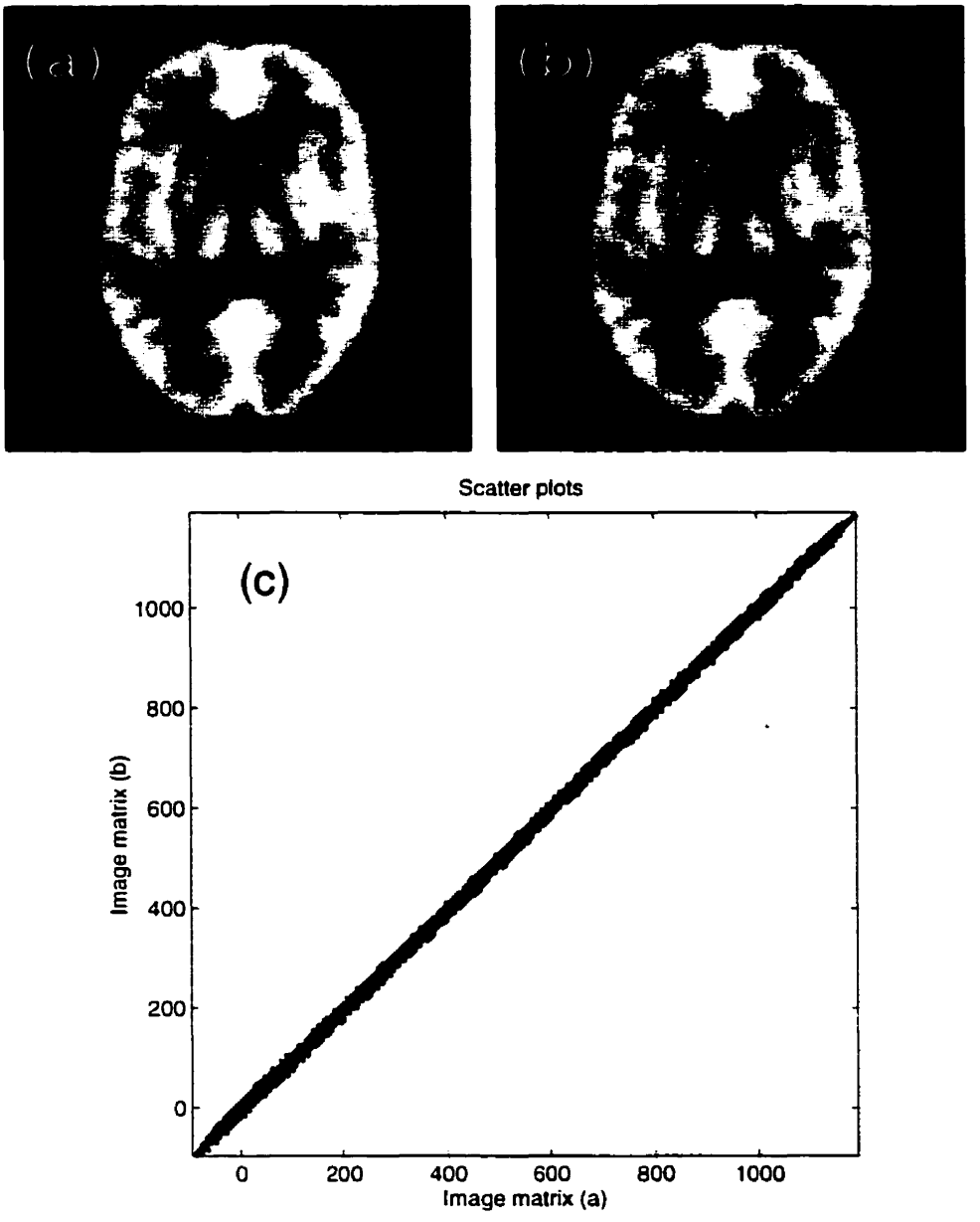

Figure 6.14: Simulated images of the Hoffman brain phantom with (a) subtraction scatter correction (see text) and (b) deconvolution scatter correction. (c) Intensity correlation plot between (a) and (b) showing a near-perfect linear fit.

6.3.2 Image analysis

In order to reveal contributions of individual components we created projection data which simulated each physical effect separately and together. In this section we wanted to investigate image resolution problems. As a result we reconstructed the total data by correcting randoms, scatter and attenuation effects with the identical terms as generated from simulations. Before analysis they were interpolated into 256 $\times$ 256 slices with 1 mm^2 pixels. We compared only images at the 6 mm intrinsic resolution since the data have a minimal amount of noise (see below).

With simulated data we first compare one of the images obtained above to that reconstructed using the scatter correction algorithm on the PC2048 scanner. As done in section 6.2.2 this procedure was repeated on this phantom to ensure the accuracy of the correction algorithm in a complex object. Fig. 6.14 shows that both images fit very well with a linear function $Y = -1.088 + 0.999X$ with a correlation coefficient of 0.9999. This proves that the simulated scatter counts are removed completely by the deconvolution method.

Fig. 6.15 shows the similarity between the simulated and measured activity distribution of the Hoffman phantom. We calculated the mean and SD in different anatomical structures using tissue maps and regional masks from MR images. We then determined their recovery coefficients (RCs) as the ratios between the measured and true activity values in the phantom. Table 6.2 compares some regional data using ROI templates in Fig. 6.16(a). Columns 2-3 (Sim1 vs Sim2) show that noisy simulation is not much different from noisefree data at this counts level. Simulated and real values in each structure differ by <8 % within the COV limits (Columns 4-5). The RCs among gray matter structures range from 0.60 to 0.86 with the lowest values in the caudate which have smallest volumes. We also observe an asymmetry of

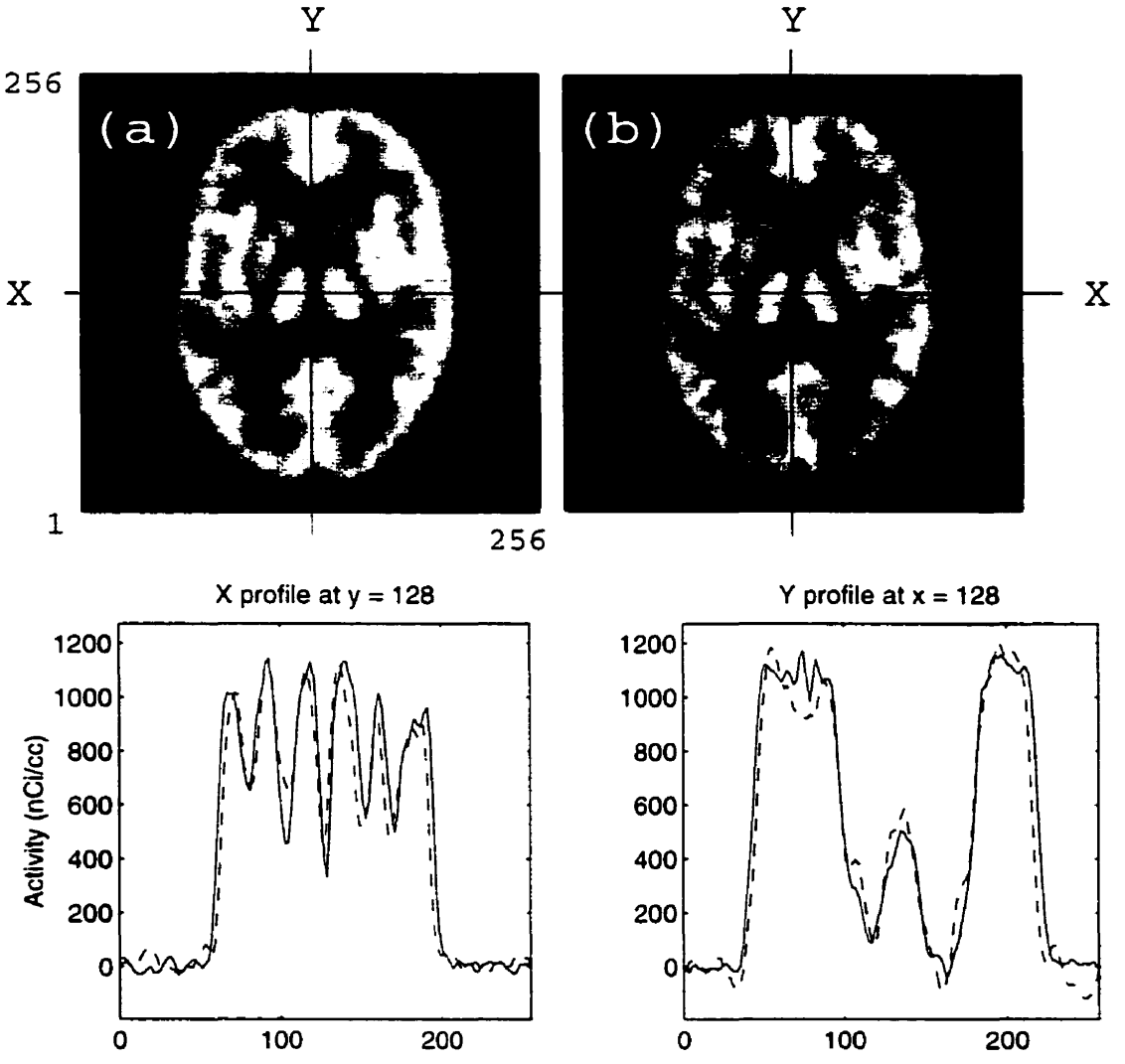

Figure 6.15: Simulated (a) and real (b) images of the Hoffman brain phantom. (c) Central activity profiles of simulated (—) and real (- -) images.

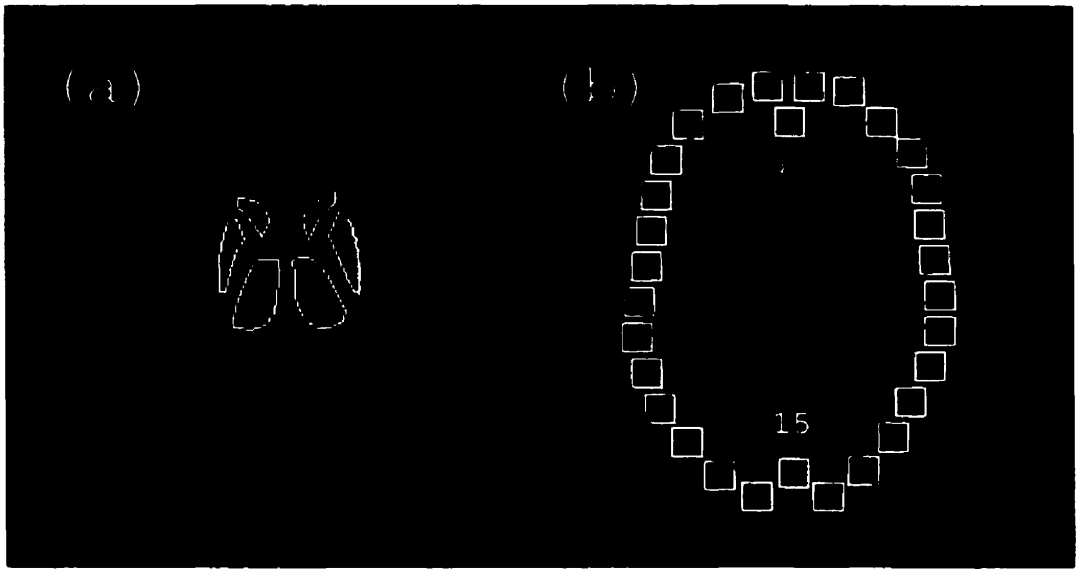

Figure 6.16: (a) Anatomical ROIs and tissue maps in the brain model. (b) 13 × 13 mm square ROIs in the cortex numbered clockwise from 1 to 30.

-12 % between the left and right putamen due mainly to their different sizes. Higher WM values reflect activity spillover from GM regions in their neighborhood.

Consider the six deep GM structures in the middle of Fig. 6.16(a). Columns 3-4 in Table 6.2 show that their RCs are reduced by 3.7-10.2 % when the axial resolution effect is included in the simulation. Overall, the values (Sim3) are 4.5 % lower than the measured data indicating that the simulated resolution is slightly larger in these regions. However the apparent activity ratios between cortical gray matter and white matter are 1.88±1.00 in simulated data versus 1.63±1.02 in real data. As discussed below they differ by 15 % although both are much smaller than the true ratio of 4. This agrees with observations in clinical PET scans of the human brain where the apparent ratios are roughly 2:1 due to partial volume distortions.

Finally we compared some activity profiles over 30 cortical ROIs in Fig. 6.16(b) whose dimensions are twice the image resolution. The geometrical templates cover the cortical ribbon as often used in clinical investigations. Fig. 6.17 shows the progressive

Table 6.2: Regional recovery coefficients (percentage) in selected brain structures of the Hoffman phantom.

Code	Sim1	Sim2	Sim3	Real	Volume (cm^3)
LC	68.7 ± 15.5	68.4 ± 16.1	63.5 ± 14.8	61.3 ± 22.0	0.793
RC	61.5 ± 18.0	61.7 ± 16.8	58.5 ± 17.5	61.2 ± 16.0	0.832
LP	75.3 ± 11.4	75.8 ± 12.6	71.5 ± 10.9	76.2 ± 10.9	1.255
RP	83.4 ± 12.3	83.2 ± 14.2	80.1 ± 13.9	85.4 ± 12.3	1.482
LT	83.9 ± 15.2	84.1 ± 16.0	77.1 ± 16.7	82.3 ± 18.6	2.711
RT	83.9 ± 16.7	84.0 ± 17.4	75.4 ± 19.7	81.4 ± 20.0	2.886
GM	84.4 ± 15.0	84.4 ± 15.3	83.0 ± 15.8	77.7 ± 25.0	69.42
WM	172 ± 39.1	172 ± 39.6	177 ± 37.6	190 ± 37.6	47.19

This table examines contributions of two resolution components and compares simulations with real data. Sim1: in-plane resolution without other physical effects and noise; Sim2: in-plane resolution with other physical effects and noise; Sim3: all physical effects with axial resolution and noise. Columns show the mean and COV using 3 mm Ramp filters. Volumes are determined from the total number of pixels in each structure displayed in Fig. 6.16(a). LC: left caudate, RC: right caudate, LP: left putamen, RP: right putamen, LT: left thalamus, RT: right thalamus. GM: cortical gray matter, WM: white matter. Data demonstrate large reduction and variability in observed regional activity with a close match between simulated and real RC and COV values.

degradation of cortical activity by the 3-D detector resolution. For instance, one can notice a partial recovery caused by activity spillover from the in-plane sampling even without including resolution effects. We observe substantial variations in the apparent activity values which reflect mostly the true activity pattern. This is not surprising since ROIs contain both gray and white structures in different proportions.

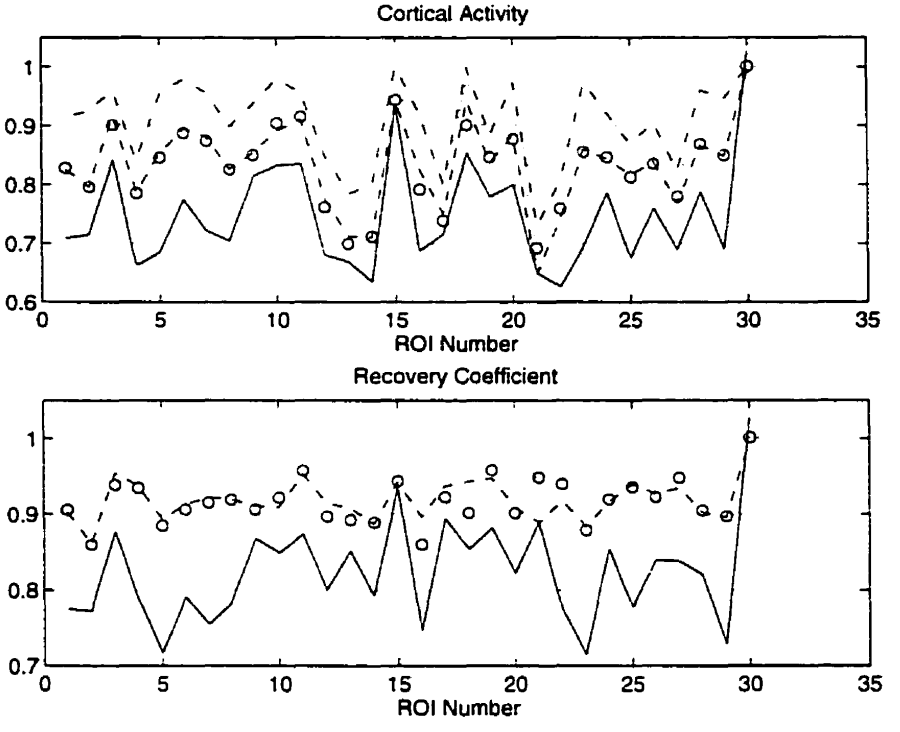

Figure 6.17: (a) Cortical profiles and (b) recovery coefficients of the simulated images with different physical effects as compared to real data of the Hoffman brain phantom. Dash-dot line: brain model; dot line: in-plane sampling; dash line: in-plane resolution; open circle: all physical effects with axial resolution; solid line: real data. ROI number runs clockwise from the top as shown in Fig. 6.16 (b) and the volume of each square ROI is 1.10 cm^3. Data are normalized to the true GM activity and regional values in the brain model respectively. Note that activity spillover from adjacent slices due to the axial resolution is not significant in the cortex. While simulations have higher magnitudes (Table 6.3) they reproduce the general shape of real data.

Table 6.3: Variability of cortical profiles and recovery coefficients in the Hoffman brain phantom.

Activity Profiles						
data	mean	SD	COV (%)	max	min	max/min
True	0.908	0.074	8.11	1.000	0.730	1.371
Sim1	0.876	0.075	8.54	0.993	0.691	1.439
Sim2	0.835	0.076	9.15	0.996	0.649	1.535
Sim3	0.833	0.072	8.69	1.001	0.692	1.447
Real	0.748	0.092	12.3	1.028	0.626	1.642
Recovery Coefficients						
Sim1	0.964	0.014	1.42	0.993	0.940	1.056
Sim2	0.919	0.027	2.94	0.996	0.859	1.159
Sim3	0.917	0.031	3.33	1.001	0.860	1.164
Real	0.823	0.068	8.30	1.028	0.715	1.437

This table describes the characteristics of the simulated and real data plotted in Fig. 6.17. True: brain model: Sim1: in-plane sampling without other physical effects and noise; Sim2: in-plane resolution with other physical effects and noise: Sim3: all physical effects with axial resolution and noise. Rows show the mean, SD and COV of each profile along with the ratio between the maximum and minimum values. Image reconstructions employ 3 mm Ramp filters. Notice the decrease in variability and the increase in recovery going from activity to RC data. Higher simulated values point to a systematic bias in resolution simulation.

Fig. 6.17 shows that the large variability in the activity profiles is reduced considerably in the RC plots as summarized in Table 6.3. The COV values of the simulated data decrease from 9.2 % to 3.3 % (Column 4) while the maximum/minimum ratios change from about 1.53 to 1.16 (Column 7). In addition the recovery in both simulated and real values is increased by 10 % after normalization to the regional data. Compared to the measurement the mean RCs in simulations are 11.4 % larger although the COV and the ratio are much smaller. This is consistent with the trend observed in Table 6.2 where the simulated RC in the cortical gray matter is 6.8 % higher than the real value. Both imply that the simulated resolution is somewhat smaller in cortical regions as compared to that in the scanner.

We can draw following conclusions from the Hoffman phantom experiments. (1) Our results demonstrate the validity of scatter and randoms models in projection data simulation and a small (<5 %) discrepancy in measured attenuation correction factors. (2) Simulations reproduce the activity distribution of the phantom scan and reveal resolution as the dominant sources of image bias. With a slight difference both simulated and measured data show that regional values among deep GM structures are underestimated by (14 - 40) % at the 6 mm intrinsic resolution. Cortical profiles demonstrate large variabilities in the simulated and real RCs having means of 0.92 ± 0.03 and 0.82 ± 0.07 respectively. Large variations in RCs prove the importance of ROI selection in the basal ganglia and cortex. Data presented here allow one to estimate or minimize potential errors in selected anatomical regions. The differences observed in this experiment suggest that the simulated resolution is lower toward the center and higher toward the edge of the imaging field.

6.4 Skull Brain Phantom

In the previous section we have used the 3-D Hoffman brain phantom which models radioactivity patterns of cerebral blood flow and metabolism. Because of the discrete nature of the phantom and the fact that its physical slice thickness matches that of the PET image planes, it is not entirely adequate to evaluate activity spillover between adjacent slices and axial resolution components. This problem becomes more important in human brain scans where activity distribution among structures is irregular and continuous along the axial direction.

In order to validate simulations in imaging situations of neuroreceptor studies we used a 3-D brain phantom of the human basal ganglia. This phantom was constructed according to structural contours from digitized brain slices to estimate partial volume distortions in small structures [Rousset et al., 1996]. It consisted of plastic cavities to represent separate compartments of the striatum and ventricles, enclosed in a main chamber and surrounded by a human skull. Because of some leakage in the left hemisphere of the basal ganglia (BG) only the right side was considered in the experiment. This does not prevent us from obtaining valuable results as long as we have a realistic radioactivity distribution.

A transmission scan was first performed on the PC2048 scanner after all compartments were filled with water. A uniform F-18 solution was then used to fill the regions of caudate nuclei (CN), putamen (PU) and globus pallidus (GP) at a concentration of 16.5 μCi/cc and a lower activity of 4.3 μCi/cc in the main cavity (BKG). Samples were taken from the radioactivity pools and measured in a well counter to determine the true isotope concentrations. This provided a static activity distribution with a ratio of 3.8 between them. A 90 minute scan was acquired to have high projection counts in each image plane with moderate randoms and deadtime contributions.

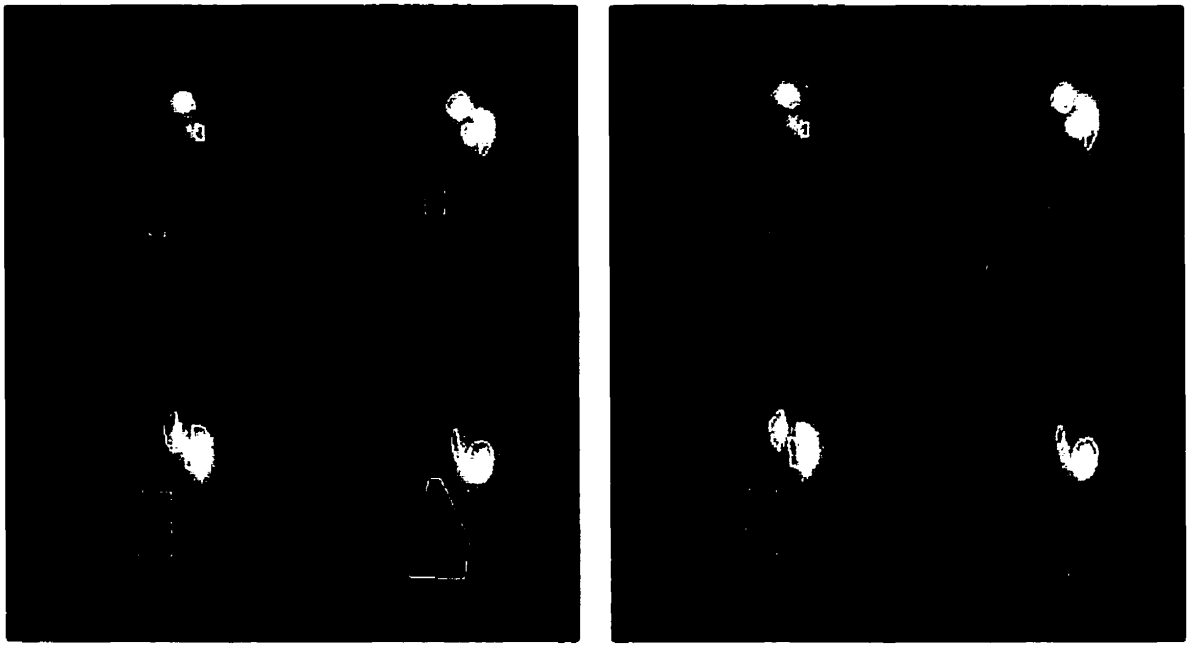

(a) (b)

Figure 6.18: Simulated (a) and real (b) images of the skull phantom with about 5 M total counts and a 6 mm Hanning filter. Irregular ROIs are created from correlated MR slices and overlaid on PET images.

MR data of the phantom were collected on a General Electric 1.5 T system; the BG structures being filled with copper sulfate solution to increase the contrast. MR and PET images were then registered and both displayed separate chambers of the striatal and ventricular structures. After being resampled into 2 mm slices the MR images were segmented into unique anatomical components. While CN, PU and GP were delineated manually, BKG and VE were identified automatically as described in section 5.1.2. Each component was then assigned the true activity values to obtain the 3-D brain model. Because of the absence of skull bone in the MR data, we created attenuation maps from the transmission PET images which were already co-registered with the resampled MRI volume. The attenuation value of water (0.096 cm^{-1}) was given to all voxels within the external boundaries of the phantom.

The simulated data of this phantom were generated such that the total counts equal the measured counts in each slice. Fig. 6.18 compares the images reconstructed to 8 mm resolution. The anatomical templates for BG regions were drawn within each structure on four MR slices located at the same levels as PET scans. Arbitrary ROIs were created to cover a large region in the background, away from the ventricles. We then determined RC data from the measured regional concentration in each compartment. Note that volumes of small ROIs vary from 0.338 to 1.872 cm^3 with the large ones between 3.913 and 10.18 cm^3. Table 6.4 shows that real and simulated activity values in BG structures are underestimated by more than 22 % with their respective upper bounds of 55 % and 50 %. Both show large and spatially variant errors even though these regions have the same activity levels in the phantom. This comes mostly from differences in the object size relative to the 3-D image resolution and some spillover effects among the BG compartments.

When compared to the real data the simulated RC values in most structures agree better than in the Hoffman brain phantom but worse in others. For example, the discrepancy in CN changes from <2 % in slices 1-2 to -17 % in slices 3-4. The values in PU are overestimated by <6.8 % in slices 1-2 but underestimated by <9.9 % in slices 3-4. The bias in GP is -4.6 % in slice 2 with the largest bias of 22.8 % in slice 3. In addition the BKG values are 10 % higher in some instances. The large fluctuations observed here suggest some systematic differences between simulations and scan data. Besides the resolution mismatch shown in the last section, there are potential geometrical errors in the segmented BG structures of the skull phantom. As Fig. 6.2 shows both poor resolution (i.e. larger FWHM) and smaller object size can lead to lower RC or vise versa. In other words, a higher RC due to better resolution would decrease if the object is smaller. As discussed below this additional problem

presents new challenges in this type of validation study. We conclude that the results from the skull phantom show reasonably good agreement with the experimental data in striatal structures.

Table 6.4: Simulated and real recovery coefficients in the skull phantom.

Slice	ID	CN	PU	GP	BKG
1	Volume (cm^3)	0.715	0.338	—	4.927
	Simulated	0.708	0.575	—	1.064
	Observed	0.695	0.553	—	0.969
	Bias (%)	2.02	4.04	—	9.73
2	Volume (cm^3)	1.04	1.04	0.371	3.913
	Simulated	0.716	0.740	0.721	1.070
	Observed	0.726	0.693	0.756	0.971
	Bias (%)	-1.42	6.82	-4.60	10.16
3	Volume (cm^3)	0.878	1.69	0.631	4.758
	Simulated	0.557	0.770	0.722	1.054
	Observed	0.671	0.778	0.588	1.014
	Bias (%)	-17.01	-0.965	22.86	3.93
4	Volume (cm^3)	0.631	1.872	—	10.18
	Simulated	0.496	0.579	—	1.036
	Observed	0.594	0.643	—	1.020
	Bias (%)	-16.45	-9.88	—	1.50

Data are from the regional activity values in caudate nuclei, putamen, globus pallidus and background, over four contiguous PET slices at 6.5 mm thickness and 8 mm image resolution. It also gives the volume of each ROI and the bias calculated by $(Simulated - Observed) \times 100/Observed$.

6.5 Discussion

We have evaluated the performance of the simulation programs under imaging situations similar to those found in clinical scans. This has been done by comparing both projection and image data.

6.5.1 Projection data comparison

Projection data and its components have been compared with a uniform phantom and a Hoffman brain phantom. Simulated and measured total projection data of the uniform cylinder match with an accuracy of a few percent as shown in Fig. 6.3 and Fig. 6.5. This ensures accurate simulation of count statistics in each projection and the resultant emission and transmission images.

We have seen small spatial variations in the measured randoms distributions which justify the use of uniform randoms and deadtime models in direct and cross slices. Scatter data from the simulations agree accurately with those estimated from the phantom studies. Analyses confirm that the simulated scatter counts in each slice are corrected accurately by the deconvolution algorithm in the scanner (Table 6.1 and Fig. 6.14). Attenuation data demonstrate the presence of scatter and randoms in real transmission measurements. The solution to this problem is to estimate and correct them in the same manner as in emission scans. A simple approach could be to model their effects in transmission simulations by using the measured attenuation coefficient.

6.5.2 Errors in resolution modeling

Resolution simulations have been evaluated by regional analysis of image data. We have demonstrated the accuracy of the simulated 3-D PSF with sphere phantom data.

This is expected since the objects are located midway between the center and the edge of the imaging field. Comparing the simulated to measured data the regional activity values in the Hoffman phantom are underestimated in deep gray matter structures but overestimated in cortical structures. This discrepancy occurs because we use a 6 mm FWHM 3-D Gaussian to model the PSF of the tomograph. As shown in Fig. 4.2 the actual resolution drops below the mean FWHM value toward the center but rise above it close to the periphery of the imaging field.

6.5.3 3-D image registration and segmentation

We have also used MR and PET data of a human skull phantom to test the accuracy of resolution simulation. We observe some additional differences between the simulated and real activity values. Being unevenly distributed these differences do not correlate with ROI size and may result from many sources. The first one is the mismatch between the simulated and actual resolution discussed above. The second one is the uncertainty in the internal landmark-based MR-PET image registration algorithm. Since the skull phantom does not contain many anatomical features we can expect a large error in this step. The third and more serious one is the error in structural delineation of BG compartments. In the current experiment we segmented them manually by drawing anatomical boundaries of each structure over a set of MR slices covering the entire BG region. This is prone to error since it is difficult to outline the structure continuously in 3-D.

Regional data from simulations demonstrate the underestimation of gray matter activity and overestimation of white matter activity with much smaller apparent ratios between them. Additionally we see large variability in regional activity values due to different object sizes and varying amounts of spillover or dilution between neighboring

structures. These observations are consistent with measurements from the phantom scans and reflect image distortions caused by partial volume effects. This problem will become worse in clinical PET studies where image resolution is lower than the intrinsic resolution. Real images and regional data have larger variances because of the noise propagation from the measured attenuation correction.

6.6 Summary

In this chapter we have validated simulation methods of projection data and their randoms, scatter, attenuation and resolution components. Phantom experiments show generally good agreement between simulated and measured data. However this work suggests that it is necessary to incorporate a spatially variant 3-D PSF and model scatter rates in the transmission scan. A more accurate digital brain phantom is also needed to tune and evaluate the simulation algorithms. Nevertheless the results presented here have laid a solid foundation for many practical applications described in the next chapter.

Chapter 7

Applications in Functional Neuroimaging

We have implemented and validated a PET simulator (PETSIM) including both object and scanner specific factors. Correlated functional and structural images are used to create a realistic representation of activity and attenuation distributions in many normal and abnormal imaging protocols. We then generate highly realistic projection data by incorporating key features of tomographic data acquisition. These simulations have many distinct advantages that allow us to evaluate and improve regional activity quantification in PET studies. In this chapter we describe some principal applications and discuss practical implications in the context of quantitative brain imaging.

The PETSIM system has been used widely as parts of several collaborative projects at the MNI and at the Johns Hopkins University. These projects include (1) estimation of regional bias and variance in dynamic image studies; (2) *in vivo* correction of partial volume effects using correlated anatomical images; (3) validation of multimodality image registration algorithms. Section 1 investigates the impact of partial volume effects on quantitative measurement of radiotracer uptake. We will concen-

trate on section 2 in which we describe a new method for partial volume correction and evaluate its accuracy using MR and PET data acquired from a 3-D brain phantom. We then summarize its use in image registration problems in section 3 along with a brief discussion of other related applications in section 4.

7.1 Estimation of Regional Bias and Variance

The accuracy and precision of radioactivity measurement depend on the optimal correction of signal distortion in data acquisition. Using PETSIM we can validate the accuracy of each distortion correction and make a quantitative assessment of their relative merits in the sinogram and image spaces. Besides looking into the signal/noise problems one can also examine the interaction between scatter and attenuation correction methods. This has been investigated briefly in the previous chapter as part of the validation experiments. It also allows objective evaluation of regional distortions from image reconstruction algorithms. In the following section we address this second question which has direct clinical relevance.

The practical image resolution in PET is much lower than the intrinsic limit of 4-5 mm imposed by the tomograph geometry and positron range effects. Coarser filters are used to reduce statistical noise at the expense of poorer resolution (typically between 8 and 20 mm FWHM depending on the application). This will decrease variance in regional values but increase bias at the same time. It is therefore necessary to characterize the magnitudes and dependence of these variables on reconstruction parameters. One can then select a proper method to balance the bias and variance as desired for a particular combination of tracer, scanner and acquisition protocol.

7.1.1 Dependence on reconstruction filters

We used the Hoffman brain phantom to study the effects of different filters and counting statistics. Simulations were necessary in order to assess the two problems separately with both noisy and noiseless data. This was done following the simulation steps as described in section 6.3.1. Simulated data were generated with 300 K, 600 K and 1 M total slice counts. With a scatter fraction of 16 % their randoms fractions equal 10 %, 16 % and 25 % respectively. These parameters covered the range typically collected in clinical PET scans. We then reconstructed images using Hanning/Ramp filters with FWHM varying from 3-20 mm. Since the ROIs were exactly known in the phantom we computed the regional activity mean and SD using the tissue maps obtained from MR data.

Figure 7.1: Simulated images of the Hoffman brain phantom with 300 K (a, b, c) and 1 M (d, e. f) total projection counts. Data are reconstructed with 6, 10 and 15 mm Hanning filters respectively. Notice the dependence of image quality on different noise levels and resolutions.

(a) Noiseless Data

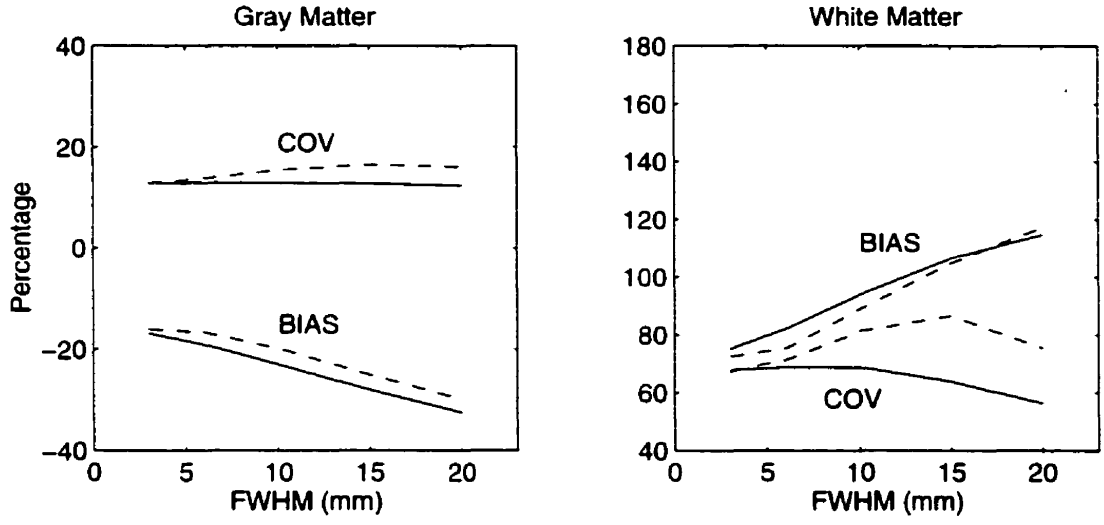

(b) Noisy Data

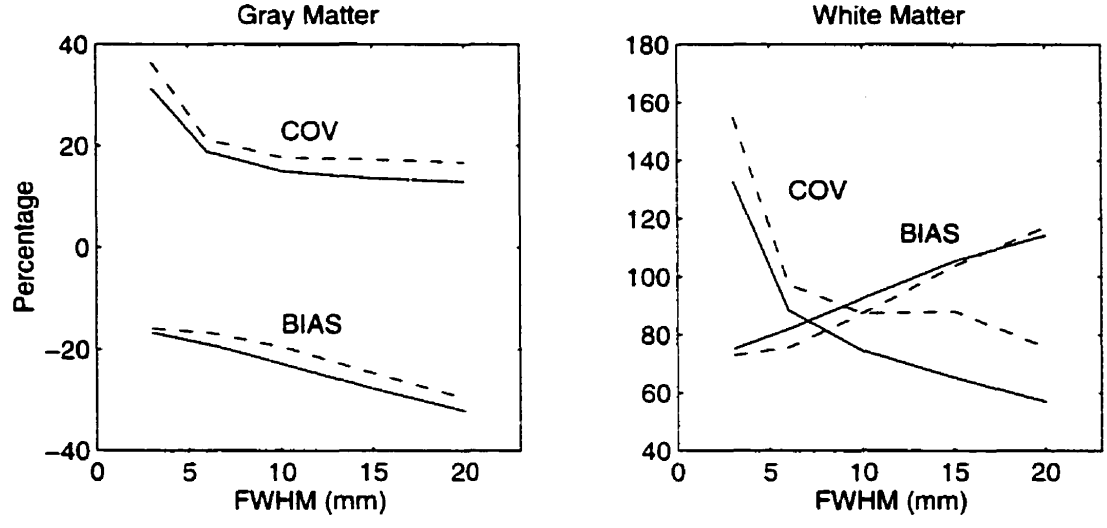

Figure 7.2: Relative bias and coefficient of variation in gray matter and white matter vs the reconstruction filter width. Data are from the simulated PET images of the Hoffman brain phantom with Hanning (—) and Ramp (- -) filters and 300 K total projection counts. Note that COV are relatively flat in the noiseless data. Although a smaller filter gives less bias, a wider filter (>5 mm) must still be used to decrease the large COV in the noisy data. One can see steady decrease/increase in the estimated activity values in gray/white regions due to partial volume mixing.

Table 7.1: Regional bias and standard deviation of the Hoffman phantom

Variable		Gray Matter		White Matter		Noise
Hann	COV	12.8	12.4	67.7	56.3	N
	(%)	31.4	12.9	133.	56.9	Y
	BIAS	-16.9	-32.5	75.1	114.7	N
	(%)	-16.7	-32.2	75.1	114.2	Y
Ramp	COV	12.8	16.1	67.3	75.3	N
	(%)	36.6	16.7	155.	75.7	Y
	BIAS	-16.1	-30.0	72.3	117.2	N
	(%)	-16.0	-29.7	72.9	117.1	Y
FWHM		3	20	3	20	

A summary of percentage quantification errors in Fig. 7.2 at two extreme filter widths: 3 and 20 mm FWHM reconstruction filters without and with Poisson noise added.

Fig. 7.1 shows the typical simulated images with different projection counts and Hanning filter widths. We evaluate them by the percentage bias (BIAS) and the coefficient of variation (COV) with respect to the true activity in each structure. Fig. 7.2 compares BIAS and COV in gray matter (GM) and white matter (WM) as a function of FWHM for two reconstruction filters. It demonstrates partial volume effects in the absence and presence of counting noise. Some of the regional data are summarized in Table 7.1.

Both plots show that BIAS values change from -16.7 % to -32.2 % for GM, and 75.1 % to 114.2 % for WM over the 3-20 mm width of Hanning filters. Without noise, Fig. 7.2(a) shows small changes in COV of 12.8 % to 12.4 % and 67.7 % to 56.3 % which reflect variations due to the image resolution alone. With noise, the COV decreases more quickly from 31.4 % to 12.9 % for GM and 133 % to 56.9 % for WM as shown in Fig. 7.2(b). As expected, we observe that the Hanning filter gives

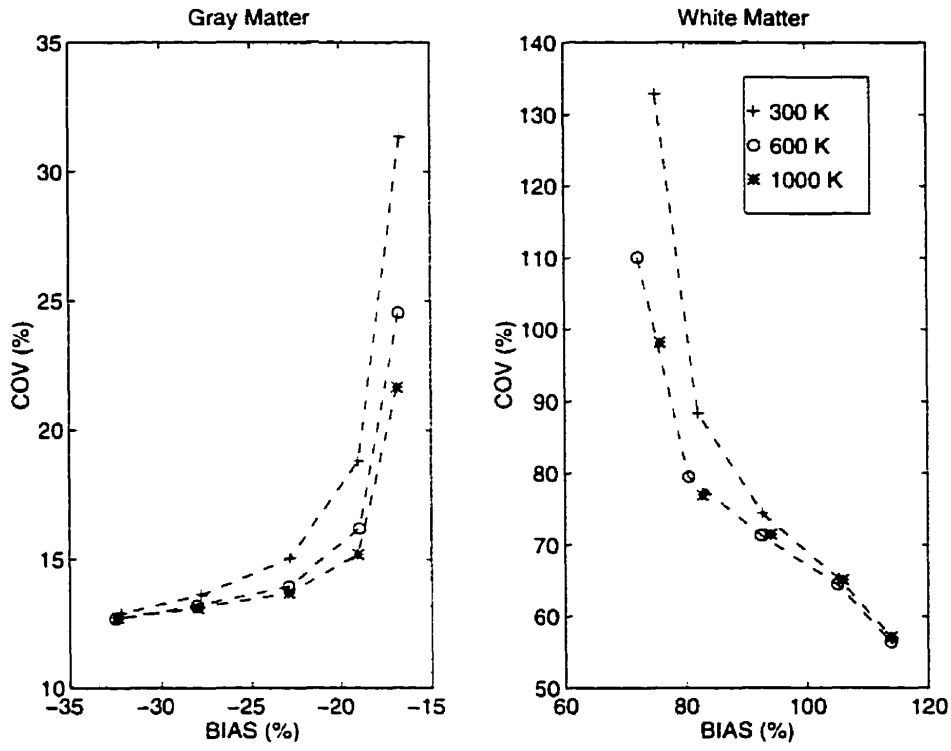

Figure 7.3: Relative bias vs COV in gray matter and white matter at three different total counts with noise added. Data are from the simulated PET images of the Hoffman brain phantom with 3-20 mm Hanning filters. The filter widths corresponding to the five data points are given below each panel. As the FWHM increases, bias becomes larger while COV decreases. Note that COV drops at higher counts due to the decreased statistical noise.

smaller variances and slightly larger biases as compared to the Ramp filter. Statistical effects are essentially eliminated at FWHM $\geq$ 15 mm where the COVs of noisy data and noisefree data become equal.

7.1.2 Accuracy verses precision

Further analysis is done to characterize the relationship between accuracy (BIAS) and precision (COV) as a function of image resolution and noise levels (Fig. 7.3). It can be seen that COV decreases with the increasing projection counts, while BIAS

remains nearly constant for a given filter width. This decrease is relatively moderate within clinical count ranges of 300 K to 1 M. At much higher counts the COV values approach the noiseless data shown earlier. Data in gray matter show that the increase in COV is much faster than the reduction in BIAS toward higher resolution (smaller FWHM); while the reduction in COV is much slower than the increase in BIAS toward lower resolution (larger FWHM). Depending on the situation both cases may give rise to a lower SNR and must be avoided in protocol design. Instead one always selects optimal parameters to achieve desired BIAS and COV. For example clinical CBF (300 K) and FDG (1 M) studies can be reconstructed with 10/6 mm FWHM respectively to have a comparable COV of 15/15.2 % and BIAS of -22.9/19.1 % (SNR = 5.14/5.32). White matter regions show a similar trend but with different values.

In a related work we observed similar behavior with other filter types like the Hamming and Parzen [Ma et al., 1995]. We find big reductions in both bias and variance within smaller circles as they approach the filter width. In general both values depend critically on the location and choice of ROI templates. One can repeat the analysis for any anatomical structures using ROIs of varying shapes and sizes. While actual numbers may differ we expect to reveal the same general relationship seen above. Based on the validation data in the last chapter we would obtain equivalent results from the real phantom. However the simulation is faster, more flexible and easier to use. For instance one can divide the simulations into arbitrarily defined ROIs with different activity distributions.

We conclude that PETSIM is useful in predicting the accuracy and precision in PET image reconstruction. The results demonstrate that for a given activity distribution, the regional bias is determined by resolution effects while the variance is dominated by counting noise. Although these issues are well-known the study

yields quantitative estimates of potential errors. This can help optimize the image reconstruction and analysis strategy according to the objectives of PET investigations.

7.2 Correction of 3-D Partial Volume Effects

A primary source of inaccuracy in PET is due to the 3-D partial volume effects (PVE) resulting from limited image resolution and inadequate axial sampling. Regions with identical activity values may have different apparent concentrations depending on their locality and image/ROI characteristics. Correcting the 3-D PVE is essential for accurate differentiation of cerebral function. This is especially true when comparing brain images that have large anatomical differences either because of atrophy or pathological disruptions.

Simulation methods using anatomical images have been proposed to remove the PVE on a pixel basis. Initially they were applied to myocardium by deriving an organ model from a human heart phantom [Herrero et al., 1988] and extended to gray matter structures using a set of segmented MR images [Muller-Gartner et al., 1992]. In this early work, activity distribution from white matter regions was estimated and subtracted from the PET images to obtain the activity distribution originating from gray matter. The resulting images were then divided by the recovery coefficient maps generated by convolving the binary tissue mask with a 3-D PSF. However these methods require some unrealistic assumption, particularly the measurement of activity values in some structures free of any PVE. This is not applicable to imaging protocols like receptor binding and clinical images that include small pathological abnormalities.

Since in practice the tracer concentrations are estimated using ROI templates we have developed a correction method on a regional basis [Rousset et al., 1996]. This

method is independent of tracer activity levels and kinetic models in PET studies. It is based on a prior model of tracer biodistribution and tomographic imaging characteristics. We derive this information from registered and segmented MR/CT data. It works by estimating the magnitude of pure recovery and activity spillover between different functional entities in a given set of ROIs. In the following we describe the algorithm and validate its performance with a 3-D brain phantom.

7.2.1 Principle of the correction method

Our method is derived directly from the linearity property inherent in tomographic imaging systems. Each voxel in a PET image is the weighted sum of the 3-D system PSF convolved with the true activity distribution. Assume there are N different tissues contributing to the measurement each with a homogeneous uptake. The apparent activity in a specific region is given by

$$t_i = \sum_{j=1}^{N} \omega_{ij} T_j \tag{7.1}$$

where vectors t_i and T_j are the observed and true activity values in each tissue. ω_{ij} denote the transfer coefficients which express the fraction of activity in the jth tissue integrated in the ith ROI. Each element is calculated by

$$\omega_{ij} = \frac{1}{M_i} \sum_{k=1}^{M_i} RSF_j \tag{7.2}$$

where M_i is the total number of pixels in the ith ROI and $RSF_j = \sum_l X_j h_{lj}$ is the regional spread function. This is basically a convolution between the domain of the structure (X_j) and the PSF of the scanner (h_{lj}). In general X_j refers to the probability of tracer uptake at each voxel with a value of 0 or 1. Collectively ω_{ij} depend on geometrical relationships between the structures involved and may vary substantially with the 3-D image resolution and ROIs used. Considering a system

with four regions one can write equation 7.1 in a matrix form,

$$\begin{bmatrix} t_1 \\ t_2 \\ t_3 \\ t_4 \end{bmatrix} = \begin{bmatrix} \omega_{11} & \omega_{12} & \omega_{13} & \omega_{14} \\ \omega_{21} & \omega_{22} & \omega_{23} & \omega_{24} \\ \omega_{31} & \omega_{32} & \omega_{33} & \omega_{34} \\ \omega_{41} & \omega_{42} & \omega_{43} & \omega_{44} \end{bmatrix} \begin{bmatrix} T_1 \\ T_2 \\ T_3 \\ T_4 \end{bmatrix} \tag{7.3}$$

While the diagonal terms ω_{ii} represent the recovery coefficient (measured to true activity ratio in the absence of surrounding activity), the other ω_{ij} refer to the spillover fraction between each pair of structures. Note that the elements depend on activity distribution but are independent of its concentration in each tissue component. If this matrix is known, one can restore the true activity in each structure by simply inverting 7.3. The corrected value and variance are then given by

$$T_i = \sum_{j=1}^{N} \omega'_{ij} t_j \qquad V_i = \sum_{j=1}^{N} \omega'^{2}_{ij} v_j \tag{7.4}$$

where ω' is the inverse matrix of ω. t_j and v_j are the mean and variance of the ROI values estimated from any images. In practice it is impossible to determine this matrix because of the compounding distortions in image acquisition. We can solve the problem only by accurate simulation of radiotracer distribution and 3-D tomograph resolution.

The key to this method is the calculation of ω_{ij} from the brain model and PET-SIM. As before, we create a 3-D brain model from tissue classification and structure delineation after MRI-PET registration. The simulated images of each structure are generated separately assuming unit activity and accounting only for 3-D resolution effects and without adding noise. This gives us the RSF for the structure, represented as a volume. Note that the 'structure' need not be made up of contiguous voxels so long as all voxels in the structure can be assumed to have the same radioactivity

concentration. Each element of the transfer matrix is then extracted by overlaying ROI sets on each RSF. We obtain and analyze images with reconstruction parameters and regional templates identical to those used in real PET scans. Because the RSF depends solely on structure geometry and image resolution, the transfer matrix is only calculated once and used across the time-activity curves (TACs).

This approach allows partial volume correction in all tissue TACs simultaneously. There is no need to estimate background activity as in other methods. Since the correction in one region depends on noisy data in all structures one must evaluate noise propagation issues. This is achieved by computing both the mean and variance of the corrected values. We determine the precision by a noise magnification factor defined as the ratio of COV before and after PVE correction.

7.2.2 Experimental validation

The accuracy and precision of the PVE correction method were evaluated with the human skull phantom described in Chapter 6. This was done in two different experiments described below.

Static tracer distribution:

In order to examine activity recovery and noise propagation we first performed a single isotope experiment. The phantom was filled with F-18 solutions at a concentration of 16.5 μCi/cc in the basal ganglia structures and 4.3 μCi/cc in the main chamber (BKG). To provide different counting statistics, a set of dynamic scans was acquired on the PC2048 camera to obtain 27 frames over 90 min using a typical F-Dopa protocol. Images were reconstructed with a 6 mm Hanning filter after decay correction and standard preprocessing routines. We used the same ROI templates and the segmented MR images created in section 6.4 to extract TACs in each structure and

perform PVE correction.

The transfer matrix was then computed over four slices. We have in this case a 3 tissue system with caudate, putamen and main cavity; or 4 when the globus pallidus is included. Table 7.2 lists typical values for transfer coefficients as illustrated by the RSF images and ROI templates given in Fig. 7.4. It shows that among the striatal structures, only part of the apparent activity comes from the region itself with small portions being contributed by the nearest neighboring structures. In all cases the most significant contaminations in the striatum come from the large background. Note that the sum of all transfer coefficients for a given ROI is less than 1 due to dilution from regions without radioactivity (e.g. ventricles). True activity values were calculated by applying its inverse to the measured regional data in each slice.

Table 7.2: Regional transfer coefficients of the skull phantom

Forward matrix					Inverse matrix				
	CN	PU	GP	BKG	cn	pu	gp	bkg	
cn	0.672	0.018	0.008	0.233	1.491	-0.053	-0.011	-0.329	CN
pu	0.037	0.483	0.112	0.358	-0.105	2.131	-0.389	-0.645	PU
gp	0.022	0.070	0.611	0.258	-0.040	-0.244	1.682	-0.341	GP
bkg	0.000	0.000	0.000	0.989	0.000	0.000	0.000	1.011	BKG

Each element on the left portion shows the fraction of the true activity concentration (upper case) integrated in the observed ROI activity (lower case). For instance the caudate nucleus contains 67.2 % true activity of the caudate itself plus 23.3 % true activity of the background region. The right portion of the table gives the elements of the inverse matrix.

To appreciate the magnitude of the correction we determined recovery coefficients (RCs) from fractions of the observed and corrected values over the true activity in each compartment. We also computed their volume average over four slices weighted by the area of each ROI. Table 7.3 reports the mean and SD values averaged over

27 frames, with total projection counts varying from 0.5 to 1 M. As expected we observe most errors in the striatal structures. Before the PVE correction their RCs (in percentage) in each slice range from 59-72 % in CN and 54-77 % in PU while the volume values are 67.6 % and 70.1 %. Afterwards they are restored to 95-106 % in CN and 91-107 % in PU, with the volume RCs of 98.5 % and 97.3 % respectively. The values for GP are 75 % before correction and 96 % after correction in the one slice analyzed.

Table 7.3: Recovery coefficients (percentage) in the skull phantom before and after partial volume correction

ID	Slice	1	2	3	4	Volume
CN	Observed	69.4±2.6	72.4±2.5	66.8±1.9	58.9±2.2	67.6±1.5
	Corrected	98.2±4.3	94.7±3.8	97.7±2.9	106.2±5.0	98.5±2.4
PU	Observed	54.1±3.3	75.2±2.5	77.3±1.5	63.5±1.5	70.0±0.6
	Corrected	94.5±10.7	107.3±5.2	98.0±2.4	90.6±2.5	97.3±1.1
BKG	Observed	97.0±2.9	97.3±4.4	101.1±2.4	104.9±2.5	100.0±1.7
	Corrected	97.5±2.9	98.3±4.4	101.6±2.4	105.5±2.5	100.6±1.7

Data show the mean and SD of the slice and volume values averaged over 27 frames (true value = 100 %). The values in caudate and putamen are largely underestimated before correction although they have the same radioactivity concentration in the phantom. The large errors are eliminated by the correction algorithm.

Table 7.4: Noise magnification factor after partial volume correction

Slice	1	2	3	4	Volume
CN	1.17	1.17	1.07	1.24	1.12
PU	1.84	1.44	1.21	1.23	1.25
BKG	0.995	0.990	0.995	0.994	0.994

Data are computed from the ratios of coefficient of variation values obtained in Table 7.3.

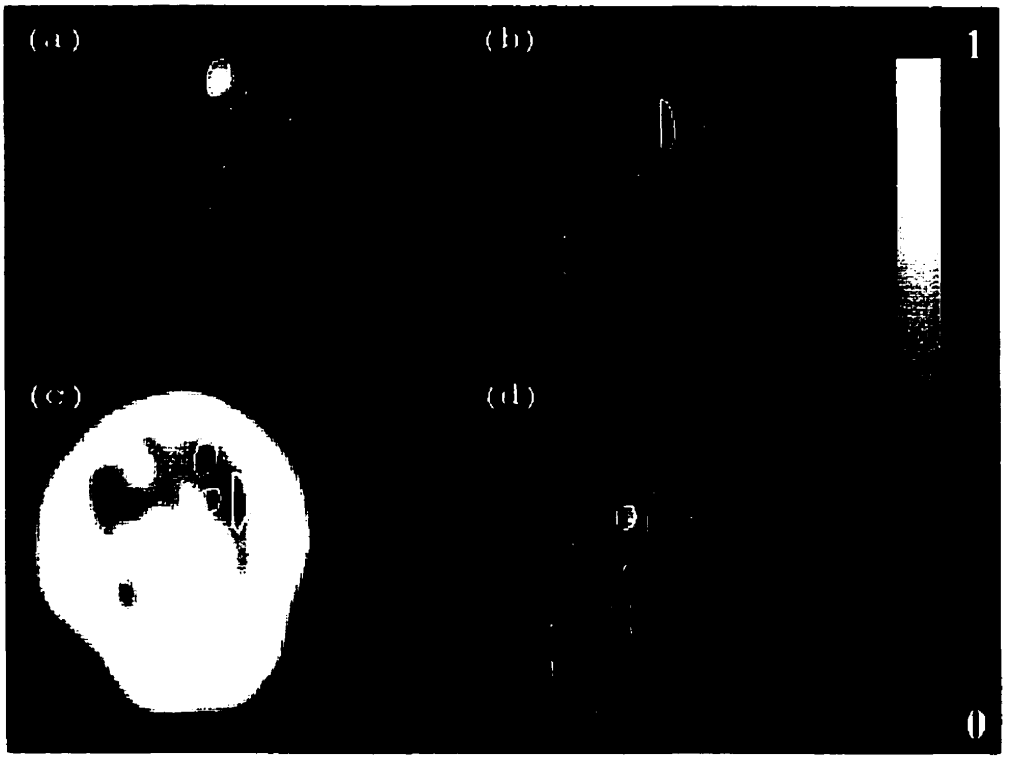

Figure 7.4: Regional spread functions from four compartments of the skull phantom. (a) caudate nuclei; (b) putamen: (c) main cavity and (d) globus pallidus. Regional templates are created on MR images to be within each structure boundary.

The regional data in Table 7.3 have relatively low SD estimates for the observed values over the entire time-series. In absolute terms they rise only slightly from 1.5-4.4 % to 2.5-5.2 % in all structures after PVE correction. Both decrease by 42-90 % in the 3-D data providing a higher precision in the corrected values. Table 7.4 lists the noise magnification factors obtained from the skull phantom. PVE corrections boost noise levels across slices by 7-24 % in CN and 21-84 % in PU. Their respective values for the volume-averaged data are 12 % and 25 % with the single-slice value of 27 % in the GP structure. Increases in all cases are smaller than the upper bound theoretical values calculated from equation 7.4. This is very encouraging considering the low statistical quality of the phantom data.

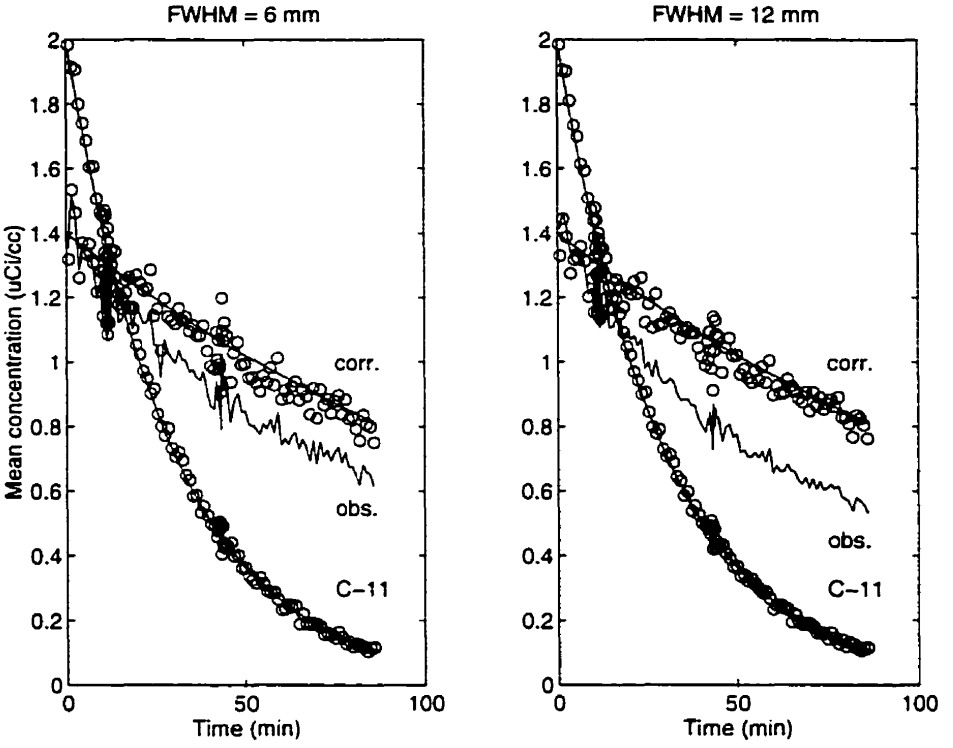

Figure 7.5: TACs extracted from the putamen of the duel-isotope skull phantom before and after partial volume correction. Notice the nonlinear reduction of the observed data and the good fit of the corrected data with the true decay curve of F-18 at both filter widths. The observed and theoretical TACs of the main compartment (C-11 curve) are also presented to demonstrate the prevailing change of contrast.

Dynamic tracer distribution:

The first skull phantom study did not test the PVE correction under changing regional contrast. Therefore a dual-isotope experiment was conducted to investigate its performance with dynamic imaging contrast [Rousset et al., 1998]. The basal ganglia (CN and PU) compartments were filled with a F-18 solution whiles the main chamber (BKG) was filled with a C-11 solution. Their initial concentrations were 14 μCi/cc and 20 μCi/cc respectively. A dynamic study was then acquired over 85 min (1 min duration per frame and 4 C-11 half-lives) on the PC4096 scanner and reconstructed

without decay correction. TACs were then extracted from each structure in PET images and restored as described above. Both the observed and corrected TACs were fitted to mono-exponential functions to derive the half-life of each tracer.

Table 7.5: Recovery of radiotracer half-lives in the duel-isotope skull phantom

Area	FWHM (mm)	Observed $T_{1/2}$ (min)	Observed Ratio* (%)	Observed rms+ (%)	Corrected $T_{1/2}$ (min)	Corrected Ratio* (%)	Corrected rms+ (%)
CN (F-18)	6	89.4	81.3	6.2	112.3	102.5	7.0
	12	74.1	67.4	4.3	113.2	103.3	5.4
PU (F-18)	6	76.8	69.8	4.1	109.6	100.0	4.2
	12	61.5	55.9	3.6	113.7	103.7	3.5
BKG (C-11)	6	20.1	98.5	1.1	20.1	98.5	1.2
	12	20.2	99.0	0.6	20.1	98.5	0.5

The ratio is relative to the true half-life value of 109.6 min for F-18 and 20.4 min for C-11. The rms is the mean root mean-square error between the sampled data and the fitted curve. Notice the underestimation of $T_{1/2}$ values in caudate nucleus and putamen before PVE correction which approach the ideal ratio of 100 % after correction.

Fig. 7.5 is a typical example to illustrate the effects of partial volume distortion and correction at two filter sizes in the image reconstruction. Initially the apparent TACs in small structures are underestimated nonlinearly to a different degree with changing contrast. After correction they match the natural decay curve of F-18 derived from the true concentration and the half-life. There is not much change in the large BKG compartment in agreement with the observation seen in the static tracer experiment. Table 7.5 shows that the half-live ($T_{1/2}$) from the raw TACs in the CN and PU regions have only 81.3 % and 69.8 % recovery at 6 mm FWHM. Both decrease by a further 14 % from the true value at 12 mm FWHM. After PVE correction the half-lives in the CN and PU structures are overestimated by less than

3.3 % and 3.7 % respectively. We see only slight increase in variances from the correction as indicated by the rms errors. This demonstrates accurate recovery of kinetic parameters at different image resolutions.

In conclusion we have developed a region-based approach to correct the 3-D PVE in each PET study using the MR data of the same brain. Brain phantom data in the static imaging experiment show that regional activity values among striatal structures are typically underestimated by 20-45 % depending on their volume and spatial location (see Table 7.3). After correction they are restored to within 5 % of the true concentration. In terms of the volumetric data the method increases activity estimates by more than 45 % while increasing the COV by less than 25 %. Data from the dynamic imaging experiment on a body tomograph reveal large errors in the observed striatal TACs and radiotracer half-lives. The apparent errors due to different object sizes/shapes and image resolutions are removed with an accuracy of better than 4 % after applying the PVE correction. This method is now in routine use at the MNI for automated correction of TAC data from various PET tracers.

7.3 Validation of Image Registration Methods

The integration of multi-modality medical images has attracted great attention because it allows a much more comprehensive analysis and diagnosis. Many automated algorithms have been written to solve two common problems: PET-MRI and PET-PET registration. The first is valuable to enhance regional data analysis in PET and improve anatomical localization, particularly in receptor binding and brain activation studies. The second is necessary when correlating PET images of the same subject acquired at different times and locations. Both have been done in the context of intra- and inter-subject comparisons. In practice we need to characterize the accuracy of

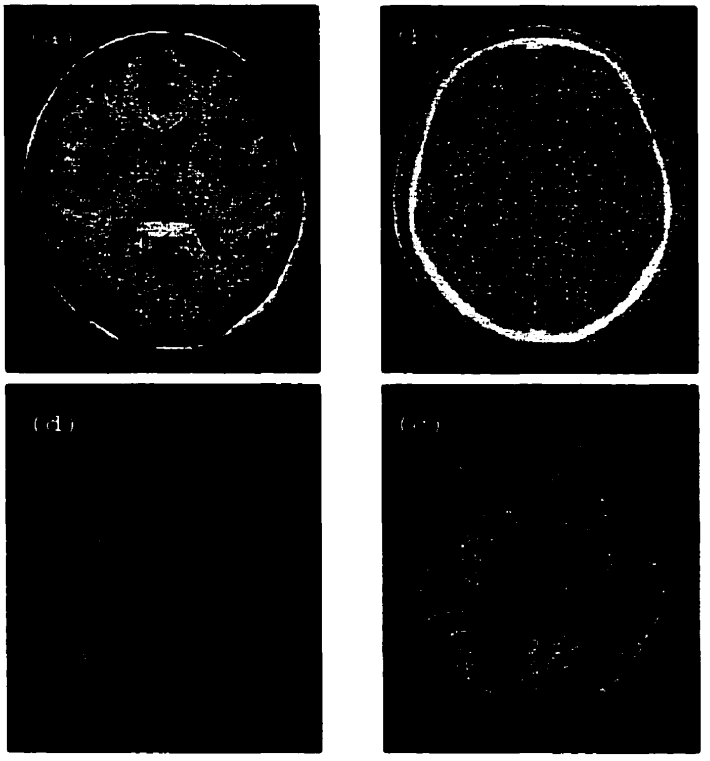

Figure 7.6: (a) MR image; (b) attenuation map; (c) activity distribution with a 4:1 uptake ratio between gray and white structures; (d) simulated PET image.

these different algorithms in realistic imaging situations.

PETSIM offers a powerful method to evaluate the performance of 3-D registration methods between PET and MRI data. The simulated PET image can be generated directly from the segmented MRI volume for any type of PET images (e.g. CBF and F-Dopa). This process can be done rapidly with desired noise levels and resolution in the image. Since both volumes are in perfect registration by definition, they can be rotated and translated from each other by a known amount and then registered back by different algorithms. The root mean square distances between a set of trial points provide a measure of total registration errors.

Table 7.6: Error in registration of simulated PET images with MRI data

Error component	X	Y	Z	Mean
Rotation error (degree)	1.9	1.5	1.6	1.67 ± 0.08
Translation error (mm)	0.9	1.5	1.4	1.27 ± 0.06
Error at 75 mm (mm)	2.7	3.2	2.6	2.83 ± 0.13

Data are the standard deviations in each dimension over 79 transformation/registration runs on two subjects. Errors in all three dimensions are effectively the same.

7.3.1 Emission image registration

As an example we previously validated the accuracy of a landmark-based method using 3-D simulated PET images [Neelin et al., 1993]. CBF-FDG type images were reconstructed at 10 and 20 mm resolution after assigning activity distribution to each structure (Fig. 7.6). Errors from the algorithm itself and from the uncertainty in landmark identification were estimated separately. In each trial the MR volume was subjected to a random rotation and translation before being registered to the PET data. This was repeated 39 times on one subject and 40 times on another. Three types of errors were then calculated by averaging over 79 simulations. Table 7.6 shows that the rms distance in each dimension runs from 1.3 mm at the centroid to 2.8 mm at 75 mm from the centroid. Overall the registration method achieves a 3-D error of 2-4 mm from the center to the surface of the brain for 15 pairs of homologous points.

7.3.2 Transmission image registration

Current direct registration methods work when image volumes have common and correlated features to match. Typical examples of image features include intensity and its derivatives. While true in normal CBF and FDG images this is not the case in

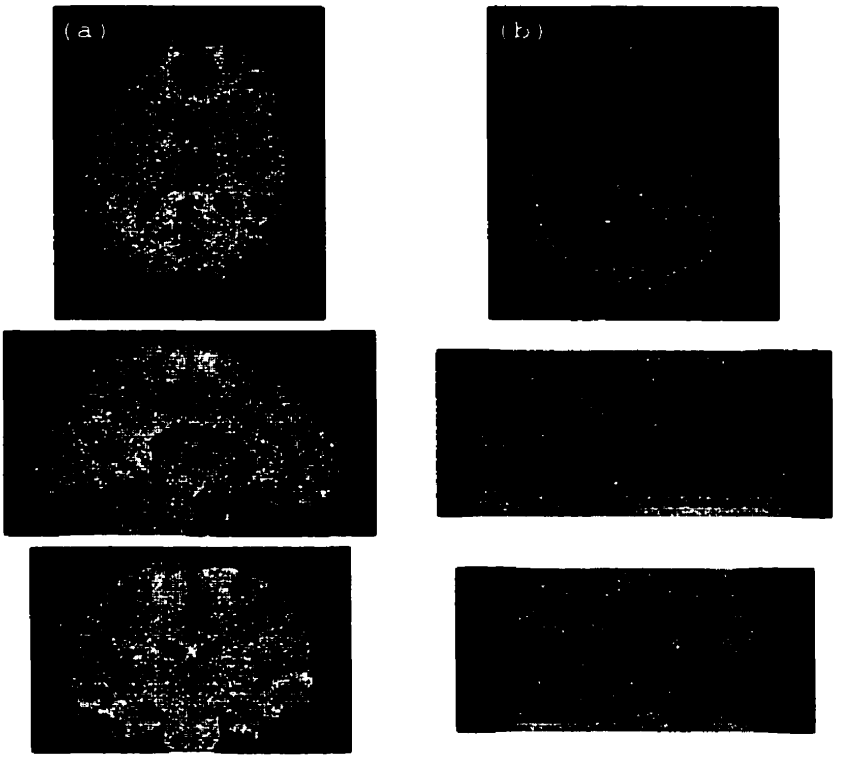

Figure 7.7: (a) MRI data (b) simulated transmission images with soft tissue and skull bone assigned attenuation values of 0.098 cm^{-1} and 0.151 cm^{-1} respectively. PET images have 9 M maximum counts in central slices and a 11.7 mm FWHM resolution.

neuroreceptor imaging and diseases such as stroke or tumor studies. We have recently implemented an automatic MR-PET registration algorithm based on transmission PET scans [Gu et al., 1998]. This method is independent of the particular PET tracer and employs mutual information theory to maximize the joint probability between the MR and PET transmission image volumes. It is robust against image noise by using a large number voxels in the registration process.

We used simulated PET transmission data to test the performance of this algorithm. Following the steps described in section 5.2.6 we generated a set of 3-D transmission images from one segmented MRI volume as shown in Fig. 7.7. This was done at three typical image resolution and four different noise levels. Twenty random

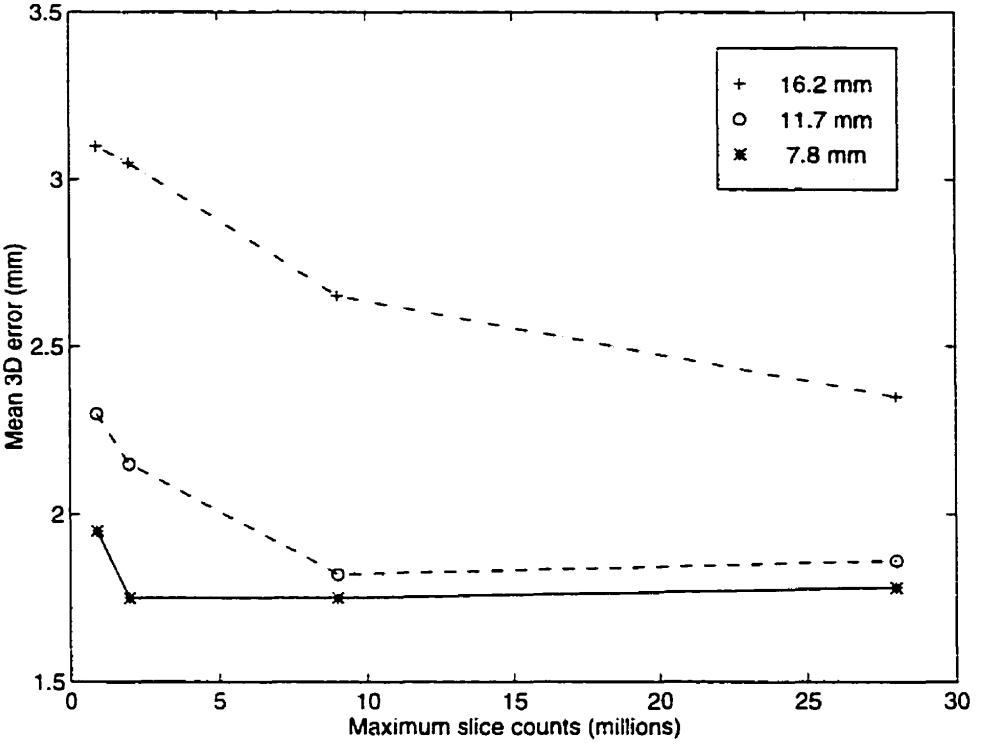

Figure 7.8: Mean registration error as a function of maximum slice counts and image resolution in PET transmission scans. The slice counts equal to 0.9, 2, 9 and 28 M respectively at four data points. Notice the larger error at poorer resolution of 16.2 mm FWHM.

transformations were applied to the MRI data before being registered to each of the twelve transmission PET images. In each case the rms distance was computed over the centroid of the brain and six points 75 mm away from the centroid along each axis. Data from 20 trials were averaged to produce the mean 3-D rms error. This process was performed using MR data from two subjects.

Fig. 7.8 shows the dependence of the misregistration error on image resolution and counting statistics. At FWHM = 7.8 mm and 11.7 mm the error curves are very close and nearly constant above 9 M counts with only small increases toward lower counts. However we observe a relatively large error at low resolution (FWHM = 16.2 mm) particularly as images become noisier (below 9 M counts). These results

indicate that the algorithm is more sensitive to image resolution than to counting noise. Data from both subjects give mean 3-D errors of less than 2 mm at image resolution $\leq$ 12 mm FWHM and total counts $\geq$ 9 M per slice. This is representative imaging conditions routinely used in PET transmission measurements.

In summary these studies demonstrate that simulated PET images are highly realistic and very useful in assessing registration errors. One can apply the same mechanism to evaluate the alignment between PET emission scans in serial studies. In addition the matching of real PET and MRI volumes can be accomplished by creating simulated PET images from the MRI data. This is useful since the PET-PET registration performs better with noisy data [Woods et al., 1993]. Considering the wide range of clinical imaging situations it is likely that more than one registration technique will be necessary. PETSIM offers a unified environment to identify the best method for a given situation.

7.4 Other Relevant Applications

The previous sections have presented three major applications of PETSIM with a focus on principles and validation. Because of its unique design this tool can be used in many different ways. In the following we summarize several other ways in which PETSIM has been used in some collaborations.

7.4.1 Parameter estimation algorithms

PET scans are mostly used to estimate kinetic model parameters in both normal and abnormal tissues. This task is often hindered by an unknown bias and variance in the recorded TACs. PETSIM gives an effective way to address this kind of problem by generating physically realistic dynamic images. Noise is much closer to the measured

data than in other simulation studies since it accounts for noise correlation through the image reconstruction process. By performing repeat simulations one can predict regional bias and variance in each scan.

A series of dynamic simulations using MR brain images have been performed to examine partial volume problems in neuroreceptor PET imaging. This is done by comparing a set of observed TACs with the true tissue TACs generated from some theoretical models of tracer kinetics. One study has shown that kinetic parameters of F-dopa uptake are grossly underestimated in caudate and putamen [Rousset et al., 1993]. The errors are removed after applying the PVE correction algorithm (section 7.2). The second study has looked into the precision issue of this method as a function of counting statistics [Rousset et al., 1996]. TACs in both striatal and cortical structures are fully corrected with a reasonable noise amplification ($<100\ \%$) that decreases as image counts increase. Both results are consistent with the brain phantom data presented above.

By simulating the uptake characteristics of certain tracers one can estimate the effects of anatomical differences on PET data and separate them from changes due to physiological factors. For instance PETSIM has been used to investigate the influence of partial volume on glucose hypometabolism in temporal lobe epilepsy [Lee, 1998]. FDG images are simulated from MRI brain volumes spatially matched with the real PET scan. Comparison between them shows that the PVE contributes significantly to the observed reduction and asymmetry in glucose uptake of the patients. Working with clinicians it is possible to evaluate the detectability of small lesions and predict disease patterns in some neurological disorders.

PETSIM also provides an objective criteria to compare and optimize temporal sampling sequences in the data collection of any dynamic PET study. We have done

some preliminary work on quantifying neurotransmitter release in combination with rigorous statistical analysis [Aston et al., 1998]. This type of study is a challenge since it involves transient and very low tracer uptake in small brain structures under a receptor modification task or pharmacological intervention. Simulations can help identify optimal tracer injection and scanning conditions very quickly. This is especially valuable since it allows us to design and validate imaging protocols before their implementation with human subjects.

Many kinetic models have been proposed to measure parameters for a large number of radiotracers (section 2.5). PETSIM offers a realistic framework to validate the performance of different estimation algorithms on both voxel and regional levels. It can also evaluate other popular methods which use spectral and factor analysis to extract the principal components in dynamic PET studies [Cunningham and Jones, 1993, Wu et al., 1995]. In particular one can explore the use of variance maps as weighting factors in parameter estimation. This would improve the kinetic data analysis strategy in a wide variety of imaging situations.

7.4.2 Statistical image reconstruction methods

In recent years there has been increased interest in iterative image reconstruction algorithms to reduce the bias and variance introduced by filtered backprojection (section 2.3.2). One area of some considerable interest is the incorporation of MRI data into PET reconstruction to restrict radioactivity to anatomically meaningful regions. This stems from the improved computational power and data fusion ability that now exist in many imaging centers. However their efficacy has yet to be validated in general clinical studies. PETSIM provides not only a physically realistic sinogram model but also an effective way to evaluate algorithmic performance in dynamic imaging

situations.

We have implemented several iterative reconstruction algorithms including basic Maximum-likelihood and Bayesian methods with and without the correlated structural information [Zhang et al., 1993]. This initial study used only a limited data model to explore MRI-weighted PET image reconstruction. In particular the preliminary results show better performance of Bayesian methods with gradient and tissue classification priors. We can restore image contrast between gray matter and white matter structures and also enhance the SNR of small hot/cold lesions with the surrounding areas. We have recently improved and compared these methods using simulated data from the Hoffman brain phantom [Murase et al., 1996b]. This algorithm is ready for clinical evaluation with cerebral blood flow and metabolic image data.

With recent advances it becomes necessary to improve the convergence of these algorithms with some regularization and to increase the execution speed with the notion of ordered subsets [Hudson and Larkin, 1994]. This would provide new insights into receptor binding and physiological activation studies where activity is highly localized in small and irregular brain structures. It would be interesting to perform a comparison with all other PVE correction methods described in section 7.2.

7.5 Summary

In this chapter we have described many different applications of PETSIM in addressing clinical questions. This stems from its ability to model each distortion source in PET imaging protocols. First, we have examined the interaction between partial volume effects and statistical noise. This allows the selection of proper image acquisition parameters for optimal signal/noise ratios. Second, we have demonstrated that

it is possible to estimate and correct partial volume distortions in PET neurological studies using correlated anatomical data. Scan data from a 3-D brain phantom of the basal ganglia reveal spatially and temporally variant distortions in the observed TACs and large errors in the fitted model parameters. Such errors are reduced to within 5% after PVE correction with tolerable noise amplification. Third, we have shown that MRI-PET registration can be achieved with a 3-D accuracy of less than 3 mm using both emission and transmission PET images. Finally we have briefly discussed its extended use in evaluating the impact of PVE on kinetic parameter estimation as well as comparing image reconstruction methods. In conclusion PETSIM offers a viable simulation environment to evaluate and optimize PET imaging methodology.

Chapter 8

Conclusions and Perspectives

In this thesis we have described an analytical PET simulation system (PETSIM) which models all key physical components of any particular tomograph. It can generate 3-D simulated PET sinogram and image data from any realistic brain model. This chapter summarizes the current status and application areas of PETSIM as well as discussing some extensions of this research program in the near future.

8.1 Summary of Present Project

The PETSIM system includes both object and scanning dependent characteristics in a PET study (see Chapter 5). Correlated brain image data are segmented into discrete tissue class maps of gray matter, white matter, CSF, skull bone and skin surface. Specific neuroanatomical structures such as the caudate nucleus or thalamus can be delineated automatically if they have different functional attributes than other areas within the same tissue class. An example is in receptor binding studies where radiotracers accumulate predominantly in the basal ganglia belonging to gray matter. 3-D brain models for both emission and transmission simulations are generated by assigning radionuclide concentration and tissue attenuation coefficients to each structure

according to the expected tracer biodistribution data. Sinogram data are then computed at many axial, angular and transverse positions using the acquisition geometry and 3-D detector PSF of the tomographic imaging system. Physical effects modeled include attenuation, scatter, randoms, detection efficiency and deadtime, scan length, radioactive decay and statistical noise. Simulated data undergo the same processing as in commercial PET scanners to obtain both emission and transmission images. The methods differ from others in that one can specify and calculate each physical factor explicitly.

A series of phantom studies has been conducted to calibrate and validate the quantitative performance of this computer-simulated PET imaging system (refer to Chapter 6). While the set of calibration scans is necessary to derive model parameters for a given camera the other experiments establish the accuracy of computational algorithms. Simulation data from multiple spheres match accurately with observed regional values within each sphere. Numerical analyses show that simulated and measured projection components of a flood phantom are in excellent agreement with each other. Compared to the calculation the measured attenuation factors are increasingly underestimated toward the center of the object, but slightly overestimated outside the object. This is largely attributed to small amounts of scatter and randoms in PET transmission scans that are not included in the present simulation.

We have also used two realistic physical phantoms: the Hoffman brain phantom constructed from lucite layers and the striatal brain phantom built from a human skull. Both are based on computerized 3-D brain phantoms to emulate radiotracer uptake in cerebral metabolism and neuroreceptor imaging studies respectively. Accurate agreement is observed between simulated and measured data for the scatter and random components of the Hoffman phantom. While showing reasonably good match

between real data and simulation both sets of data reveal spatially variant quantification errors in regional activity values. These errors depend on the size of structure and its position in the tomograph as a result of partial volume effects (PVE).

However there are still some residual disagreement between the simulated and real images. This may come from several sources: (1) errors in the simulation of 3-D image resolution of the PET camera, (2) the slightly different attenuation factors shown above, and (3) the limited accuracy attainable from MR scans of the brain phantoms. The last two problems could also result from a potential mismatch between the physical and digital versions of the brain phantoms. A better phantom model could be created by performing high resolution X-ray CT scans with 1 mm thickness.

After the validation PETSIM has been used to study a number of issues affecting image quantification (see Chapter 7). First we have shown its utility in estimating regional bias and variance in dynamic imaging studies. Particularly one can separate contributions to image variances from resolution distortions and counting statistics. By quantifying their dependence on reconstruction filters and total counts one can choose optimal data acquisition and analysis parameters. We have also demonstrated its usefulness in the comparison of inter-modality matching algorithms between MR and PET scans under varying imaging conditions. This helps verify an automatic new image registration method best suitable for neuroreceptor or disease studies.

Importantly we have established a general methodology which is capable of removing 3-D PVE in dynamic emission studies using the correlated MR/CT images. This method is based on the calculation of a transfer matrix relating the apparent and true activity values in all structures of interest. Its elements reflect the interaction of each structure with the scanner and the spillover effects between structures during the scan. A simple matrix inversion allows simultaneous correction of partial

volume distortions from both data acquisition and image reconstruction. Dynamic simulations using PETSIM in our laboratory demonstrate that the 3-D PVE generally distorts the shape/amplitude of the observed TACs with large errors in the estimated rate constants. Applications of the correction algorithm show complete restoration of TACs and physiological rate constants. The accuracy and precision of this method has been validated using a 3-D skull phantom of the human basal ganglia with both static and dynamic imaging conditions.

We can now use PETSIM without modifying the reconstruction program of a particular scanner and it is applicable to any PET system with multi-slice acquisition. This includes the fully 3-D PET cameras operating in 2-D mode. Importantly the entire process can be done rapidly and automatically on a single computing platform. The results derived from the use of PETSIM show that the simulated 3-D images of cerebral blood flow, metabolism and neuroreceptor uptake are in good agreement with normal PET brain scans. Further validation can be done by assigning the PVE-corrected TACs to the brain models and comparing simulations with real scan data. Some of this work is already under way.

8.2 Future Work

8.2.1 Further applications

As MRI is increasingly used for functional activation studies, PET will tend to concentrate more on investigations of receptor, transmitter and enzyme kinetics in normal and abnormal brains using various radio-ligands. Besides the more traditional steady-state measurement of kinetic parameters this will also include mapping neuroreceptor activation during behavioral stimulation or pharmacological challenge.

We need to incorporate PETSIM into the development of research imaging protocols to evaluate their efficacy. This can be performed either at the TAC level or with the extracted functional parameters. We can study the effect of each imaging variable or parameter and compare different data analysis methods. For example simulations using the Hoffman brain phantom have demonstrated the feasibility of performing a dual-tracer paradigm in a single session [Koeppe et al., 1998]. PETSIM uses both structural and functional data of the individual brain and hence offers a powerful tool for validating the design of a large number of PET imaging experiments.

PET activation studies in a single subject are becoming more popular with the improvement in scanner sensitivity and resolution. This has moved investigations from localizing only peaks to their morphological distributions. For instance there is an increased interest in the connectivity between different functional brain networks using regional metabolic and blood flow data [Alexander and Moeller, 1994, Paus et al., 1996]. PETSIM will be a valuable tool to examine the signal-to-noise issue and resolution trade-off between object size/shape and contrast in both baseline and activation states. We can then assess the ability of a particular strategy to reveal true correlation patterns between brain regions in normal or disease.

So far we have done partial volume corrections in neuroreceptor studies with F-dopa and Raclopride [Rousset et al., 1993, Yokoi et al., 1998]. In order to take full advantage of this algorithm we should pursue the following: (1) apply it to other radiotracers and biological systems: (2) evaluate its efficacy in clinical correlation imaging. For instance we can compare two groups of subjects - normals and patients with and without correction. A particularly valuable use is in imaging neurodegenerative processes such as Huntington's disease, where both the biochemical state and the amount of atrophy vary at different rates within/between groups and as a func-

tion of time. This will reduce or eliminate regional variability in PET data due to scan-specific characteristics and anatomical differences. It provides absolute quantification of cerebral function for physiological comparison between regions, scans and research centers.

After observing the promising results from dynamic PET data in the brain we can expect similar improvements in the imaging accuracy of cardiac scans as well. One important use is to derive plasma curves from TACs in the left ventricle without any blood sampling. This will increase the throughput in body imaging work.

With the continued increase in image resolution one can segment certain regions from different brain and cardiac PET images. PETSIM will be useful for evaluating functional tissue classification algorithms in clinical studies. This is also applicable to attenuation correction methods based on segmentation of transmission PET images of the body. Finally PETSIM can generate interleaved PET data at any axial position and arbitrary orientation. It allows us to investigate the effects of subject movement during or between emission and transmission scans.

8.2.2 Extensions to the software

Although many key features of PET imaging modality have been implemented there are still a number of limitations requiring further improvement. The current version of PETSIM is driven by a set of parameter files and runs separately from computing tools dealing with tracer kinetic models. In order to simplify its usage and increase productivity we should create a graphic user interface and a better linkage with tracer modeling programs. This would provide a complete solution for realistic testing of kinetic data analysis algorithms. Work is also under way to port the software onto personal computers which are becoming more powerful in recent years.

8.2.3 Extensions to 2-D modeling

The sinogram model employed in the current study can be extended in several ways. We use only a uniform Gaussian function to model the 3-D PSF of the scanner. We are modifying our program to handle the spatial variation in axial and in-plane resolutions as well as differences between direct and cross slices. This will reveal more image distortions caused by non-uniform tomograph resolution in 3-D. While randoms and deadtime factor are count-rate specific both remain constant over projection positions in each slice. In the short term we should model the radial variation of the randoms and deadtime in each pair of coincident detectors. As noted above we also need to include scatter and randoms in simulated blank and transmission scans. This is necessary to evaluate different scatter and attenuation correction methods in image reconstruction. Finally the effect of scanner wobble motion can be incorporated by fine-sampling projection data at the corresponding positions.

Statistical reconstruction is a fundamental approach to emission and transmission tomographic imaging. This work has laid a solid foundation to implement and validate such image reconstruction algorithms. Working with others at our laboratory we have demonstrated the improved image quality of an MR-guided Bayesian reconstruction method. It would be straight-forward to incorporate the full physical model into the iteration steps. This would allow automatic PVE correction and noise suppression. We can also compare its performance with the current *a posteriori* correction methods.

8.2.4 Extensions to fully 3-D systems

With the installation of the new generation PET scanners it is necessary to extend PETSIM to handle truly 3-D data acquisition and image reconstruction. Although the present simulation is a good approximation to such a system the set

of programs will be expanded according to the latest PET cameras such as GE Advance and ECAT HR+. We can model the key physical components in 3-D mode based on Monte Carlo simulations and experimental characterization data [DeGrado et al., 1994, Adam et al., 1997]. For instance one can scan point sources and phantoms to measure the spatially variant 3-D PSF and count-rate behavior at each coincidence line. Physical effects can then be included using the same principle as detailed in this thesis.

Actual simulation would involve computationally intensive ray-tracing of activity distribution according to the 3-D geometry of coincidence detectors. A particular problem is the increased level of scatter due to the absence of inter-plane septa. These events can be modeled by modifying scatter convolution filters derived by others [Bailey and Meikle, 1994, Ollinger, 1996]. Simulated projection data can then be reconstructed using the commercially available projection-backprojection algorithm. Some work may be needed to establish simplifications for faster computation.

Ultimately this research program will result in an accurate 3-D simulation tool for evaluating and optimizing PET data collection, image reconstruction, ROI analysis and physiological parameter estimation. This effort will improve the accuracy and precision of kinetic analysis in a wide variety of functional imaging applications. Its success requires rigorous validation with highly realistic 3-D brain phantoms and real scan data. A tissue-equivalent anthropomorphic phantom (Radiological Support Devices Inc, Long Beach, CA) would be suitable for this purpose by combining the entire human head and separate anatomical structures.

Bibliography

[Adam et al., 1997] Adam, L., Zaers, J., Ostertag, H., Trojan, H., Bellemann, M., and Brix, G. (1997). Performance evaluation of the whole-body PET scanner ECAT EXACT HR+. *IEEE Trans. Nucl. Sci.*, 44(3):1172–1179.

[Alexander and Moeller, 1994] Alexander, G. and Moeller, J. (1994). Application of the scaled subprofile model to functional imaging in neuropsychiatric disorders: a principal component approach to modeling brain function in disease. *Human brain mapping*, 2:79–94.

[Andersson et al., 1995] Andersson, J., Sundin, A., and Valind, S. (1995). A method for coregistration of PET and MR brain images. *J. Nucl. Med.*, 36:1307–1315.

[Aston et al., 1998] Aston, J., Dagher, A., Worsley, K., Ma, Y., and Evans, A. (1998). Measuring neurotransmitter release with PET: simulation studies. *NeuroImage*, 7:A64. 2nd Int. Symp. Neuroreceptor Mapping of Living Brain, Ann Arbor, USA, June 1998.

[Bailey and Meikle, 1994] Bailey, D. and Meikle, S. (1994). A convolution-subtraction scatter correction method for 3D PET. *Phys. Med. Biol.*, 39:412–424.

[Beanlands et al., 1997] Beanlands, R., deKemp, R., Scheffel, A., and et al, C. N. (1997). Can nitrogen-13 ammonia kinetic modeling define myocardial viability

independent of fluorine-18 fluorodeoxyglucose ? *Journal American College of Cardiology*, 29:537–543.

[Bendriem et al., 1991] Bendriem, B., Dewey, S., Schlyer, D., Wolf, A., and Volkow, N. (1991). Positron emission tomography: a phantom study of the effect of contrast and axial positioning. *IEEE Trans. Med. Imag.*, 10:216–222.

[Bentourkia et al., 1995a] Bentourkia, M., Msaki, P., Cadorette, J., and Lecomte, R. (1995a). Assessment of scatter components in high-resolution PET: correction by non-stationary convolution subtraction. *J. Nucl. Med.*, 36:121–130.

[Bentourkia et al., 1995b] Bentourkia, M., Msaki, P., Cadorette, J., and Lecomte, R. (1995b). Energy dependence of scatter components in multi-spectra PET imaging. *IEEE Trans. Med. Imag.*, 14:138–145.

[Bergman et al., 1998] Bergman, A., Thompson, C., Murthy, K., Robar, J., Clancy, R., and English, M. (1998). Technique to obtain positron emission mammography images in registration with x-ray mammograms. *Medical Physics*, 25:2119–2129.

[Bergstrom et al., 1983] Bergstrom, M., Eriksson, L., Bohm, C., Blomqvist, G., and Litton, J. (1983). Correction for scattered radiation in a ring detector positron camera by integral transformation of the projections. *J. Comput. Assist. Tomogr.*, 7:42–50.

[Blomqvist et al., 1995] Blomqvist, G., Lammertsma, A., Mazoyer, B., and Wienhard, K. (1995). Effect of tissue heterogeneity on quantification in positron emission tomography. *Eur. J. Nucl. Med.*, 22:652–663.

[Bowsher et al., 1996] Bowsher, J., Johnson, V., and Turkington, T. (1996). Bayesian reconstruction and use of anatomical a priori information for emission tomograph. *IEEE Trans. Med. Img.*, 15:673–686.

[Brooks et al., 1987] Brooks, R., Hatazawa, J., Chiro, G., Larson, S., and Fishbein, D. (1987). Human cerebral glucose metabolism determined by PET: A revisit. *J. Cereb. Blood Flow Metab.*, 7:427–432.

[Carson et al., 1994] Carson, R., Chen, Y., Chodkowski, B., Yap, T., and Daube-Witherspoon, M. (1994). Precision and accuracy of regional radioactivity quantitation using the maximum likelihood EM reconstruction algorithm. *IEEE Trans. Med. Imag.*, 13:526–537.

[Carson et al., 1988] Carson, R., Daube-Witherspoon, M., and Green, M. (1988). A method for postinjection PET transmission measurements with a rotating source. *J. Nucl. Med.*, 22:627–637.

[Carson et al., 1993] Carson, R., Yan, Y., Daube-Witherspoon, M., Freedman, N., Bacharach, S., and Herscovitch, P. (1993). An approximation formula for the variance of PET regions of interest values. *IEEE Trans. Med. Imag.*, 12:240–250.

[Chen et al., 1992] Chen, C., Cooper, M., Chou, J., and Nathan, M. (1992). Design of brain phantoms for computer simulation studies of image reconstruction algorithms and physiological models. *J. Nucl. Med.*, 33:1012.

[Cherry and Phelps, 1996] Cherry, S. and Phelps, M. (1996). Imaging brain function with positron emission tomography. *Brain Mapping: The Methods*, pages 191–221.

[Cherry et al., 1997] Cherry, S., Shao, Y., and et al, R. S. (1997). MicroPET: A high resolution PET scanner for imaging small animals. *IEEE Trans. Nucl. Sci.*, 44:1161–1166.

[Cherry et al., 1995] Cherry, S., Woods, R., Doshi, N., Banerjee, P., and Mazziotta, J. (1995). Improved signal-to-noise in PET activation studies using switched paradigms. *J. Nucl. Med.*, 36:307–314.

[Cho et al., 1993] Cho, Z., Jones, J., and Singh, M. (1993). *Foundations of Medical Imaging*. Wiley, New York.

[Collins et al., 1998] Collins, D., Zijdenbos, A., Kollokian, V., Holmes, C., and Evans, A. (1998). Design and construction of a realistic digital brain phantom. *IEEE Trans. Med. Imag.*, 17:463–468.

[Collins et al., 1995] Collins, L., Holmes, C., Peters, T., and Evans, A. (1995). Automatic 3-D model-based neuroanatomical segmentation. *Human Brain Mapping*, 3:190–208.

[Collins et al., 1994] Collins, L., Neelin, P., Peters, T., and Evans, A. (1994). Automatic 3-D inter-subject registration of MR volumetric data in standardized Talairach space. *J. Comput. Assist. Tomogr.*, 18:192–205.

[Cooke and Evans, 1983] Cooke, B. and Evans, A. (1983). A phantom to assess quantitative recovery of positron tomographs. *J. Comput. Assist. Tomogr.*, 7:876–880.

[Cunningham and Jones, 1993] Cunningham, V. and Jones, T. (1993). Spectra analysis of dynamic PET studies. *J. Cereb. Blood Flow Metab.*, 13:15–23.

[Daube-Witherspoon and Carson, 1991] Daube-Witherspoon, M. and Carson, R. (1991). Unified deadtime correction model for PET. *IEEE Trans. Med. Imag.*, 10:267–275.

[Daube-Witherspoon et al., 1992] Daube-Witherspoon, M., Carson, R., Chen, Y., and Yap, T. (1992). Scatter correction in ML reconstruction of PET data. *Proc. IEEE Nucl. Sci. Symp. and Med. Imag. Conf.*, 2:945–947.

[Defrise et al., 1997] Defrise, M., Kinahan, P., Townsend, D., Michel, C., Sibomana, M., and Newport, D. (1997). Exact and approximate rebinning algorithms for 3-D PET data. *IEEE Trans. Med. Imag.*, 16:145–158.

[DeGrado et al., 1994] DeGrado, T., Turkington, T., Williams, J., Stearns, C., Hoffman, J., and Coleman, R. (1994). Performance characteristics of a whole-body PET scanner. *J. Nucl. Med.*, 35:1398–1406.

[deKemp and Nahmias, 1994] deKemp, R. and Nahmias, C. (1994). Attenuation correction in PET using single photon transmission measurement. *Med. Phys.*, 21:771–778.

[Derenzo et al., 1993] Derenzo, S., Moses, W., Huesman, R., and Budinger, T. (1993). Critical instrumentation issues for <2 mm resolution, high sensitivity brain PET. In Uemura, K., Lassen, N., Jones, T., and Kanno, I., editors, *Quantification of brain function using PET*, pages 25–37, Amsterdam. Elsevier.

[Diksic and Reba, 1991] Diksic, M. and Reba, R. C. (1991). *Radiopharmaceuticals and brain pathology: studied with PET and SPECT.* CRC Press, Boca Raton.

[Eidelberg et al., 1995] Eidelberg, D., Moeller, J., and et al, T. I. (1995). Early differential diagnosis of parkinson's disease with FDG and PET. *Neurology*, 45:1995–2004.

[Evans et al., 1992a] Evans, A., Marrett, S., and et al, P. N. (1992a). Anatomical mapping of functional activation in stereotactic space. *NeuroImage*, 1:43–53.

[Evans et al., 1991a] Evans, A., Marrett, S., Torrescorzo, J., Ku, S., and Collins, L. (1991a). MRI-PET correlation in three dimensions using a volume of interest (VOI) atlas. *J. Cereb. Blood Flow Metab.*, 11:A69–A78.

[Evans et al., 1992b] Evans, A., Peters, T., Collins, D., Henry, C., Marrett, T., Pike, G., and Dai, W. (1992b). 3-D correlative imaging and segmentation of cerebral anatomy, function and vasculature. *Automedica*, 14:65–80.

[Evans et al., 1991b] Evans, A., Thompson, C., Marrett, S., Meyer, E., and Mazza, M. (1991b). Performance evaluation of the PC-2048: a new 15-slice encoded-crystal PET scanner for neurological studies. *IEEE Trans. Med. Imag.*, 10:90–98.

[Feng et al., 1995] Feng, D., Ho, D., and et al., K. C. (1995). An evaluation of the algorithms for determining LCMR of glucose using PET dynamic data. *IEEE Trans. Med. Imag.*, 14:697–710.

[Friston et al., 1995] Friston, K., Holmes, A., Worsley, K., Poline, J., Frith, C., and Frackowiak, R. (1995). Statistical parametric maps in functional imaging: A general linear approach. *Human Brain Mapping*, 2:189–210.

[Ginovart et al., 1997] Ginovart, N., Lundin, A., and et al, L. F. (1997). PET study of the pre- and post-synaptic dopaminergic markers for the neurodegenerative process in Huntington's disease. *Brain*, 120:503–514.

[Gjedde and Wong, 1990] Gjedde, A. and Wong, D. (1990). Modeling neuroreceptor binding of radioligands in vivo. In Frost, J. and H.N. Wagner, J., editors, *Quantitative Imaging: Neuroreceptors, Neurotransmitters, and Enzymes*, pages 51–79, New York. Raven Press.

[Grady, 1991] Grady, C. (1991). Quantitative comparison of measurements of cerebral glucose metabolic rates made with two positron cameras. *J. Cereb. Blood Flow Metab.*, 11:A57–A63.

[Graham and Lewellen, 1993] Graham, M. and Lewellen, B. (1993). High-speed automated discrete blood sampling for PET. *J. Nucl. Med.*, 31:1357–1360.

[Greitz et al., 1991] Greitz, T., Bohm, C., Holte, S., and Eriksson, L. (1991). A computerized brain atlas: construction, anatomical content and some applications. *J. Comput. Assist. Tomogr.*, 15:26–38.

[Gu et al., 1998] Gu, W., Ma, Y., and Evans, A. (1998). Tracer-independent MR/PET image registration algorithm based on PET transmission data. *IEEE Trans. Med. Imag.*

[Heiss et al., 1995] Heiss, W., Wienhard, K., Graf, R., Lottgen, J., Pietrzyk, U., and Wagner, R. (1995). High resolution PET in cats: application of a clinical camera to experimental studies. *J. Nucl. Med.*, 36:493–498.

[Herman et al., 1989] Herman, G., Lewitt, R., Odhner, D., and Rowland, S. (1989). SNARK89 - a programming system for image reconstruction from projections. Technical Report MIPG 160. University of Pennsylvania, Philadelphia.

[Herman, 1980] Herman, G. T. (1980). *Image Reconstruction from Projections: The Fundamentals of Computerized Tomography.* Academic Press, New York.

[Herrero et al., 1988] Herrero, P., Markham, J., Myears, D., Weinheimer, C., and Bergmann, S. (1988). Measurement of myocardial blood flow with PET: correction for count spillover and partial volume effects. *Mathematical and computational modeling*, 11:807–812.

[Hoffman et al., 1991] Hoffman, E., Cutler, P., Guerrero, T., Digby, W., and Mazziotta, J. (1991). Assessment of accuracy of PET utilizing a 3-D phantom to simulate the activity distribution of FDG uptake in the human brain. *J. Cereb. Blood Flow Metab.*, 11:A17–A25.

[Hoffman et al., 1979] Hoffman, E., Huang, S., and Phelps, M. (1979). Quantitation in PET: 1. effect of object size. *J. Comput. Assist. Tomogr.*, 3:299–308.

[Hoffman and Phelps, 1986] Hoffman, E. and Phelps, M. (1986). PET: principles and quantitation. In Phelps, M., Mazziotta, J., and Schelbert, H., editors, *Positron Emission Tomography and Autoradiography: Principles and Applications for the Brain and the Heart*, pages 237–286, New York. Raven Press.

[Hooper et al., 1996] Hooper, P., Meikle, S., Eberl, S., and Fulham, M. (1996). Validation of postinjection transmission measurements for attenuation correction in neurological FDG-PET studies. *J. Nucl. Med.*, 37:128–136.

[Hounsfield, 1973] Hounsfield, G. (1973). Computerized transverse axial scanning (tomography): 1. description of system. *British Journal of Radiology*, 46:1016–1022.

[Huang et al., 1987] Huang, S., Mahoney, D., and Phelps, M. (1987). Quantitation in PET: 8. effect of nonlinear parameter estimation on functional images. *J. Comput. Assist. Tomogr.*, 11:314–325.

[Hudson and Larkin, 1994] Hudson, H. M. and Larkin, R. S. (1994). Accelerated image reconstruction using ordered subsets of projection data. *IEEE Trans. Med. Imag.*, 13(4):601–609.

[Huesman et al., 1989] Huesman, R., Salmeron, E., and Baker, J. (1989). Compensation for crystal penetration in high resolution positron tomography. *IEEE Trans. Nucl. Sci.*, 36:1100–1107.

[Hutchins, 1991] Hutchins, G. (1991). Simulation of signal recovery in PET studies of cerebral physiology and biochemistry. In Nagel, J. H. and Smith, W. M., editors, *13th IEEE-EMBS Annual International Conference*, pages 215–216, Orlando, Florida. IEEE, Piscataway, NJ.

[Hutchins et al., 1992] Hutchins, G., Garaher, J. M., and Raylman, R. R. (1992). A region of interest strategy for minimizing resolution distortions in quantitative myocardial PET studies. *J. Nucl. Med.*, 33:1243–1250.

[Hutchins et al., 1990] Hutchins, G., Rogers, W., Chiao, P., Raylman, R. R., and Murphy, B. (1990). Constrained least square filtering in high resolution PET and SPECT imaging. *IEEE Trans. Nucl. Sci.*, 37:647–651.

[Johns and Cunningham, 1969] Johns, H. and Cunningham, J. (1969). *The Physics of radiology*. Charles C Thomas, Springfiled, IL, 3rd edition.

[Jones et al., 1995] Jones, W., Digby, W., Luk, W., Casey, M., and Byars, L. (1995). Optimizing rod window width in positron emission tomography. *IEEE Trans. Med. Imag.*, 14(2):266–270.

[Jovkar et al., 1989] Jovkar, S., Evans, A., Diksic, M., Nakai, H., and Yamamoto, L. (1989). Minimisation of parameter estimation errors in dynamic PET: choice of scanning schedules. *Phys. Med. Biol.*, 34:895–908.

[Kamber et al., 1995] Kamber, M., Shinghal, R., Collins, D., Francis, G., and Evans, A. (1995). Model-based 3-D segmentation of multiple sclerosis lesions in magnetic resonance brain images. *IEEE Trans. Med. Imag.*, 14:442–453.

[Karp et al., 1993] Karp, J., Kinahan, P., Muehllehner, G., and Countryman, P. (1993). Effect of increased axial field of view on the performance of a volume PET scanner. *IEEE Trans. Med. Imag.*, 12:299–306.

[Kazumata et al., 1998] Kazumata, K., Dhawan, V., and et al, T. C. (1998). Dopamine transporter imaging with Fluorine-18-FPCIT and PET. *J. Nucl. Med.*, 39:1521–1530.

[Kennedy et al., 1978] Kennedy, C., Sakurada, O., Shinohara, M., Jehle, J., and Sokoloff, L. (1978). Local cerebral glucose utilization in the normal conscious macaque monkey. *Ann. Neurol.*, 4:293–301.

[Kessler et al., 1984] Kessler, R., Ellis, J., and Eden, M. (1984). Analysis of emission tomographic scan data: limitations imposed by resolution and background. *J. Comput. Assist. Tomogr.*, 8:514–522.

[Klein et al., 1997] Klein, G., Teng, X., and et al., W. J. (1997). A methodology for specifying PET VOI's using multimodality techniques. *IEEE Trans. Med. Imag.*, 16:405–415.

[Koeppe et al., 1998] Koeppe, R., Ficaro, E., Raffel, D., Minoshima, S., and Kilbourn, M. (1998). Temporally overlapping dual tracer PET studies. In Carson,

R., Daube-Witherspoon, M., and Herscovitch, P., editors, *Quantification of brain function using PET*, pages 359–366, San Diego. Academic Press.

[Kollokian, 1996] Kollokian, V. (1996). Performance analysis of automatic techniques for tissue classification in magnetic resonance images of the human brain. Master's thesis, Dept. of Computer Science, Concordia University, Montreal, Canada.

[Kops et al., 1990] Kops, E., Herzog, H., Schmid, A., Holte, S., and Feinendegen, L. (1990). Performance characteristics of an eight-ring whole body PET scanner. *J. Comput. Assist. Tomogr.*, 14:437–445.

[Kuwabara et al., 1993] Kuwabara, H., Cumming, P., and et al, J. R. (1993). Human striatal L-DOPA decarboxylase activity estimated in vivo using FDOPA and PET: error analysis and application to normal subjects. *J. Cereb. Blood Flow Metab.*, 13:43–56.

[Kuwert et al., 1992] Kuwert, T., Ganslandt, T., and et al., P. J. (1992). Influence of size of regions of interest on PET evaluation of caudate glucose consumption. *J. Cereb. Blood Flow Metab.*, 16:789–794.

[Lammertsma et al., 1996] Lammertsma, A., Bench, C., and et al, S. H. (1996). Comparison of methods for analysis of clinical C-11 raclopride studies. *J. Cereb. Blood Flow Metab.*, 16:42–52.

[Lammertsma et al., 1990] Lammertsma, A., Cunningham, V., and et al, M. D. (1990). Combination of dynamic and integral methods for generating reproducible functional CBF images. *J. Cereb. Blood Flow Metab.*, 10:675–686.

[Lee, 1998] Lee, J. W. (1998). PET-FDG partial volume effects in temporal lobe epilepsy. In *Morphometry of the cortex in partial epilepsy*, pages 72–101, Montreal, Canada. PhD Dissertation. McGill University. Chapter 3.

[Liang, 1994] Liang, Z. (1994). Detector response restoration in image reconstruction of high resolution PET. *IEEE Trans. Med. Imag.*, 13:314–321.

[Llacer et al., 1993] Llacer, J., Veklerov, E., Coakley, K., Hoffman, E., and Nunez, J. (1993). Statistical analysis of ML estimator images of human brain FDG PET studies. *IEEE Trans. Med. Imag.*, 12(2):215–231.

[Loessner et al., 1995] Loessner, A., Alavi, A., Lewandrowski, K., Mozley, D., Souder, E., and Gur, R. (1995). Regional cerebral function determined by FDG-PET in healthy volunteers: normal patterns and changes with age. *J. Nucl. Med.*, 36:1141–1149.

[Logan et al., 1996] Logan, J., Fowler, J., Volkow, N., Wang, G., Ding, Y., and Alexoff, D. (1996). Distribution volume ratios without blood sampling from graphical analysis of PET data. *J. Cereb. Blood Flow Metab.*, 16:834–840.

[Lupton and Keller, 1983] Lupton, L. and Keller, N. (1983). Performance study of single-slice PET scanners by Monte Carlo techniques. *IEEE Trans. Med. Imag.*, MI-2:154–168.

[Ma and Evans, 1996] Ma, Y. and Evans, A. (1996). Spatial variability of regional radioactivity quantitation in blood flow and metabolic PET brain scans. *J. Nucl. Med.*, 37(5):222P. 43rd SNM Annual Meeting: Denver, June 1996.

[Ma and Evans, 1997] Ma. Y. and Evans, A. (1997). Analytical modeling of PET imaging with correlated functional and structural images. *IEEE Trans. Nucl. Sci.*, 44:2439–2444.

[Ma et al., 1993] Ma, Y., Kamber, M., and Evans, A. (1993). 3-D simulation of PET brain images using segmented MRI data and positron tomograph characteristics. *Comput. Med. Imag. Graph.*, 17:365–371.

[Ma et al., 1995] Ma, Y., Rousset, O., and Evans, A. (1995). A computationally efficient method to evaluate and optimize reconstruction parameters and data analysis of PET images. *Medical Physics*, 22:669. Proc. COMP Conference: 93-94, Montreal, June 1995.

[Ma et al., 1998] Ma, Y., Rousset, O., and Evans, A. (1998). Influence of image acquisition and reconstruction parameters on the topology of brain activation patterns with PET. *NeuroImage*, 7:S642. 4th Int. Conf. Human Brain Mapping, Montreal, Canada, June 1998.

[Mahoney et al., 1987] Mahoney, D., Huang, S., Ricci, A., Mazziotta, J., Carson, R., Hoffman, E., and Phelps, M. (1987). A realistic computer-simulated brain phantom for evaluation of PET characteristics. *IEEE Trans. Med. Imag.*, 6:250–257.

[Maze and Lecomte, 1990] Maze, A. and Lecomte, R. (1990). Analytical study of the effect of collimation on the performance of PET cameras in 3-D imaging. *IEEE Trans. Nucl. Sci.*, 37:823–831.

[Meikle et al., 1995] Meikle, S., Bailey, D., and et al., P. H. (1995). Simultaneous emission and transmission measurements for attenuation correction in whole-body PET. *J. Nucl. Med.*, 36:1680–1688.

[Meyer, 1989] Meyer, E. (1989). Simultaneous correction for tracer arrival delay and dispersion in cbf measurements by the $H_2^{15}O$ autoradiographic method and dynamic PET. *J. Nucl. Med.*, 30:1069–1078.

[Michel et al., 1991] Michel, C., Bol, A., Spinks, T., Townsend, D., Bailey, D., Grootoonk, S., and Jones, T. (1991). Assessment of response function in two PET scanners with and without interplane septa. *IEEE Trans. Med. Imag.*, 10:240–248.

[Miller et al., 1990] Miller, T., Wallis, J., and Grothe, R. (1990). Design and use of PET tomographs: the effect of slice spacing. *J. Nucl. Med.*, 31:1732–1739.

[Mintun et al., 1989] Mintun, M., Fox, P., and Raichle, M. (1989). A highly accurate method of localizing regions of neuronal activation in the human brain with PET. *J. Cereb. Blood Flow Metab.*, 9:96–103.

[Moeller et al., 1996] Moeller, J., Ishikawa, T., and et al. V. D. (1996). The metabolic topography of normal aging. *J. Cereb. Blood Flow Metab.* 16:385–398.

[Moisan et al., 1997] Moisan, C., Rogers, J., and Douglas, J. (1997). A count rate model for PET and its application to an LSO HR+ scanner. *IEEE Trans. Nucl. Sci.*, 44(3):1219–1224.

[Moses et al., 1997] Moses, W., Virador, P., Huesman, R., Derenzo, S., and Budinger, T. (1997). Design of a high resolution/sensitivity PET camera for human brains and small animals. *IEEE Trans. Nucl. Sci.*, 44:1487–1491.

[Muller-Gartner et al., 1992] Muller-Gartner, H. W., Links, J., Prince, J., Bryan, R., McVeigh, E., Leal, J., Davatzikos, C., and Frost, J. (1992). Measurement of radiotracer concentration in brain gray matter using PET: MRI-based correction for partial volume effects. *J. Cereb. Blood Flow Metab.*, 12:571–583.

[Mumcuoglu et al., 1996] Mumcuoglu, E., Leahy, R., and Cherry, S. (1996). Bayesian reconstruction of PET images: methodology and performance analysis. *Phys. Med. Biol.*, 41:1777–807.

[Murase et al., 1996a] Murase, K., Kuwabara, H., Yasuhara, Y., Evans, A., and Gjedde, A. (1996a). Mapping of change in cerebral glucose utilization using FDG double injection and the constrained weighted-integration method. *IEEE Trans. Med. Img.*, 15(6):824–835.

[Murase et al., 1996b] Murase, K., Zhang, Y., Ma, Y., and Evans, A. (1996b). Usefulness of a newly developed MRI-constrained PET image reconstruction method. *J. Nucl. Med.*, 37(5):223P. 43rd SNM Annual Meeting: Denver, June 1996.

[Neelin et al., 1993] Neelin, P., Crossman, J., Hawkes, D., Ma, Y., and Evans, A. (1993). Validation of an MR-PET landmark registration method using 3-D simulated PET images and point simulations. *Comput. Med. Imag. Graph.*, 17:351–356.

[Ohta et al., 1996] Ohta, S., Meyer, E., Fujita, H., Evans, D. R. A., and Gjedde, A. (1996). Cerebral O-15 water clearance in humans determined by PET: I. theory and normal values. *J. Cereb. Blood Flow Metab.*, 16:765–780.

[Ollinger, 1996] Ollinger, J. (1996). Model-based scatter correction for fully 3D PET. *Phys. Med. Biol.*, 41:153–176.

[Ouyang et al., 1994] Ouyang, X., Wong, W., Johnson, V., Hu, X., and Chen, C. (1994). Incorporation of correlated structural images in PET image reconstruction. *IEEE Trans. Med. Imag.*, 13:627–640.

[Palmer and Brownell, 1992] Palmer, M. and Brownell, G. (1992). Annihilation density distribution calculations for medically important positron emitters. *IEEE Trans. Med. Imag.*, 11:373–378.

[Paus et al., 1996] Paus, T., Marrett, S., Worsley, K., and Evans, A. (1996). Imaging motor-to-sensory discharges in the human brain: an experimental tool for the assessment of functional connectivity. *NeuroImage*, 4:78–86.

[Pawitan and O'Sullivan, 1993] Pawitan, Y. and O'Sullivan, F. (1993). Data-dependent bandwidth selection for emission CT reconstruction. *IEEE Trans. Med. Imag.*, 12(2):167–172.

[Pelizzari et al., 1989] Pelizzari, C., Chen, G., Spelbring, D., Weichselbaum, R., and Chen, C. (1989). Accurate 3-D registration of CT, PET, and/or MR images of the brain. *J. Comput. Assist. Tomogr.*, 13:20–26.

[Phelps et al., 1975] Phelps, M., Hoffman, E., Huang, S., and Ter-Pogossian, M. (1975). Effect of positron range on spatial resolution. *J. Nucl. Med.*, 16:649–652.

[Phelps et al., 1982] Phelps, M., Huang, S., Hoffman, E., Plummer, D., and Carson, R. (1982). An analysis of signal amplification using small detectors in PET. *J. Comput. Assist. Tomogr.*, 6:551–565.

[Picard and Thompson, 1994] Picard, Y. and Thompson, C. (1994). Determination of the centroid of interaction of crystals in block detectors for PET. *IEEE Trans. Nucl. Sci.*, 41:1464–1468.

[Picard et al., 1992] Picard, Y., Thompson, C., and Marrett, S. (1992). Improving the precision and accuracy of Monte Carlo simulation in PET. *IEEE Trans. Nucl. Sci.*, 39:1111–1116.

[Politte, 1990] Politte, D. (1990). Image improvements in PET due to measuring differential time-of-flight and using ML estimation. *IEEE Trans. Nucl. Sci.*, 37:737–742.

[Press et al., 1992] Press, W., Teukolsky, S., Vetterling, W., and Flannery, B. P. (1992). *Numerical Recipes in C: The Art of Scientific Computing.* Cambridge University Press, New York, 2nd edition.

[Rousset et al., 1998] Rousset, O., Ma, Y., and Evans, A. (1998). Correction for partial volume effects in PET: principle and validation. *J. Nucl. Med.*, 39(5):904–911.

[Rousset et al., 1993] Rousset, O., Ma, Y., Leger, G., Gjedde, A., and Evans, A. (1993). Correction for partial volume effects in PET using MRI-based 3-D simulations of human brain metabolism. In Uemura, K., Lassen, N., Jones, T., and Kanno, I., editors, *Quantification of brain function using PET*, pages 113–123, Amsterdam. Elsevier.

[Rousset et al., 1996] Rousset, O., Ma, Y., Marenco, S., Wong, D., and Evans, A. (1996). In vivo correction for partial volume effects in PET: accuracy and precision. In Myers, R., Cunningham, V., Bailey, D., and Jones, T., editors, *Quantification of brain function using PET*, pages 158–165, San Diego. Academic Press.

[Rowe and Dai, 1992] Rowe, R. W. and Dai, S. (1992). A pseudo-poisson noise model for simulation of positron emission tomographic projection data. *Medical Physics*, 19:1113–1119.

[Schmidt et al., 1996] Schmidt, K., Lucignani, G., and Sokoloff, L. (1996). FDG-PET to determine regional cerebral glucose utilization: A re-examination. *J. Nucl. Med.*, 37:394–399.

[Seitz and Roland, 1992] Seitz, R. and Roland, P. (1992). Variability of the regional cerebral blood flow patterns studied with C-11-Fluoromethane and PET. *Comput. Med. Imag. Graph.*, 16:311–322.

[Shao et al., 1994] Shao, L., Freifelder, R., and Karp, J. (1994). Triple energy window scatter correction technique in PET. *IEEE Trans. Med. Imag.*, 13:641–648.

[Shao and Karp, 1991] Shao, L. and Karp, J. (1991). Cross-plane scattering correction - point source deconvolution in PET. *IEEE Trans. Med. Imag.*, 10:234–239.

[Shao et al., 1997] Shao, Y., Cherry, S., and et al, K. F. (1997). Development of a PET detector system compatible with MRI/NMR systems. *IEEE Trans. Nucl. Sci.*, 44:1167–1171.

[Sossi et al., 1998a] Sossi, V., Oakes, T., Chan, G., Schulzer, M., and Ruth, T. (1998a). Quantitative comparison of three- and two-dimensional PET with human brain studies. *J. Nucl. Med.*, 39:1714–1719.

[Sossi et al., 1998b] Sossi, V., Oakes, T., and Ruth, T. (1998b). A phantom study evaluating the quantitative aspect of 3-D PET imaging of the brain. *Phys. Med. Biol.*, 43:2615–2630.

[Spinks et al., 1992] Spinks, T., Jones, T., Bailey, D., Townsend, D., Grootoonk, S., and et al, P. B. (1992). Physical performances of a positron tomograph for brain imaging with retractable septa. *Phys. Med. Biol.*, 37:1637–1655.

[Stapleton et al., 1995] Stapleton, J., Morgan, M., Phillips, R., and et al., D. W. (1995). Cerebral glucose utilization in polysubstance abuse. *Neuropsychopharmacology*, 13:21–31.

[Stearns and Wack, 1993] Stearns, C. and Wack, D. (1993). A noise equivalent counts approach to transmission imaging and source design. *IEEE Trans. Med. Imag.*, 12:287–292.

[Takikawa et al., 1994] Takikawa, S., Dhawan, V., Chaly, T., Robeson, W., R, R. D., Zanzi, I., Mandel, F., Spetsieris, P., and Eidelberg, D. (1994). Input functions for 6-[Fluorine-18]Fluoro-dopa quantitation in parkinsonism: comparative studies and clinical correlations. *J. Nucl. Med.*, 35:955–963.

[Tanaka et al., 1982] Tanaka, E., Nohara, N., Tomitani, T., and Endo, M. (1982). Analytical study of the performance of a multilayer positron computed tomography scanner. *J. Comput. Assist. Tomogr.*, 6:350–364.

[Ter-Pogossian, 1985] Ter-Pogossian, M. (1985). Positron emission tomography instrumentation. In Reivich, M. and Alavi, A., editors, *Positron emission tomography*, pages 43–61, New York, Alan R Liss Inc.

[Ter-Pogossian et al., 1982] Ter-Pogossian, M., Ficke, D., Hood, J., Yamamoto, M., and Mullani, N. (1982). PETT VI: a positron emission tomography utilizing cesium fluoride scintillation detectors. *J. Comput. Assist. Tomogr.*, 6:125–133.

[Thompson, 1993] Thompson, C. (1993). Problem of scatter correction in positron volume imaging. *IEEE Trans. Med. Imag.*, 12:124–132.

[Thompson et al., 1986] Thompson, C., Dagher, A., Meyer, E., and Evans, A. (1986). Imaging performance of a dynamic positron emission tomograph: Positome IIIp. *IEEE Trans. Med. Imag.*, MI-5:183–198.

[Thompson et al., 1992] Thompson, C., Moreno-Cantu, J., and Picard, Y. (1992). PETSIM: Monte Carlo simulation of all sensitivity and resolution parameters of cylindrical positron imaging systems. *Phys. Med. Biol.*, 37:731–749.

[Thompson et al., 1991] Thompson, C., Ranger, N., Evans, A., and Gjedde, A. (1991). Validation of simultaneous PET emission and transmission scans. *J. Nucl. Med.*, 32:154–160.

[Trebossen and Mazoyer, 1991] Trebossen, R. and Mazoyer, B. (1991). Count rate performances of TTV03: the CEA-LETI time-of-flight positron emission tomography. *IEEE Trans. Med. Imag.*, 10:261–266.

[Votaw, 1996] Votaw, J. (1996). Signal-to-noise ratio in neuro activation PET studies. *IEEE Trans. Med. Img.*, 15:197–205.

[Wang et al., 1992] Wang, H., Jaszczak, R., and Coleman, R. (1992). Solid geometry-based object model for Monte Carlo simulated emission and transmission tomographic imaging systems. *IEEE Trans. Med. Imag.*, 11:361–372.

[Watanabe et al., 1992] Watanabe, M., Uchida, H., and et al, H. O. (1992). A high resolution PET for animal studies. *IEEE Trans. Med. Imag.*, 11:577–80.

[Webb, 1995] Webb, S. (1995). In the beginning. In Webb, S., editor, *The Physics of Medical Imaging*, pages 7–19, Bristol. Institue of Physics Publishing Ltd.

[Wienhard et al., 1994] Wienhard, K., Dahlbom, M., Eriksson, L., Michel, C., Bruckbauer, T., Pietrzyk, U., and Heiss, W. (1994). The ECAT EXACT HR: performance of a new high resolution positron scanner. *J. Comput. Assist. Tomogr.*, 18:110–118.

[Woods et al., 1993] Woods, R., Mazziotta, J., and Cherry, S. (1993). MRI-PET registration with automated algorithm. *J. Comput. Assist. Tomogr.*, 17:536–546.

[Worsley et al., 1992] Worsley, K., Evans, A., Marrett, S., and Neelin, P. (1992). A 3-D statistical analysis for CBF activation studies in human brain. *J. Cereb. Blood Flow Metab.*, 12:900–918.

[Worsley et al., 1996] Worsley, K., Marrett, S., Neelin, P., Vandal, A., Friston, K., and Evans, A. (1996). A unified statistical approach for determining significant signals in images of cerebral activation. *Human Brain Mapping*, 4:58–73.

[Wu et al., 1995] Wu, H., Hoh, C., Choi, Y., Schelbert, H., and Hawkins, R. (1995). Factor analysis for extraction of blood time-activity curves in dynamic FDG-PET studies. *J. Nucl. Med.*, 36(9):1714–1722.

[Xu et al., 1991] Xu, E., Mullani, N., Gould, K., and Anderson, W. (1991). A segmented attenuation correction for positron emission tomography. *J. Nucl. Med.*, 32:161–165.

[Yokoi et al., 1998] Yokoi, F., Rousset, O., Marenco, S., Evans, A., and Wong, D. (1998). Impact of partial volume correction on kinetic modeling parameters: preliminary experience in patient studies. In Carson, R., Daube-Witherspoon, M., and Herscovitch, P., editors. *Quantification of brain function using PET*, pages 77–82, San Diego. Academic Press.

[Yu and Nahmias, 1996] Yu, S. and Nahmias, C. (1996). Segmented attenuation correction using artificial neural networks in positron tomography. *Phys. Med. Biol.*, 41:2189–2206.

[Zeeberg et al., 1990] Zeeberg, B., Gibson, R., and Reba, R. (1990). Quantification of the dopamine D2 receptor in the living human caudate nucleus by PET: comparison of in vivo and in vitro kinetic parameters. *IEEE Trans. Med. Imag.*, 9:24–31.

[Zhang et al., 1993] Zhang, Y., Ma, Y., and Evans, A. (1993). Image reconstruction for PET using anatomical information. *Medical Physics*, 20:1591. Proc. COMP/CMBES Joint Conference: 162-163, Ottawa, May 1993.

[Zubal and Harrel, 1991] Zubal, G. and Harrel, C. (1991). Voxel-based Monte Carlo calculations of nuclear medicine images and applied variance reduction techniques. In Colchester, A. and Hawkes, D., editors, *Information Procesing in Medical Imaging*, pages 23–33, London, Springer-Verlag.